Illuminating Flatland

Nonlinear and Nonequilibrium Optical Properties of Graphene

Peter John Hale

School of Physics

University of Exeter

A thesis submitted for the degree of

Doctor of Philosophy in Physics

2012

Illuminating Flatland
Nonlinear and Nonequilibrium Optical Properties of Graphene

Submitted by Peter John Hale to the University of Exeter as a thesis for
the degree of Doctor of Philosophy in Physics
2012

I certify that all material in this thesis which is not my own work has been identified and that no material has previously been submitted and approved for the award of a degree by this or any other University.

Peter John Hale
2012

Abstract

In this thesis the nonlinear and nonequilibrium properties of graphene are experimentally investigated using degenerate four–wave mixing and time–resolved pump–probe spectroscopy. High quality exfoliated natural graphite and large area epitaxial graphene on silicon carbide are investigated with femtosecond and picosecond ultrafast pulses in the near–infrared. A bespoke technique for suspending exfoliated graphene is also presented.

In Chapter 3, the third–order nonlinear susceptibility of graphene is measured for the first time and shows a remarkably large response. Degenerate four–wave mixing at near–infrared wavelengths demonstrates an almost dispersionless emission over a broad spectral range. Quantum kinetic theory is employed to estimate the magnitude of the response and is in good agreement with the experimental data. The large susceptibility enables high contrast imaging, with a monolayer flake contrast of the order 10^7 times higher than for standard reflection imaging.

The degenerate four–wave mixing technique is utilised in Chapter 4 to measure the interface carbon signal of epitaxially grown graphene on silicon carbide. Comparable third–order signal from the silicon carbide bulk prevents true interface imaging. Excluding the third–order emission from detection by elongating the emission to outside a band–pass filter range allows for pure interfacial luminescence imaging. Features within the two growth faces are investigated with Raman spectroscopy.

Nonlinear measurements are an increasingly popular tool for investigating fundamental properties of graphene. Chapter 5 investigates the influence of ultrafast pulses on the nonlinear response of graphene. High instantaneous intensities at the sample are shown to reduce the nonlinear emission by a factor or two. Comparing the Raman peak positions, widths and intensities before and after irradiation points to a huge doping of the samples, of the order 500 meV.

In Chapter 6 the relaxation of photoexcited carriers is measured via time–resolved pump–probe spectroscopy, where a layer dependence of hot phonon decay is observed. Single layer flakes are observed to relax faster than bilayers and trilayers, with an asymptote reached at approximately four layers. Removing the substrate and measuring fully suspended samples reveals the same trend, suggesting that substrate interactions are not the cause of the enhanced decay. The decay mechanism is therefore intrinsic to graphene, perhaps due to coupling to out–of–plane, flexural phonons. The thickness dependence of epitaxial graphene on silicon carbide is compared to that of exfoliated flakes where the layer dependence is not observed. Phonon relaxation times, however, are in good agreement.

Predictions for future investigations into this novel material based on the works here are suggested in Chapter 7. Preliminary pump–probe measurements at high carrier concentrations are an example of such progress, which will offer an insight into further decay mechanisms in graphene.

Acknowledgements

Alex

In many ways this is the hardest part of the thesis for me to write, a section that I should never have had to. Alex's sudden passing was tragic. He wasn't just a supervisor to me, I regarded him more as a father figure and I hope this is how he saw me. Alex's approach to the scientific method, his work rate and most of all his obvious enjoyment of research was contagious. My first encounter with a bank holiday weekend was met with, ”We are not bankers”, a valid point, but one that took some time to get used to!

Our initial trip to Russia reflected the friendly, father–like relationship Alex had with his students. Visiting the sights (and bars!) of St. Petersburg was a joy, although I think he had us beaten when it came to the mid–afternoon vodka shots! I remember boarding the train from Moscow to St. Petersburg and asking if he wanted a beer, he said no but if they had it he would have a *small* glass of Cognac. After walking to the bar at the end of the train it transpired that we could only buy the entire bottle. Without hesitation this is, of course, what I bought for him. There aren't many people I would spend £26 on for a small Cognac!

There are many things that we will all miss about Alex, the press–up competitions, the discussions about physics, Russia and women! Mostly we will miss his smile and the way in which he constantly pushed us all to be both better scientists and better people. His influence on those of us fortunate to have known him will always be there, and I am thankful for this. As much as his passing has hurt, I do find solice in the knowledge that I am one of the lucky ones to have called him a friend.

A gentle, kind and generous person, a proud father and a wonderful friend. He will never be forgotten. Thanks Shevers!

My gratitude for the supervision I have been fortunate to receive from Euan can not be underestimated. I'm sure he won't mind me saying, the guy is a genius! All questions, no matter the subject, are met with a precise and well structured argument (almost always better than what I'd come up with!) and reflect the rigour with which Euan approaches his work. I've learnt so much from our time together and couldn't have wished for a better mentor.

With great fondness I can recall many of our supervisor meetings where Euan, Alex and myself would sit and discuss my project. This tended to last for anywhere up to three hours, the majority of which was spent discussing anything other than physics! I feel humbled to have had such incredible supervisors and I can't thank them enough.

There have been a great number of people who have helped me during the years and deserve special mention here. Julian Moger has been a great help in letting us take over his wonderful lab, without which the majority of these measurements would not have been possible. In the early days I was fortunate to have been assisted by Tom Isaac, a hero in the ultrafast lab. Many of the experiments have required bespoke apparatus from the workshop and I thank all the guys for their assistance. In the clean room, Spartaco Landi was a great help in etching substrates at the University of Bath and Dave Anderson for all his work here at Exeter. Sergei Mikhailov also deserves a mention for his theoretical help.

For assistance in data fitting and experiment I must acknowledge the help of Sam Hornett and Eugene Alexeev. I certainly wouldn't have got this far without their programming help!

Within G28 I have had a the privilege to work alongside some brilliant scientists. David Horsell, Saverio Russo, Monica Craciun and Jens Martin are always on hand with incisive and helpful remarks. Adam Price, Alexey Kaverzin, Aleksey Kozikov, Steve Hubbard, Fred Withers, Ivan Khrapach, Tim Khodkov, Sam Hornett, Dave Hudson, Tom Bointon, Steve Martins, to name a few, have provided the lab with both scientific enthusiasm and friendship. We have fabricated, measured and broken samples together. Heroes.

Within the wider quantum group I must thank the theorists for all their insight over the years. Specifically, Eros Mariani, Andrey Shytov, Misha Portnoi and GP Srivastava. I must also thank GP for allowing me to run the problems classes for the last three years, an experience I enjoyed tremendously.

I've been extremely fortunate to have been part of not just the quantum group but also the electromagnetic materials group. Interacting with the group both in the lab and socially has been a delight. There are too many people to name here but there are a few I must single out. Firstly, I must acknowledge Roy Sambles for his supervision during my MPhys project. His passion for science and the introduction into experimental physics he gave me was a key factor in my decision to continue into research. My lab partner, Joe Selwyn, also deserves a mention for all the help he gave me during the project and in our revision (Mario Kart) sessions! Bill Barnes, Pete Vukusic, Alastair Hibbins, Matt Lockyear and Ian Hooper have offered friendship and knowledge along the way and I hope to continue this in the future.

I couldn't have asked for a better place to study than Exeter, but what really makes this such a remarkable place is the people I have spent time with here. The G31 and basement people, especially Tom Constant, Chris Holmes, Ciaran Stewart, Helen Rance, Caroline Pouya, Ed Stone and Liz Brock have made this such a great place to live and work.

The time I have spent in Stormguards has moulded me into the person I am today. For the incessant competition, whether it be for who makes the tea or who jumps in the pool - I raise a whisky to you, thank you Stormers.

Of course I wouldn't have got to this point without the support of my family, but I think it goes much further than that. Having such close family friends really act as clear role models and much of what I do is because of the hard working nature of the people I have been surrounded by. I could name many people here but a special mention to the Hughes' and the Mostons, who always make us feel as part of their families. Having such good, kind people around you is inspiring and I am sure has helped develop me over the years. My only regret is that my grandparents are no longer here to see this, I'm sure they would have been proud. Growing up, doing sums to impress them and Auntie Margaret was my favourite part of Christmas and I'm sure this is what steered me towards a mathematics–based career path.

I feel so lucky for all the love and support and would not have reached this point without everyones help. Mum and Dad, cheers. Not much help with the physics I have to say but you have been, and continue to be, an inspiration. Thanks.

2008/2009, 2010/2011, 2011/2012 Physics Tower Run Champion

Publications

E. Hendry, P. J. Hale, J. Moger, A. K. Savchenko, S. A. Mikhailov. *Coherent Nonlinear Optical Response of Graphene*. Physical Review Letters, **105**:097401 (2010)

P. J. Hale, S. M. Hornett, J. Moger, D. W. Horsell, E. Hendry. *Hot Phonon Decay in Supported and Suspended Exfoliated Graphene*. Physical Review B, **83**:121404(R) (2011)

Conference Presentations

Ultrafast Optical Measurements of Graphene. NanoPeter conference on the fundamentals of electronic nanosystems, St. Petersburg, 2010. Poster presentation.

Hot Phonon Decay in Supported and Suspended Exfoliated Graphene. Graphene Week 2011: Fundamental science of graphene and applications of graphene–based devices, Obergurgl, 2011. Poster presentation.

Contents

List of Figures

Chapter 1

Background Theory

1.1 Introduction

The importance of carbon can not be underestimated, it is one of the building blocks for life, forming the backbone of DNA strands, and taking part in the photosynthesis reaction as carbon dioxide (CO_2). The diversity of carbon is what gives it its unique place in all forms of science. The sixth element in the periodic table, carbon possesses four outer, valence electrons. These can form strong covalent bonds with numerous different elements, producing millions of different compounds. The ability to form carbon–carbon single (Alkanes), double (Alkenes) and triple (Alkynes) bonds allows for the vast variety of compounds.

Carbon itself possesses several allotropes of differing dimensions, each with greatly different physical and electrical properties, see Figure 1.1.1. For example, the 3–dimensional (3D) forms of carbon are diamond and graphite. Whereas diamond is an insulator with a wide band–gap of approximately 5.5 eV[6], making it transparent to visible light, graphite is a semi–metal with a narrow band gap[7], making it opaque at optical wavelengths.

Graphene, the 2D form of carbon, was the last allotrope to be discovered. It consists of a single layer of carbon atoms covalently bonded in a hexagonal array. The study of graphene, however, dates back to 1947 when Wallace[8] first derived the band structure for graphite. Since graphite is constructed from multiple layers of weakly–bound graphene, calculating the properties of a single layer was the starting point for the bulk calculation. The tight binding model predicts a linear dispersion relation of charge carriers for a graphene monolayer, but it was agreed within the field that extracting and preserving a monolayer of atoms would not be thermodynamically stable[9,10].

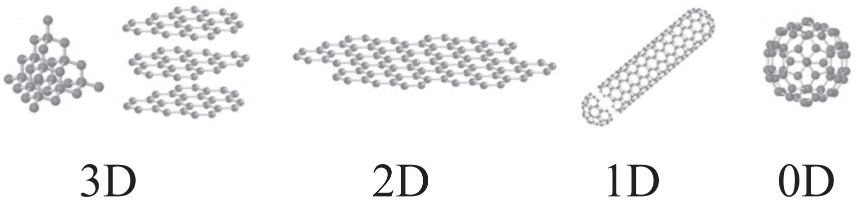

Figure 1.1.1: The most common allotropes of carbon and their dimensionalities, 3D diamond and graphite, 2D graphene, a 1D nanotube and a 0D Buckminsterfullerene. Image adapted from[1].

Carbon nanotubes and Buckminsterfullerenes are the 1D and 0D allotropes of carbon, respectively. Each are formed from rolling up a graphene sheet into a cylinder (nanotube) or a sphere (Buckminsterfullerene) and so the underlying physics, to an extent, is that of graphene. Nanotubes are of particular interest due to the great range of electrical, optical, mechanical and thermal properties one can observe depending on the way in which the tubes are rolled[11].

In 2004 the gold rush in graphene began. Novoselov, Geim and co–workers extracted and measured graphene[12], revealing to the world the huge potential this material holds. To date, research on graphene has produced over 13,500 papers, Figure 1.1.2. This figure, in just an 8 year period, is a reflection of the unique properties graphene possesses. From the quantum hall signature[13], where $\sigma_{\mathrm{xy}} = \pm 4e^2/h(N + 1/2)$, ($N$ is the Landau level index), to the universal optical conduction[14–16] and zero–mass of charge carriers, graphene is a truly unique and interesting material for both fundamental and application based research.

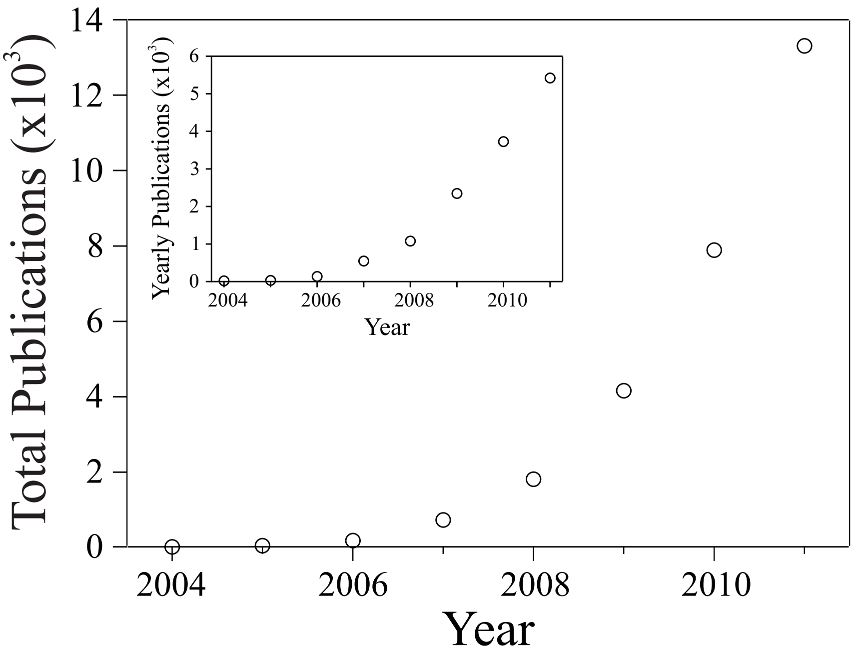

Figure 1.1.2: The cumulative number of publications with graphene in the title from 2004 to 2011. Inset: The number of publications per year. Data extracted from Web of Science.

1.2 Tight Binding Model

The electronic dispersion relation for graphene can be approximated using a nearest–neighbour tight binding formulation[8]. The carbon atoms that make up the graphene crystal each possess six electrons, two of which are in tightly bound core $1s^2$ states, the remaining four outer electrons are responsible for the crystal structure and therefore the electronic and phononic properties of graphene.

Three of the four valence electrons occupy the hybridised sp^2 orbitals, forming strong in–plane covalent bonds. Each atom therefore possesses three nearest–neighbours, separated by $120°$. The fourth and final outer electron belongs to a p_z orbital, orthogonal to the sp^2 bonds. This p_z orbital is weakly bound to the carbon atom and so is considered to be a free, or conduction, electron. The overlap of p_z orbitals, forming π and π^* bands, reveals the electronic dispersion relation via the tight binding approach.

A hexagonal lattice does not possess two primitive lattice vectors and so to reproduce the crystal structure of graphene a triangular lattice with a basis of two, shown in Figure 1.2.1, is required.

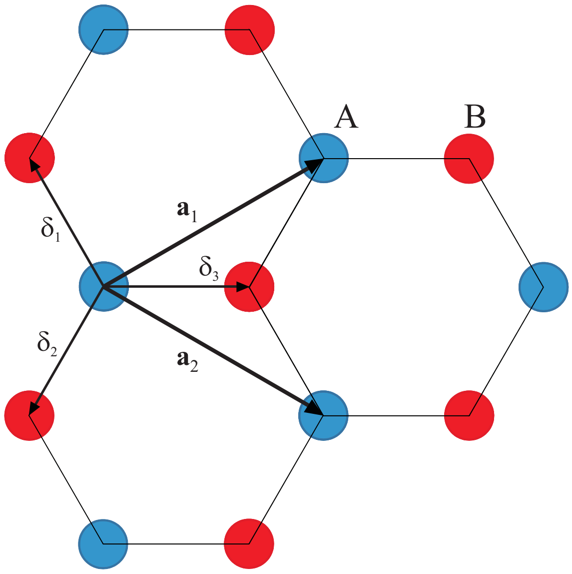

Figure 1.2.1: The hexagonal crystal structure of graphene, a triangular lattice with a basis of two. One may think of graphene as being two intersecting triangular lattices, A and B, represented here by the blue and red circles. The primitive lattice vectors and nearest–neighbours are shown for the carbon atoms on the A sublattice.

The primitive lattice vectors are,

$$\begin{aligned} \mathbf{a_1} &= \frac{a}{2}(3\hat{\mathbf{x}} + \sqrt{3}\hat{\mathbf{y}}) \\ \mathbf{a_2} &= \frac{a}{2}(3\hat{\mathbf{x}} - \sqrt{3}\hat{\mathbf{y}}) \end{aligned} \tag{1.2.1}$$

where $a = 1.42$ Å is the nearest–neighbour carbon–carbon spacing in graphene. The nearest–neighbour vectors then follow as

$$\begin{aligned} \delta_1 &= (\frac{\mathbf{a}_1}{3} - \frac{2\mathbf{a}_2}{3}) \\ \delta_2 &= (\frac{\text{-2}\mathbf{a}_1}{3} + \frac{\mathbf{a}_2}{3}) \\ \delta_3 &= (\frac{\mathbf{a}_1}{3} + \frac{\mathbf{a}_2}{3}). \end{aligned} \tag{1.2.2}$$

The reciprocal lattice vectors,

$$\begin{aligned} \mathbf{b}_1 &= \frac{2\pi}{3a}\left(\hat{x}, \sqrt{3}\hat{y}\right) \\ \mathbf{b}_2 &= \frac{2\pi}{3a}\left(\hat{x}, -\sqrt{3}\hat{y}\right) \end{aligned} \tag{1.2.3}$$

form the primitive unit cell of graphene. The first Brillouin zone is a hexagon rotated by 30° to the real lattice, Figure 1.2.2. The high symmetry points of the Brillouin zone are labelled. The coordinates of these positions in momentum space are; $\Gamma = (0, 0)$, $M = (\frac{2\pi}{3\mathrm{a}}, 0)$, $K = (\frac{2\pi}{3\mathrm{a}}, \frac{2\pi}{3\sqrt{3}\mathrm{a}})$ and $K' = (\frac{2\pi}{3\mathrm{a}}, \frac{2\pi}{-3\sqrt{3}\mathrm{a}})$. The K and K' points are of main interest for the low energy physics in graphene.

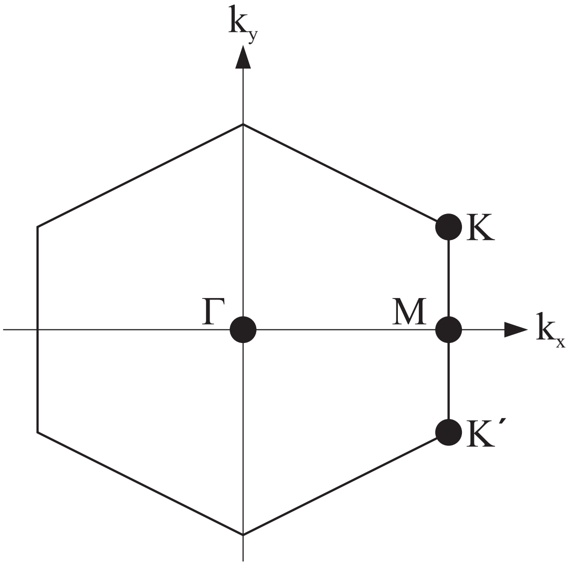

Figure 1.2.2: The first Brillouin zone of graphene with the high symmetry points indicated.

The tight–binding solution for the electronic dispersion relation in graphene is found by finding a solution to the Schrödinger equation, $\hat{H}\Psi_{\mathbf{k}} = E_{\mathbf{k}}\Psi_{\mathbf{k}}$. Here, $\hat{H}$ is the Hamiltonian for electrons in the periodic potential formed by the graphene crystal structure, E is the energy and **k** is the wave vector. The wavefunction, $\Psi_{\mathbf{k}}$, is considered as a linear combination of atomic orbitals (LCAO), which correspond to the carbon atoms on sublattices A and B,

$$\Psi_{\mathbf{k}} = c_{\mathrm{A}}\psi_{\mathbf{k}}^{\mathrm{A}} + \mathrm{c}_{\mathrm{B}}\psi_{\mathbf{k}}^{\mathrm{B}}. \tag{1.2.4}$$

$\psi_{\mathbf{k}}^{\mathrm{A}}$ and $\psi_{\mathbf{k}}^{\mathrm{B}}$ are the p_z atomic orbital wavefunctions, with corresponding amplitudes c_{A} and c_{B}. The normalised p_z atomic orbital wavefunctions must satisfy the Bloch condition $\psi(\mathbf{r}+\mathbf{R}) = e^{i(\mathbf{k}\cdot\mathbf{R})}\psi(\mathbf{r})$ and are written

$$\begin{aligned}\psi_{\mathbf{k}}^{A} &= \frac{1}{\sqrt{N}}\sum_{A} e^{i(\mathbf{k}\cdot\mathbf{r}_A)}\phi_A(\mathbf{r}-\mathbf{r}_A)\\ \psi_{\mathbf{k}}^{B} &= \frac{1}{\sqrt{N}}\sum_{B} e^{i(\mathbf{k}\cdot\mathbf{r}_B)}\phi_B(\mathbf{r}-\mathbf{r}_B)\,,\end{aligned} \tag{1.2.5}$$

where N is the number of unit cells considered and $\mathbf{r}_{\mathrm{A,B}}$ are lattice translation vectors. $\phi_{\mathrm{A,B}}$ are the local p_z atomic orbitals. To find the solutions to the Schrödinger equation one requires the matrix elements $H_{ij} = \langle\psi_i \mid H \mid \psi_j\rangle$, where i, j are the A and B sublattices,

$$\mathrm{c}_A H_{AA} + \mathrm{c}_B H_{AB} \;=\; E(\mathbf{k})\mathrm{c}_A \tag{1.2.6}$$

$$\mathrm{c}_A H_{BA} + \mathrm{c}_B H_{BB} = E(\mathbf{k})\mathrm{c}_B \tag{1.2.7}$$

The simultaneous equations are solved by noting that, since the two sublattices are equivalent, $H_{\mathrm{AA}} = H_{\mathrm{BB}}$. This on–site energy can be set to zero as it is an arbitrary value. One also notes that $H_{\mathrm{AB}} = H_{\mathrm{BA}^*}$. The solutions to Equations 1.2.6 and 1.2.7 are non–zero only if the secular determinant is zero. The integrals can be calculated with the knowledge of the nearest neighbour distances from Equation 1.2.2,

$$H_{AB} = \gamma_0 \left(e^{i\mathbf{k}\cdot\left(\frac{\mathbf{a}_1}{3} - \frac{2\mathbf{a}_2}{3}\right)} + e^{i\mathbf{k}\cdot\left(\frac{-2\mathbf{a}_1}{3} + \frac{\mathbf{a}_2}{3}\right)} + e^{i\mathbf{k}\cdot\left(\frac{\mathbf{a}_1}{3} + \frac{\mathbf{a}_2}{3}\right)} \right). \tag{1.2.8}$$

The term γ_0 is the nearest–neighbour hopping parameter and has a value $\gamma_0 \sim 2.8$ eV. It encompasses the overlap of the ϕ_{A} and ϕ_{B} orbital wavefunctions. Further considerations to the model can be made by introducing next–nearest–neighbour interactions, but these corrections are small. The use of only nearest–neighbours is sufficient.

Solving the determinant for the simultaneous equations 1.2.6 and 1.2.7, the energy dispersion for electrons in graphene can be approximated. The energy dispersion is simply

$$E(\mathbf{k}) \;=\; \pm\gamma_0 \sqrt{\left| \sum_{i=1}^{3} e^{i\mathbf{k}\cdot\mathbf{r}_i} \right|^2} \tag{1.2.9}$$

where $i = 1, 2, 3$ denotes the nearest–neighbour vectors. Multiplying this out one reaches the electronic dispersion relation

$$E(\mathbf{k}) = \pm\gamma_0 \sqrt{1 + 4\cos\left(\frac{\sqrt{3}a}{2}k_y\right)\cos\left(\frac{3a}{2}k_x\right) + 4\cos^2\left(\frac{\sqrt{3}a}{2}k_y\right)}, \tag{1.2.10}$$

illustrated in Figure 1.2.3. Importantly, the dispersion relation vanishes at the K and K′ points, meaning the Fermi surface is simply a set of isolated crossing points. Setting Equation 1.2.10 to zero, these coordinates in momentum space are $\pm\frac{2\pi}{3\mathrm{a}}\left(1, \frac{1}{\sqrt{3}}\right)$, $\pm\frac{2\pi}{3\mathrm{a}}\left(-1, \frac{1}{\sqrt{3}}\right)$ and $\pm\frac{2\pi}{3\mathrm{a}}\left(0, \frac{2}{\sqrt{3}}\right)$. Since each unit cell contains two electrons and a possible four states, the dispersion relation is exactly half–filled. All valence band states are therefore occupied and the Fermi energy, at $E = 0$, is found at the K and K′ points.

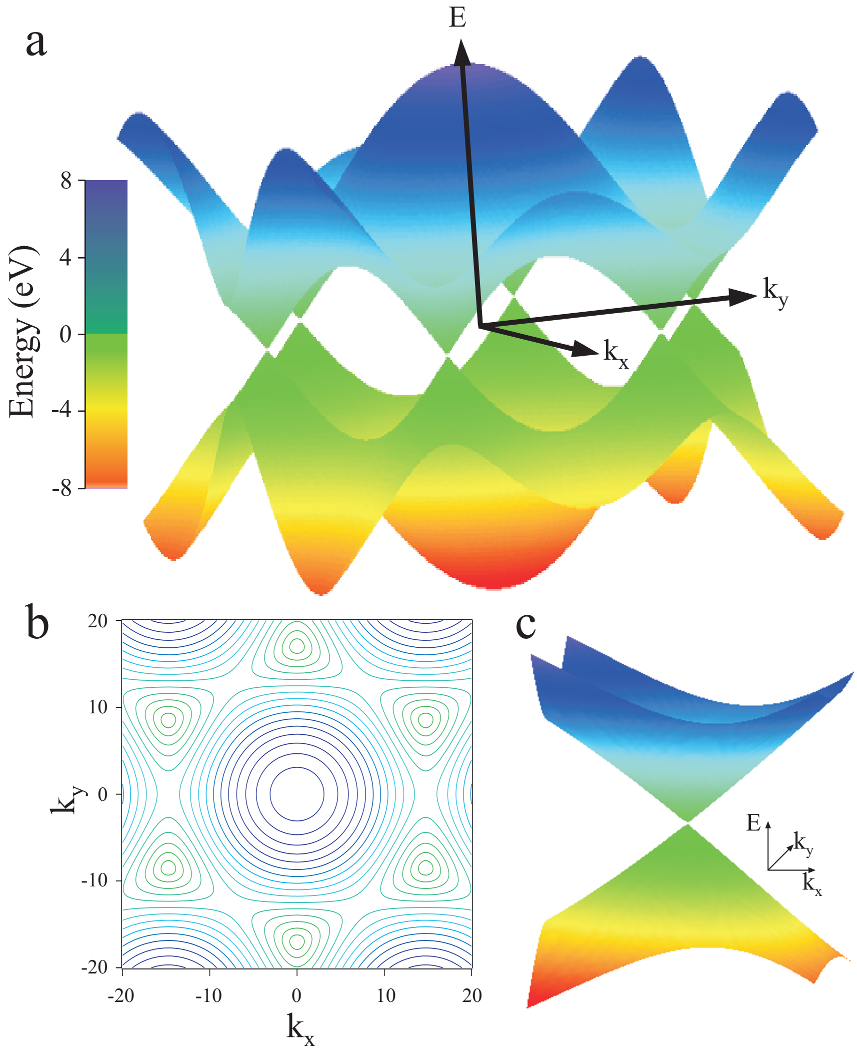

Figure 1.2.3: The nearest–neighbour electronic dispersion relation for graphene. (a) The full dispersion relation revealing the six points at which the bands cross. (b) A contour plot of the dispersion from $0 \leq E \leq 8$ eV. (c) A zoomed–in region of one of the K points, highlighting the linearity of the band structure around $E = 0$.

1.2.1 Low Energy Electronic Dispersion

The dispersion relation close to the K and K′ points can be shown to be linear with a simple expansion in the Hamiltonian of $\mathbf{k} = \mathbf{K}_{\mathrm{D}} + \Delta\mathbf{k}$, where $\mathbf{K}_{\mathrm{D}}$ denotes one of the crossing points, either at K or K′. Solving Equation 1.2.10 one may trivially find the position of the two crossing points within the first Brillouin zone,

$$\mathbf{K}_{\mathrm{D}}^{\pm} = \pm\frac{2\pi}{3\sqrt{3}a}\begin{pmatrix}\sqrt{3}\\ 1\\ 0\end{pmatrix}, \tag{1.2.11}$$

where the ± refers to the K and K′ points. Solving

$$\sum_{i=1}^{3} e^{\pm i\mathbf{k}\cdot\mathbf{r}_{\mathrm{A}}} \tag{1.2.12}$$

for $\mathbf{k} = \mathbf{K}_{\mathrm{D}} + \Delta\mathbf{k}$, one obtains the Hamiltonian,

$$H^{\pm} = \begin{bmatrix} 0 & -i\gamma_0\left(\frac{3a}{2}\right)e^{\pm i\frac{2\pi}{3}}\left(\Delta k_x \mp i\Delta k_y\right) \\ i\gamma_0\left(\frac{3a}{2}\right)e^{\mp i\frac{2\pi}{3}}\left(\Delta k_x \pm i\Delta k_y\right) & 0 \end{bmatrix}, \tag{1.2.13}$$

where again the ± indicates the K and K′ positions in reciprocal space. Substituting for the Fermi velocity, $v_F = \frac{3\gamma_0 a}{2} \sim 1 \times 10^6$ ms^{-1}, and solving the secular determinant, the energy dispersion is found to be linearly dependent on the wavevector,

$$E = \pm v_{\mathrm{F}}\left|\mathbf{k}\right| , \tag{1.2.14}$$

as seen in Figure 1.2.3(c). This dispersion differs greatly from the parabolic bands normally associated with solid state physics and is one of the main reasons why graphene is of such great interest. The conical shape of the dispersion, centered around the K and K′ points, is similar to that of a photon, which has the dispersion $\omega = ck$. Electrons in graphene can therefore be thought of as massless particles, propagating with a velocity $1/300^{\text{th}}$ of the speed of light.

1.3 Phonon Dispersion Relation

The phonon dispersion relation in graphene has been calculated via several methods[2,17–24] and confirmed in experiments[25–27]. There are three acoustic (A) and three optical (O) branches, the out–of–plane (Z), in–plane (L) and transverse (T) modes, Figure 1.3.1. For the nonequilibrium measurements performed in Chapter 6, the high–energy optical modes are of importance, since these are able to quickly remove energy from the hot electron population.

In Raman spectroscopy, only optically–active modes are observed. The 2D peak results from two opposite momentum in–plane TO phonons[3] at the K point, while the G peak is a result of the degenerate LO and TO modes[28] at the Γ point. These modes are detailed in Section 1.4.3.

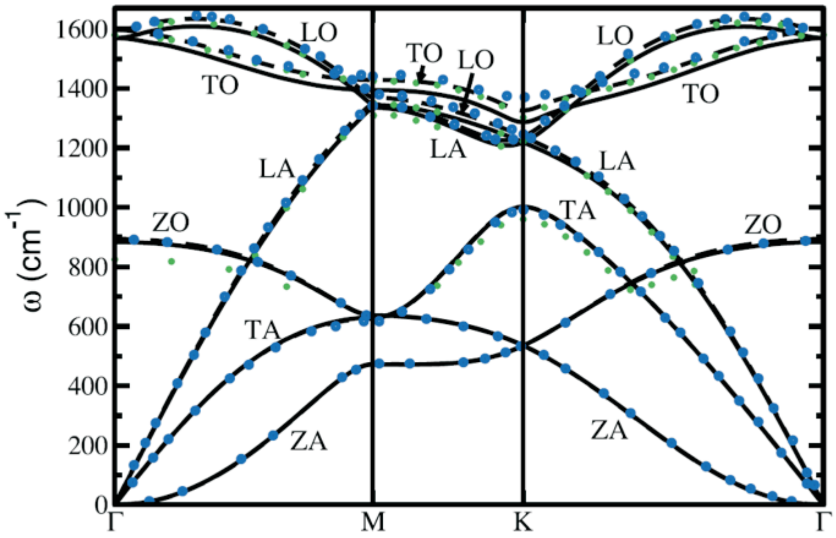

Figure 1.3.1: The phonon dispersion relation for graphene, revealing the three acoustic and three optical modes. Image adapted from[2].

1.4 Optics

The optical properties of graphene are of great interest as they offer huge potential for fundamental research and device applications. Arguably the most striking optical property of graphene is the presence of a universal optical conductance[14–16]. It can be shown that the optical conductance of a graphene sheet, $\pi e^2/2h$, is independent of any physical parameters, provided the photon energy is much larger than the Fermi energy and the temperature. This results in an optical absorption of approximately $\pi\alpha$, or 2.3%, where $\alpha = e^2/\hbar c$ (in cgs units) is the fine structure constant. This result is truly remarkable considering there are no parameters relating to the properties of graphene.

In this section, several optical phenomena are described. The origin of nonlinear frequency components, due to high intensity electric fields, is shown. Counting the number of graphene layers on a substrate via optical contrast is used to quantify layer thickness. To achieve this, the Fresnel equations at interfaces are used to calculate reflection spectra, from which the contrast per layer is determined. Finally, the origins of the Raman peaks in graphene are discussed, which offer a unique method for the quick, non–invasive determination of monolayer versus bilayer and multilayer samples.

1.4.1 Nonlinear Optics

With the production of the first working laser by Maiman in 1960[29], the field of nonlinear optics was born. High intensity monochromatic light sources were soon readily available causing an increase in experimental and theoretical research within the field.

Under the application of low electric fields, $\mathbf{E}$, the polarisation,

$$\mathbf{P} = \epsilon_0 \chi^{(1)} \mathbf{E}, \tag{1.4.1}$$

where ϵ_0 is the permittivity of free space, depends linearly with electric field. The constant of proportionality is $\chi^{(1)}$, measured in electrostatic units (esu) [$\mathrm{g}^{1/2}\mathrm{cm}^{3/2}\mathrm{s}^{-1}$]. For high electric fields, a Taylor expansion of the polarisation

$$\mathbf{P} = \epsilon_0 \left[\chi^{(1)} \mathbf{E} + \chi^{(2)} \mathbf{E} \cdot \mathbf{E} + \chi^{(3)} \mathbf{E} \cdot \mathbf{E} \cdot \mathbf{E} + \ldots \right], \tag{1.4.2}$$

enables a description of a material's response to higher orders. The magnitude of the nonlinear dependence is characterised by the susceptibilities $\chi^{(2)}$, $\chi^{(3)} \ldots$. The polarisation (dipole moment per unit volume) is used here as it can be shown that a time–varying polarisation may act as a source of new electric field components.

The four Maxwell equations, listed in terms of the free charge, ρ_f, and the free current, $\mathbf{J}_f$, are

$$\nabla \cdot \mathbf{D} = \rho_f \tag{1.4.3a}$$

$$\nabla \cdot \mathbf{B} = 0 \tag{1.4.3b}$$

$$\nabla \times \mathbf{E} = -\frac{\partial \mathbf{B}}{\partial t} \tag{1.4.3c}$$

$$\nabla \times \mathbf{H} = \frac{\partial \mathbf{D}}{\partial t} + \mathbf{J}_f. \tag{1.4.3d}$$

If one assumes there are no free charges and no free currents, Equations 1.4.3a and 1.4.3d are simplified. One also assumes, for simplicity, that the materials are non–magnetic, implying that $\mathbf{B} = \mu_0 \mathbf{H}$. Application of the curl operator onto Equation 1.4.3c, reversing the spatial and time operators and rearranging via the vector triple product, the following wave equation is obtained,

$$\nabla \left(\nabla \cdot \mathbf{E} \right) - \nabla^2 \mathbf{E} = -\mu_0 \frac{\partial^2 \mathbf{D}}{\partial t^2}. \tag{1.4.4}$$

The dielectric function, $\mathbf{D}$, is expressed as a combination of the electric field and the polarisation vector,

$$\mathbf{D} = \epsilon_0 \mathbf{E} + \mathbf{P}. \tag{1.4.5}$$

Substituting Equation 1.4.5 into Equation 1.4.4, one arrives at a standard wave equation (left hand side) with the addition of a 'source' term on the right hand side:

$$\nabla^2 \mathbf{E} - \frac{1}{c^2}\frac{\partial^2 \mathbf{E}}{\partial t^2} = -\frac{1}{c^2 \epsilon_0}\frac{\partial^2 \mathbf{P}}{\partial t^2}. \tag{1.4.6}$$

Note here that the divergence term from Equation 1.4.4 has been omitted. To a first approximation the divergence of the electric field is zero since $\nabla \cdot \mathbf{D} = 0$. For convenience, the substitution $c^2 = (\mu_0 \epsilon_0)^{-1}$ has been used.

The left hand side of Equation 1.4.6 simply describes the propagation of a transverse wave. The addition of a second order partial differential term in **P** gives rise to extra electric field components, since electromagnetic radiation is generated from accelerated charges. The polarisation is therefore used as a method of characterising the magnitude of a system's response to external fields, whether it be in the linear or nonlinear regime. By driving a system with high enough fields, one may observe extra frequency components and gain an insight into the physical properties of the system.

1.4.2 Visibility

One of the most striking properties of graphene is the extremely large interaction it has with light. A monolayer absorbs approximately 2.3% of all incident light, with much interest into the visibility of graphene being undertaken in recent years[30–36]. With the use of the Fresnel coefficients at interfaces, one can show how it is possible for graphene to be visualised on different substrates. The ability to see monolayers is of paramount importance and is almost certainly the reason the graphene field has been able to expand so rapidly.

Two substrates are considered, silicon wafers with a thermally grown oxidide layer, and glass. Oxidised silicon wafers are used as these provide a suitable substrate for electrical measurements. Graphene flakes deposited on top of the oxide layer are electrically isolated from the conductive silicon and so a gate may be applied to modify the carrier concentration. These were the first substrates used for investigating graphene. Glass substrates are considered as they will be the focus of the majority of work in this thesis. In order to perform optical measurements in transmission as well as reflection, one requires an optically transparent material. For experimental reasons the substrates must also be extremely thin, $\sim 100\ \mu$m, due to the short working–distance of the high numerical aperture objective lens used. Glass coverslides are therefore used and, as will be shown, provide suitable conditions for visualising graphene.

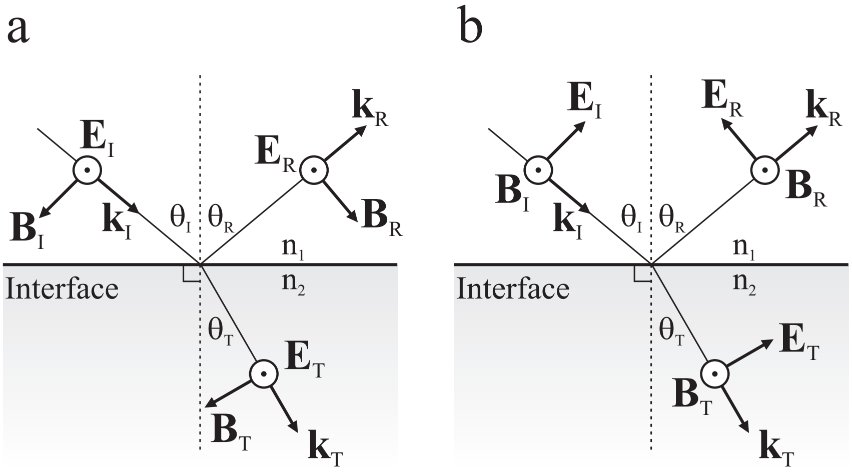

Figure 1.4.1: The incident, I, reflected, R, and transmitted, T, components for an electromagnetic wave at an interface between two media with refractive indicies n_1 and n_2. (a) TM polarised, (b) TE polarised.

Considering the interaction of planar electromagnetic radiation at an interface, Figure 1.4.1, one can simply derive the reflection and transmission Fresnel coefficients for a wave polarised parallel (transverse magnetic (TM)) or perpendicular (transverse electric (TE)) to the plane of incidence,

$$\left.\frac{\mathbf{E}_{0R}}{\mathbf{E}_{0I}}\right|_{TM} = r_{TM} = \frac{n_1 \mathrm{cos}\theta_T - n_2 \mathrm{cos}\theta_I}{n_1 \mathrm{cos}\theta_T + n_2 \mathrm{cos}\theta_I} \tag{1.4.7a}$$

$$\left.\frac{\mathbf{E}_{0T}}{\mathbf{E}_{0I}}\right|_{TM} = t_{TM} = \frac{2 n_1 \mathrm{cos}\theta_I}{n_1 \mathrm{cos}\theta_T + n_2 \mathrm{cos}\theta_I} \tag{1.4.7b}$$

$$\left.\frac{\mathbf{E}_{0R}}{\mathbf{E}_{0I}}\right|_{TE} = r_{TE} = \frac{n_1 \mathrm{cos}\theta_I - n_2 \mathrm{cos}\theta_T}{n_1 \mathrm{cos}\theta_I + n_2 \mathrm{cos}\theta_T} \tag{1.4.7c}$$

$$\left.\frac{\mathbf{E}_{0T}}{\mathbf{E}_{0I}}\right|_{TE} = t_{TE} = \frac{2 n_1 \mathrm{cos}\theta_T}{n_1 \mathrm{cos}\theta_I + n_2 \mathrm{cos}\theta_T}\,.\,. \tag{1.4.7d}$$

The Fresnel coefficients $r_{\text{TM,TE}}$ and $t_{\text{TM,TE}}$ are trivially related to the reflectance, R, and transmittance, T, simply by considering the ratios of the reflected and transmitted power per unit area (flux). Since the incident and reflected beams travel in the same material, the reflectance is straightforward,

$$R_{\text{TM,TE}} = r^2_{\text{TM,TE}}. \tag{1.4.8}$$

The transmittance is slightly complicated due to the refraction of the transmitted beam. The change in propagation speed and cross–sectional area, due to the different indices of refraction, reveal the transmittance as

$$T_{\mathrm{TM,TE}} = \left(\frac{n_1 \cos\theta_1}{n_2 \cos\theta_2}\right) \cdot t^2_{\mathrm{TM,TE}}. \tag{1.4.9}$$

From these equations one may predict the reflectance and transmittance for any structure. One simply requires the real and imaginary components of the refractive index as a function of wavelength. This is trivial for silicon and glass as these parameters are well known. Graphene, however, introduces an interesting problem since the permittivity of a medium is defined as a bulk property of the material. Being a monolayer of carbon atoms, this condition clearly can not be met. For simplicity, the real and imaginary components of the refractive index for graphene over the visible spectrum are taken from bulk graphite[37]. This is a valid assumption[34] as the optical properties are dominated by the in–plane bonds and transition dipoles. The approximation will break down at lower photon energies, ~ 0.7 eV[38], where the band structure of graphene and graphite differ.

Figure 1.4.2 plots the theoretical reflectivity for graphene and few–layer graphene on glass and a 300 nm oxidised silicon wafer for a plane wave at normal incidence. For glass, the reflection spectra is frequency independent over the visible spectrum with a low reflection coefficient. Silicon has a large reflection coefficient in the optical, making monolayer flakes impossible to see, but can be reduced with a cavity to produce destructive interference and a minima in reflection. The contrast, C, for a given structure is defined as

$$C = \frac{R_{\text{graphene}} - R_{\text{substrate}}}{R_{\text{substrate}}}, \tag{1.4.10}$$

where R_{graphene} and $R_{\text{substrate}}$ refer to the reflection coefficients from the graphene and substrate respectively. By destructively interfering the reflected light in the silicon structure, the denominator in Equation 1.4.10 reduces, increasing the contrast to observable levels (typically features below 1% become unobservable by eye) , Figure 1.4.3. The oxidised layer must be fine–tuned to destructively interfere with visible light, thus producing the minimal reflection coefficient. This condition is met with a silicon dioxide layer of approximately 300 nm or 100 nm. Importantly, a cavity of 200 nm produces constructive interference from the substrate, making monolayers practically impossible to see in reflection.

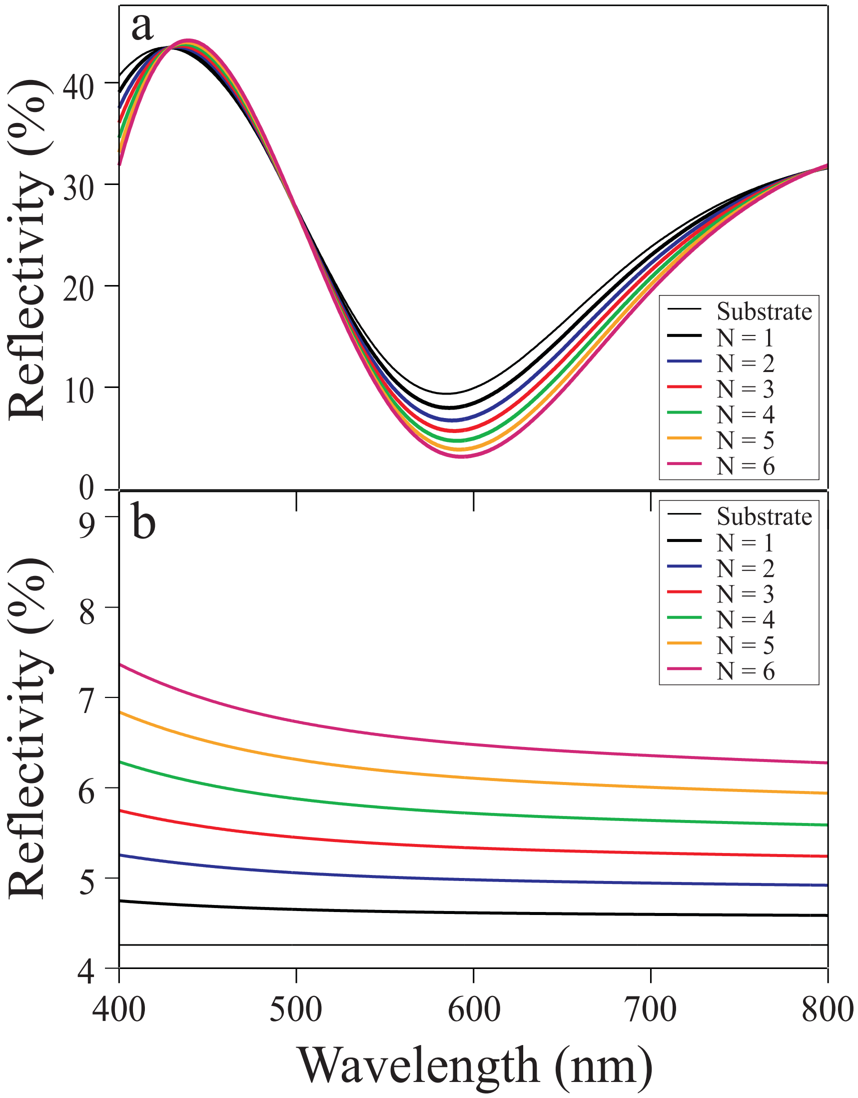

Figure 1.4.2: Reflectivity as a function of incident wavelength for mono– and few–layer graphene on oxidised silicon (a) and glass (b). Planar wave modelling using the Fresnel coefficients is used. The oxide thickness is 300 nm.

Remarkably, a single atomic layer can be visualised when placed on a glass substrate due to the low reflection coefficient of the glass. With no cavity condition required the wavelength dependence of the reflected signal on glass is flat, producing a contrast almost independent of wavelength.

Imaging few–layer flakes to determine layer number requires the use of a band–pass filter for oxidised substrates. Since white light illumination averages the contrast over the whole visible range, a lower contrast per layer is observed. With a narrow–band filter centered on the peak contrast, the visibility is optimised. The wavelength independence of the reflection on glass substrates means the contrast is unaffected with optical filters. Extracting the contrast at $\lambda = 596$ nm for both the glass and oxidised silicon substrates, the contrast per layer displays a linear dependence, Figure 1.4.4.

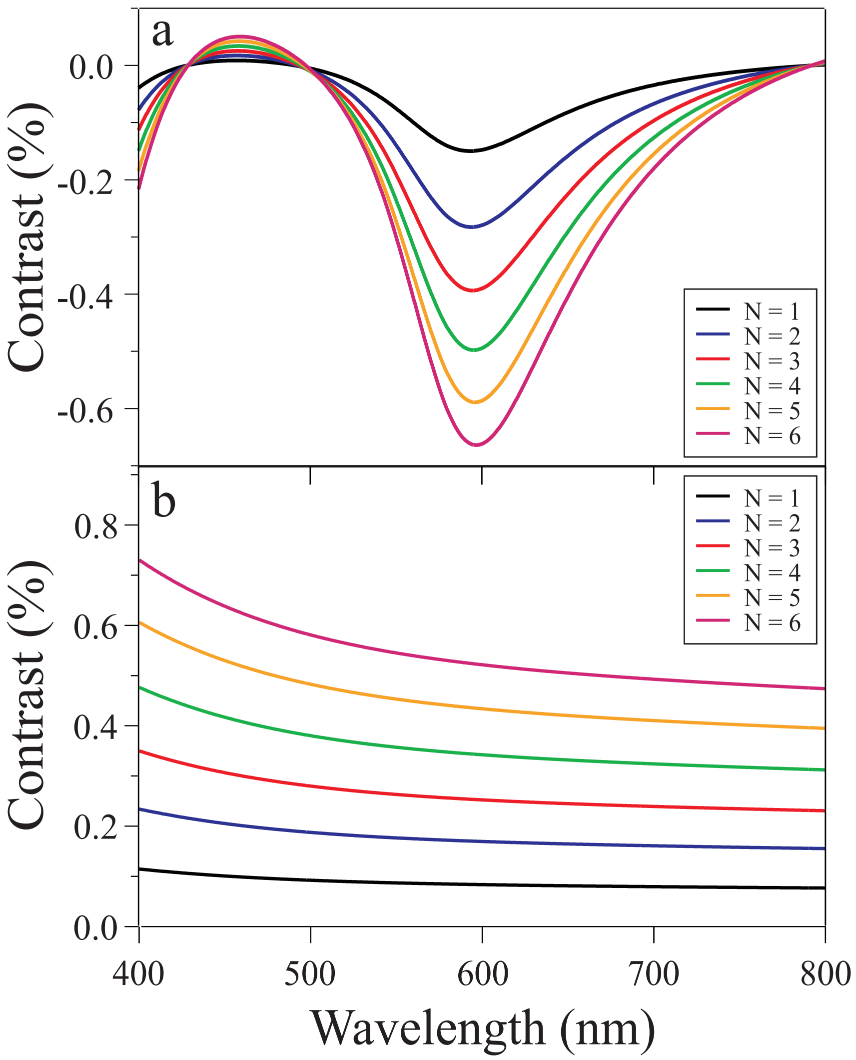

Figure 1.4.3: Contrast as a function of incident wavelength for mono– and few–layer graphene on oxidised silicon (a) and glass (b). Contrast is determined using Equation 1.4.10 and confirms that a monolayer is visible on a glass substrate. Due to the cavity present in the oxidised silicon wafer, a strong wavelength dependence in the contrast is observed. Careful choice of optical filters is required for visualisation.

Flakes found on both glass and oxidised silicon agree with the theoretical predictions of reflection contrast, however these predictions tend to be an over estimate. The theory suggests a peak contrast for monolayers of approximately 14% on the silicon substrates and 9% on glass. In practise, one observes the optical contrast (depending on the microscope setup used) to be typically 8% and 5% on the silicon and glass substrates respectively. There are several reasons for this discrepancy, especially when considering the oxidised wafers. Firstly, the contrast is extremely sensitive to the thickness of a cavity. Although the oxidised layers are nominally 300 nm, any error in this value will shift the resonance of the destructive interference. Similarly, the contrast has a large wavelength dependence and the choice of a suitable optical filter is required. For white–light illumination one averages the contrast at all wavelengths, resulting in a much lower contrast. Choosing a narrow–band filter as close to the peak contrast as possible will ensure the flakes are easily observable. One must also take into account the numerical aperture of the objective lens[33]. Simple plane–wave illumination, as in the simple Fresnel model, does not take into account the distribution of incident angles onto the sample through a high numerical aperture lens. As the angle of incidence is increased, so is the reflection coefficient, lowering the observed contrast.

For few–layer samples the optical contrast is linear with the number of layers and so can be used as a characterisation tool. Of course this is in no way definitive, but provides an approximate value for layer numbers. In order to distinguish a monolayer sample, the Raman spectra is employed which, as detailed in the following section, is able to distinguish absolutely between monolayers, bilayers and multilayers.

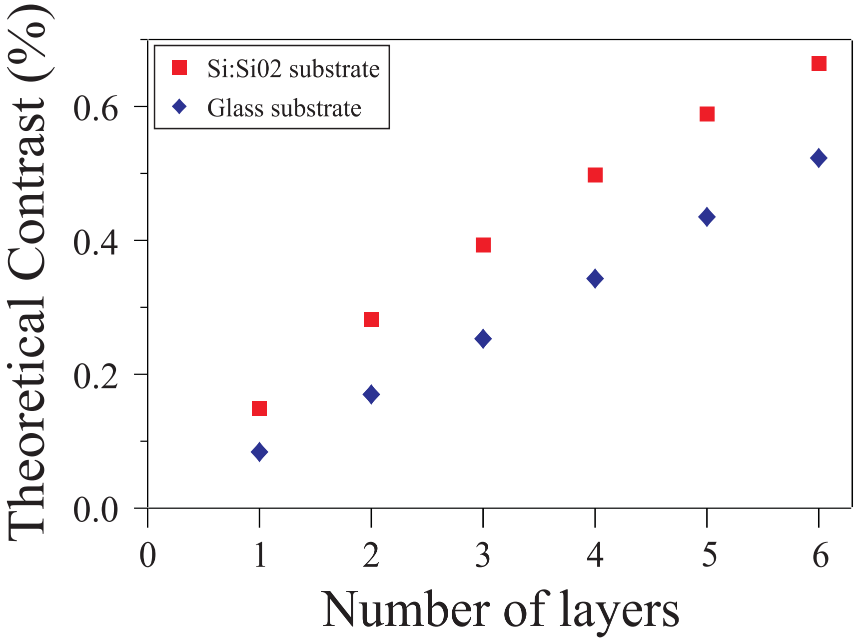

Figure 1.4.4: Contrast as a function of few–layer graphene for $\lambda = 596$ nm. For few–layer samples the contrast is linear in N and is a useful characterisation tool for determining layer thickness.

1.4.3 Raman Spectroscopy

Raman spectroscopy is a powerful tool for the characterisation of a wide variety of materials. Discovered in 1928 by C. V. Raman, the process is used in a great number of research fields due to the non–destructive nature of the measurements and the valuable information about the samples it provides. Unlike most imaging techniques, Raman spectroscopy does not probe electronic transitions, instead, the low energy physics of the system is revealed. Information about the lattice vibrations within a system are revealed via inelastic

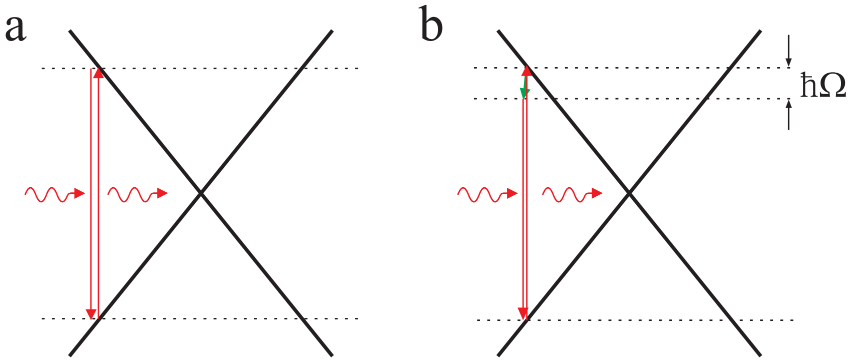

Figure 1.4.5: Elastic Rayleigh and inelastic Raman scattering in graphene. (a) Rayleigh scattering at the K point of the Brillouin zone in monolayer graphene. The incident photon excites an electron–hole pair which recombine, producing a photon of the same energy. (b) Raman scattering for the G peak in graphene. An excited electron scatters inelastically with a Γ point phonon of low momentum, near the Brillouin zone centre, before recombining with a hole. The photon produced is of lower energy than the incident photon by a value of $\hbar\Omega$.

light scattering.

In graphene, Raman spectroscopy is a powerful tool for distinguishing monolayer versus bilayer samples. In essence, Raman spectroscopy is a rather simple process. An incident photon excites an electron from an occupied state in the valence band to an available state in the conduction band, Figure 1.4.5(a). Without interactions between the excited electron and the lattice, the electron simply recombines with the hole left in the valence band and emits a photon of the same energy. This is simply elastic Rayleigh scattering. If, however, the electron is able to interact with the lattice, either gaining or losing energy from a phonon, then the resulting recombination will emit a photon with a slightly different energy, Figure 1.4.5(b). By irradiating a sample with a continuous wave of monochromatic light, one can look at the reflected spectra to find distinct peaks, attributed to optically active phonon modes.

There are two types of Raman scattering, Stokes and anti-Stokes, Figure 1.4.6. For Stokes shifts, an excited electron transfers energy to a phonon before recombination. This results in an emitted photon of lower energy than the incident photon. Anti-Stokes scattering is simply the opposite, an excited electron is scattered into an elevated level from an energetic phonon. The resultant photon is therefore of higher energy than the incident photon. Of course, Rayleigh scattering will be the dominant process for all samples. In order to measure the Raman shifts, of the order one part in 10^{-6}, a specialised system must be used, see Section 2.3.

Due to the lower occupation of phonons in elevated energy states and the low number of available ground states, anti-Stokes scattering has a lower probability than Stokes scattering. For this reason, only the Stokes shift will be considered.

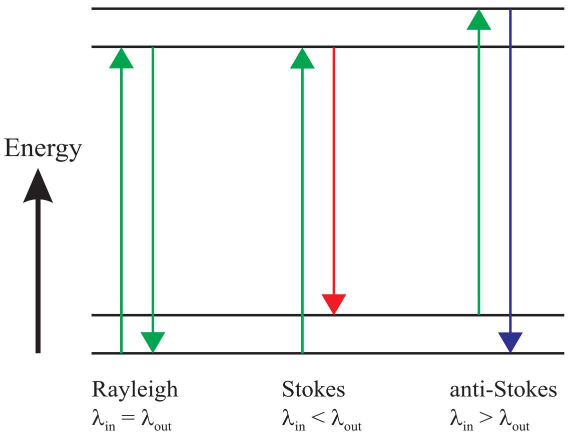

Figure 1.4.6: Energy diagram for elastic Rayleigh scattering and the inelastic Stokes and anti–Stokes scattering. For Rayleigh scattering, the excited electron experiences no phonon scattering and the recombination produces a photon with the same energy as the incident photon. For a Stokes shift, the electron excites a phonon to an elevated level, reducing the energy of the electron. The recombination produces a lower energy photon then the incident one. Anti–Stokes scattering scatters the electron into a higher energy level, from a high energy phonon. The recombination therefore produces a higher energy photon then the incident one.

In graphite there exists three optically active Raman modes of interest, Figure 1.4.7, the defect–induced D band at $\sim$ 1350 cm^{-1}, the G peak at $\sim$ 1580 cm^{-1} and the 2D peak at $\sim$ 2700 cm^{-1}. The G peak is the most prominent feature in the spectra of bulk graphite and is a result of an in–plane vibration of the carbon atoms. The mode is of low momentum, close to the Γ point in the first Brillouin zone, Figure 1.2.2. For a monolayer sample, Figure 1.4.5(b), the Raman energy diagram is rather trivial. The excited electron interacts with a Γ point phonon of energy $\hbar\Omega = 196$ meV, resulting in a slightly red–shifted photon being emitted. (This is the more probable Stokes shift, found by measuring positive shifts from the laser line. With the use of a different edge filter, the anti–Stokes shift can also be measured. This is a much weaker process due to the exponentially lower probability of finding a phonon in a higher energy state).

The D peak in graphite is found at $\sim$ 1350 cm^{-1}, but only for defected samples. The mode originates from a phonon at the K point of the Brillouin zone, Figure 1.2.2, but this itself is not allowed in pristine samples, Figure 1.4.8. In order to observe the D mode, an interaction with a defect must occur. The excited electron is scattered into an adjacent valley but has no route to recombine. An elastic scattering event must take place to return the electron its original valley where it can recombine. From the uncertainty principle,

$$\Delta x \, \Delta p_x \geq \frac{\hbar}{2}, \tag{1.4.11}$$

the large momentum shift required must therefore come from extremely short–range scat-

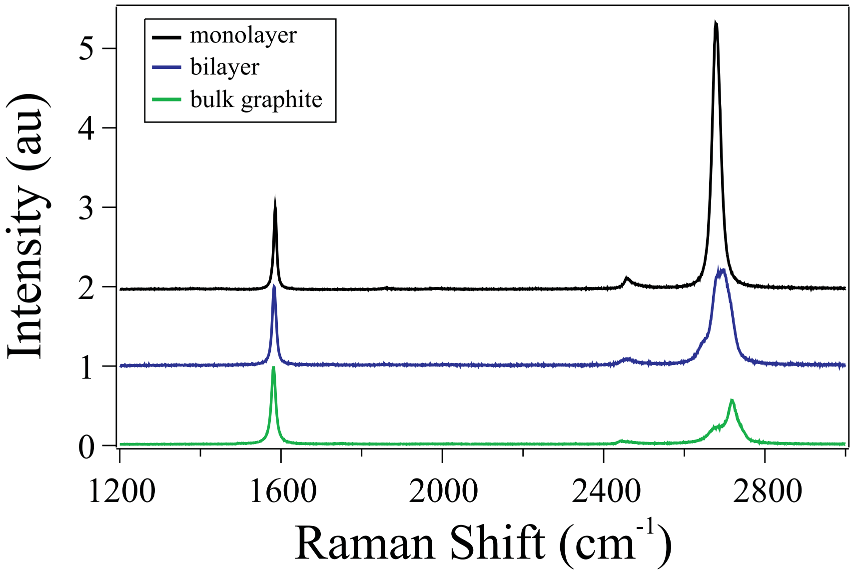

Figure 1.4.7: Raman spectra for monolayer and bilayer graphene, plotted against a spectra of bulk graphite. The G peak, at $\sim$ 1580 cm^{-1}, and the 2D peak, at $\sim$ 2700 cm^{-1}, are prominent. The defect–induced D peak is not visible at $\sim$ 1350 cm^{-1}, due to the high quality of the samples. The spectra are normalised to a G peak intensity of unity and offset in the y–axis for clarity. The feature at $\sim$ 2450 cm^{-1} is an intervalley scattering process via a TO and an LA phonon[3] and is not of interest here.

terers, atomic defects. For the high quality exfoliated samples measured, one does not see evidence of a D peak.

As previously mentioned, the power of Raman spectroscopy in graphene is the ability to distinguish single atomic layers quickly and non–invasively. This is achieved by comparing the profile of the second order of the D mode, the 2D peak, for monolayers and multilayers. For single–layer samples, the 2D peak is a fully resonant process, only achievable via a single path, Figure 1.4.9(a). This results in a single, symmetric peak, found at twice the Raman shift of the D peak position. In order for the process to occur, two phonons of equal energy, but opposite momentum, are required. Due to the lack of any gap in the band structure of graphene, all processes are resonant and so the magnitude of the peak is large.

For the case of a bilayer, Figure 1.4.9(b), there exists four resonant pathways. This is due to the different band structure associated with a bilayer. When considering the tight binding model for a bilayer one must include the overlap integral from the second layer. This produces a band structure that is parabolic at low energies and touches at the K and K′ points of the Brillouin zone. A higher–energy band, approximately 400 meV above the Dirac point, is also formed[39]. This produces the multiple peaks in the bilayer Raman spectra.

Each of the processes illustrated in Figure 1.4.9(b) differ both in energy and coupling

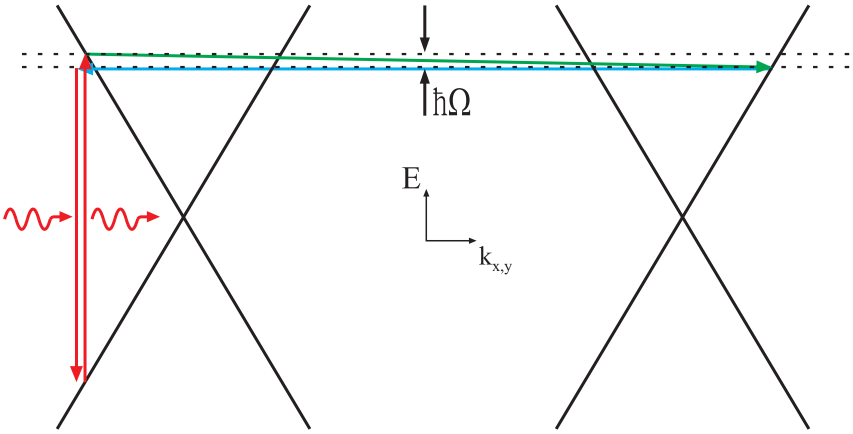

Figure 1.4.8: The Raman scattering process for the D peak in graphene. The high momentum K point phonon (green arrow) scatters an excited electron into an adjacent valley. To recombine, the electron must scatter back to the original valley, this is achieved via a short range, high momentum, elastic scattering event (blue arrow) due to a defect.

strength, with density functional theory showing that the coupling of photons is strongest with the upper processes in Figure 1.4.9(b)[40]. This is revealed in the more prominent features within the 2D peak. A high resolution Raman spectrum of monolayer and bilayer graphene, centred around the 2D peak, is shown in Figure 1.4.10 and demonstrates how the profiles of the peaks are easily distinguished. Fitting with a single Lorentzian peak, a full–width half–maximum (FWHM) of approximately $30\ \mathrm{cm}^{-1}$ is found for the monolayer, compared to $\sim 55\ \mathrm{cm}^{-1}$ for a single peak fit to the bilayer. Fitting the bilayer instead with four peaks allows for a more accurate description of the spectrum and can be used to distinguish between bilayers and trilayers. For the investigation of trilayer graphene, Raman spectroscopy is also a useful tool in determining whether samples are ABA– or ABC–stacked due to the different peak magnitudes of the resonant processes[41].

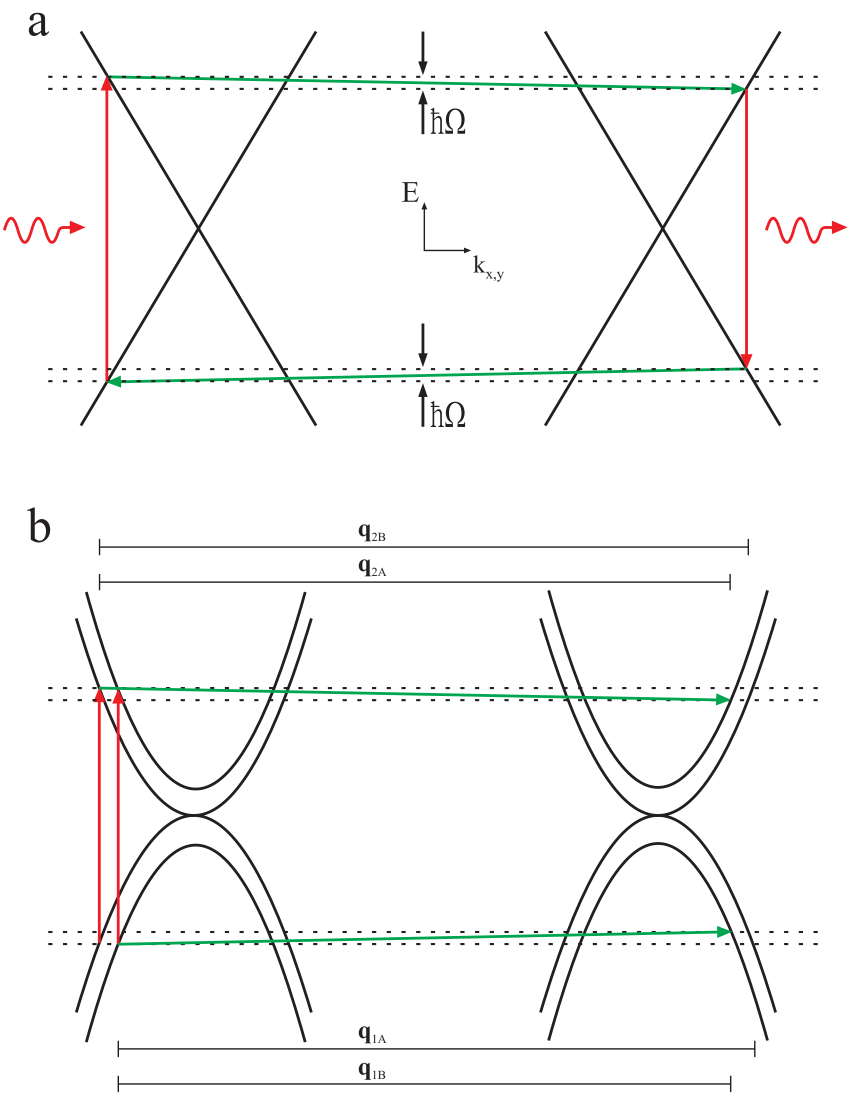

Figure 1.4.9: The 2D Raman scattering processes for graphene and bilayer graphene. (a) The fully resonant 2D Raman process for graphene via two K point phonons (green arrows) of equal and opposite momentum. (b) The 2D Raman processes for bilayer graphene. The four distinct peaks found in the Raman spectrum are highlighted. For clarity, the momentum shifts $\mathbf{q}_{2A}$ and $\mathbf{q}_{2B}$ are shown for electron scattering, $\mathbf{q}_{1A}$ and $\mathbf{q}_{1B}$ for hole scattering.

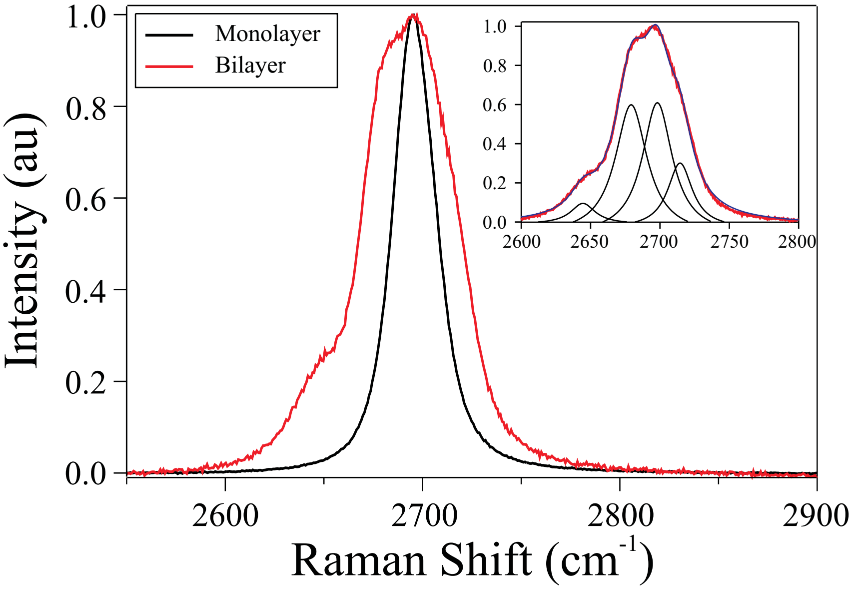

Figure 1.4.10: Normalised high resolution Raman spectra for monolayer and bilayer graphene at the 2D peak. The symmetric profile of the single layer is in stark contrast to the multi–peak found in the bilayer. Inset: Fitting the bilayer 2D peak with four Lorentzian curves (black), the resultant fit (blue) shows excellent agreement.

Chapter 2

Experimental Techniques

In this chapter the fabrication, characterisation and measurement techniques utilised in this thesis are discussed. Many of the techniques used are well established but some, such as the fabrication of suspended graphene samples, have been developed independently. Explanation of the fabrication and measurement techniques is such that all experiments may be repeated from this work.

2.1 Sample Fabrication

2.1.1 Mechanical Exfoliation of Natural Graphite

Standard graphene samples are fabricated via mechanical exfoliation[12] from natural graphite, Figure 2.1.1(a). All the exfoliated samples used in this work are prepared from this single large graphite flake purchased from Madagascar. The use of a single, large crystal of graphite is so as to increase the probability of fabricating large area graphene samples. If the graphite possesses large domains it follows that the exfoliated flakes will be of a larger size than those from smaller domains. Obtaining substrates with large flakes not only makes finding the samples much easier, but also enables more elaborate samples to be fabricated, such as multi–terminal devices. To date, single–crystal exfoliated flakes provide the highest quality graphene samples and are the material of choice for all transport measurements.

The preparation of samples using the following method has now become a standard procedure for high quality graphene flakes. The graphite is placed onto a pre–cut piece of adhesive tape, peeled several times and pressed onto the desired substrate, Figure 2.1.1(b,c). Ordinary Scotch tape may be employed here, although it is found to leave large amounts of glue residue on the flakes and substrate. Instead, a less adhesive tape (Nitto Denko) is used which leaves behind a much cleaner surface after peeling and deposition.

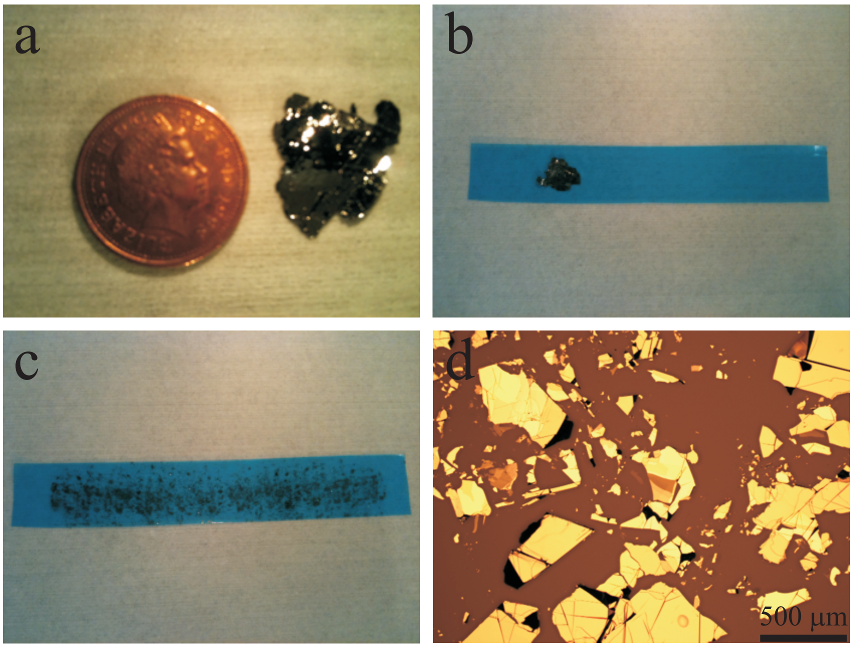

Figure 2.1.1: Images of the mechanical exfoliation technique. (a) An image of the large piece of graphite from which all of the samples in this work are fabricated from. A one pence coin is used for scaling. (b) The graphite is placed onto a cut piece of Nitto tape and removed, leaving behind part of the bulk graphite. (c) The tape is folded and unfolded approximately 10 times to produce a homogeneous distribution of flakes which can be studied under an optical microscope to look for large–area domains. (d) An example of a 5× magnification white light image of flakes on a glass substrate. Manual searching for low contrast flakes is then required in order to find monolayer samples.

Although statistics are few, experience shows that peeling the tape too many times results in higher densities of flakes (thick and thin) but generally of a smaller surface area. Peeling too few times, in an attempt to prevent the loss of large area flakes, results in a low density of deposited flakes. A compromise of peeling approximately ten times, ensuring a homogeneous covering of flakes over the tape, seems to be the best option.

Before transferring the flakes from the tape to the substrate an optical microscope is used to search for areas of large domain sizes. Once found, a cleaned substrate is firmly pressed face–down onto the corresponding part of the tape. To avoid a low yield of flakes being transferred the substrate is placed onto a hot plate to soften the glue on the tape, approximately 100° C for 60 seconds. This method also has advantages for delicate substrates, such as glass coverslides, which can easily be broken during the tape removal process even when the less adhesive Nitto tape is used. A random distribution of graphite, few–layer and monolayer graphene is then found on the substrate, Figure 2.1.1(d). The laborious task of manually searching the substrate for the thinnest areas begins and the desired flakes are identified via their optical contrast (Section 1.4.2).

The traditional substrate of choice for graphene measurements is n–doped silicon with a 300 nm, thermally grown oxide layer on top. This provides a suitable substrate to allow for back–gating, due to the separation of the conductive graphene and the silicon gate. This configuration also allows monolayer graphene to be visualised under an optical microscope, as seen in Section 1.4.2.

For the optical measurements performed in this thesis there is a requirement for transparent substrates such that visible and near–infrared wavelengths can pass through the entire structure. There is also a requirement for the substrate to be extremely thin, of the order $\sim 100\ \mu$m, so as to take full benefit of the high resolution water immersion objective lense.

Glass cover slides are first sonicated in acetone for 2 minutes, rinsed in deionised water (to remove the majority of the acetone), sonicated for a further 2 minutes in isopropanol and dried with N_2 gas. The substrates are then taken to an oxygen plasma asher (Emitech K1050X) and exposed to a power of 40 W for 20 minutes. This method has been found to greatly increase the density of thin flakes sticking to the substrate, presumably due to a cleaner surface providing better adhesion for flakes.

The power and duration of the etching is of some importance for obtaining a large density of flakes. Initial tests on full power (100 W) revealed substrates with extremely low densities. Etching at 40 W for just 2 minutes also resulted in a low yield. While statistics are sparse, a 40 W etch for 20 minutes appears to give the best results. Further tests on varying the duration and power were not conducted as this was not the focus of the project.

2.1.2 Large Area Growth Techniques

With the emergence of graphene comes the potential of a new generation of devices which can be transparent, conductive and flexible. Of course, due to the lack of a band gap in pristine monolayer graphene, practical devices can not yet be realised due to the poor on/off ratios achieved. Much research is been undertaken to address this by bonding different elements or molecules to the graphene. This modifies the band structure and can result in band gaps of 0.5 eV in hydrogenated graphene[42] and 3.07 eV in fluorinated graphene[43]. However, the real issue for future devices is one of scaling. The best graphene samples are, to date, still fabricated via mechanical exfoliation of natural graphite and found manually under an optical microscope. This is a laborious task and yields extremely low numbers of samples. For future industry, graphene will be needed on a large scale.

Recent advances in the large scale growth of graphene on various substrates are particularly encouraging as we begin to move towards commercial applications. For instance, metal substrates, such as nickel[44–48] and copper[49,50] are used as catalysts to grow carbon layers. For the nickel method, a thin film of metal is heated to a high temperature and a hydrocarbon gas is allowed to penetrate into the film. By controlling the rate of cooling, only a small amount of carbon can leave the bulk and form layers on the surface. The process on copper films is similar but the carbon does not penetrate into the metal, instead, the copper acts as a catalyst and so the process is self–limiting. The drawback of both of these methods is the production of a carbon layer on a conducting substrate which is not suitable for producing gated structures. Therefore, the large area graphene must first be transferred before it can be contacted and fabricated into a field–effect transistor device.

Arguably the most promising route for the large scale fabrication of graphene occurs through epitaxial growth on heated SiC substrates[51–53]. In this process, silicon atoms preferentially sublimate during annealing, leaving behind carbon atoms that self–assemble into graphene layers. In recent years, devices fabricated from epitaxial graphene have much improved performance figures. Currently, samples with a field mobility $\sim 3 \times 10^4$ cm^{2}V^{-1}s^{-1} have been recorded in an epitaxial graphene device on SiC[54]. This is still some way behind the reported values for exfoliated high quality, suspended graphene[55], where mobilities of approximately 2×10^5 cm^{2}V^{-1}s^{-1} have been observed, but Tedesco *et al.*[56] have shown that the intrinsic limit on mobility could be as high as 1.5×10^5 cm^{2}V^{-1}s^{-1}, even at 300 K.

The epitaxial graphene samples used in this work are provided by C. Berger at the Georgia Institute of Technology and C. Marrows, G. Creeth and A. Strudwick at the University of Leeds. Prior to annealing, the SiC substrate has one silicon– and one carbon–terminated face, Figure 2.1.2. It is well known that the $[000\bar{1}]$ carbon–terminated face of SiC does not show the growth of a covalently–bonded buffer layer[57], and the individual layers are decoupled due to their rotational stacking[58], resulting in high mobility samples[54]. Moreover, growth on the carbon–terminated face is found to be much faster than the silicon–terminated face; whereas the silicon face appears to be self–limiting at approximately 10 layers, the carbon face shows growth up up to 100 layers[53]. However, growth tends to be uneven across the substrate, leading to thickness variations on the micron scale[59].

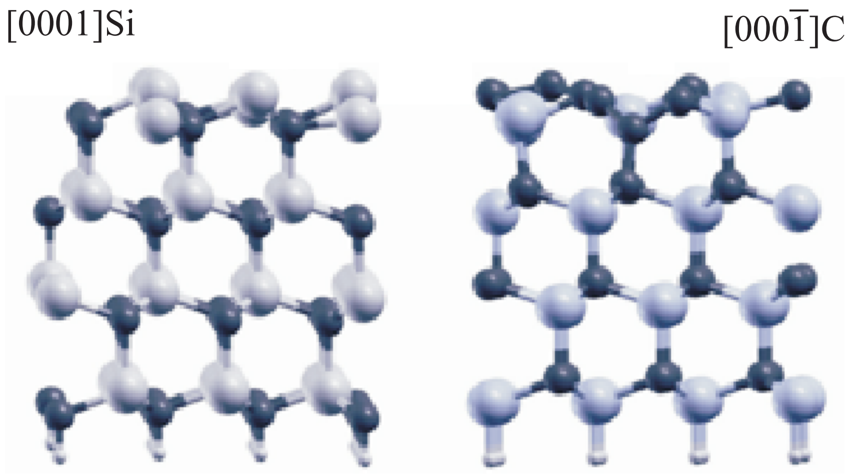

Figure 2.1.2: Schematic of the 4–H SiC [0001] and [000$\bar{1}$] interfaces, the silicon and carbon terminated faces. The white and black spheres represent silicon and carbon atoms, respectively. Image adapted from Borysiuk *et al.*[4].

2.1.3 Suspended Graphene

The following section describes a bespoke method for the fabrication of suspended graphene samples. The use of reactive ion etching (RIE) and optical lithography are described. Attempts are initially made to fabricate suspended structures using wet etching with hydrofluoric acid but, as shown, proved unsuccessful due to the isotropic profile of the wet etching.

2.1.3.1 Optical Lithography

Suspended samples are fabricated by depositing graphene onto pre–etched substrates. An optical mask is first made to transfer a pattern design onto the desired substrate which can then be etched, ready for graphene deposition. Two designs for the optical mask are attempted, one with an array of long trenches cut into the substrate so as to suspend the flakes at either end, the second to fabricate an array of holes in the substrate, thus supporting the flake all the way around the suspension. Suspended flakes were never found using trenches, each sample that was investigated showed flakes that touched the base of the holes. This is believed to be due to the lack of support around the sides of the flakes. To combat this, an array of etched holes was used so that the flakes would be in contact with the substrate all the way around the suspended region.

Two constraints are put on the size of the features required within the mask, the spot–size at the focal point of the objective lens and the average size of flakes found on the substrate. For the 1.2 numerical aperature (NA) water immersion lens used in these experiments, Chapter 6, the spot size is ≤ 1.5 μm, putting a lower limit on the size of the structures. Fabricating structures with lateral dimensions much bigger than this will, of course, limit the number of flakes that are large enough to span the void.

Typically, monolayer samples with dimensions larger than $\sim 10\ \mu$m are rare when searching on coverslides. The reason for this is unknown. Potentially, the roughness of the flame–polished surface of the coverslide is less adhesive than that of the thermally grown silicon dioxide surface, where deposited flakes with dimensions of the order $\sim 100\ \mu$m are common.

A mask is therefore produced with square holes of dimensions $2.5\ \mu$m, $3.5\ \mu$m and $4.5\ \mu$m. The separation between the squares (centre to centre) is $6.75\ \mu$m, $9.5\ \mu$m and $12\ \mu$m, respectively. This keeps the ratio of glass surface area to etched area at approximately $2.5 : 1$, ensuring there is plenty of area for the flakes to attach to. The mask itself is made from a glass substrate with a 400 nm anti–reflection coating on the underside and a reflective chromium layer on the top.

Using the mask, one is then able to produce patterned substrates via a photolithography process. A light–sensitive resist (S1813) is spun onto a glass coverslide covered with a thermally evaporated (~ 20 nm) layer of chromium, Figure 2.1.3(a). The chromium acts to protect the glass during etching and the photoresist to transfer the pattern from the mask.

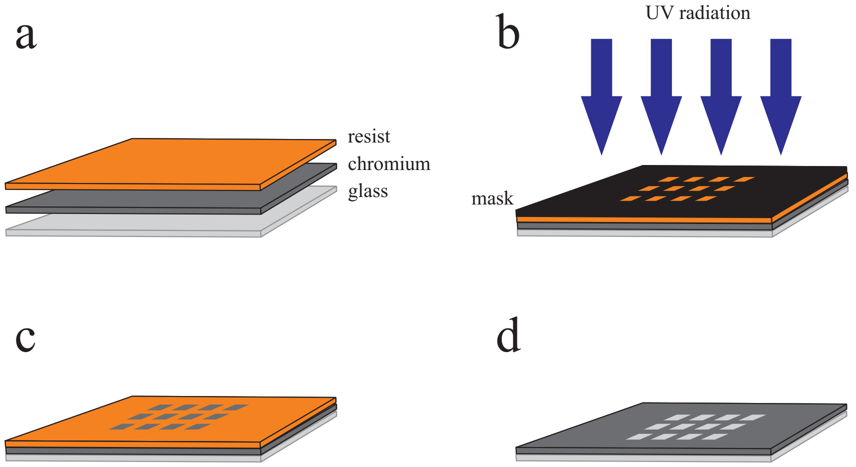

Figure 2.1.3: Fabrication of a patterned sample for reactive ion etching. (a) A thin layer of chromium is evaporated onto the glass, follwed by spin–coating of a light–sensitive resist. (b) The sample is placed into a mask aligner, covered with the desired mask and irradiated with ultra–violet radiation. (c) The sample is developed to remove those regions exposed to the light. A wet etch removes the chromium from within the holes. (d) The remaing resist is dissolved in acetone, leaving behind a chromium–protected patterned substrate.

The photoresist is dropcast onto the glass with a pipette and spun at 5500 rpm for 40 seconds. Baking on a hot plate for 1 minute at 115° C ensures the solvent within the resist is completely evaporated. This produces a layer approximately $1.1\ \mu$m thick. Thicker regions, near the corners, are removed with acetone and a cotton bud. The sample is then exposed to ultra–violet (UV) light in a mask aligner (Suss MicroTec MJB4) in hard contact mode. During this process, the sample and the mask are pressed together and the UV light exposes the regions of the sample not protected by the mask, Figure 2.1.3(b).

The resist is extremely absorbing in the UV range and the application of the radiation chemically changes the exposed regions. Subsequent development in MF319 developer for ~ 15 seconds removes the exposed areas; the mask pattern has then been successfully transferred, Figure@2.1.3(c). A wet etch of the chromium for ~ 60 seconds removes all unwanted metal from within the holes. The photoresist is then removed by sonicating in acetone to reveal the transferred pattern on the chromium–protected glass substrate, Figure 2.1.3(d).

Once these steps of fabrication are complete the sample is ready for etching. Samples prepared for etching with hydrofluoric acid, Section 2.1.3.2, do not require the chromium layer but are otherwise fabricated in the same way (without the last step of photoresist removal).

2.1.3.2 Wet Chemical Etching

The first attempt at suspending devices involves wet–etching a glass coverslip in a buffered oxide etching (BOE) solution, containing hydrofluoric acid (HF) and ammonium fluoride (NH_4F). A glass coverslip with an array of lithographically defined holes is etched in a $6:1$, by volume, ratio of 40% NH_4F and 49% HF in water. The use of a BOE, as opposed to just diluted HF, is to ensure a slower etching rate. Without the buffering solution the reaction is extremely fast and violent. This makes timing the etching difficult and may even break delicate samples due to the violent release of gas from the reaction.

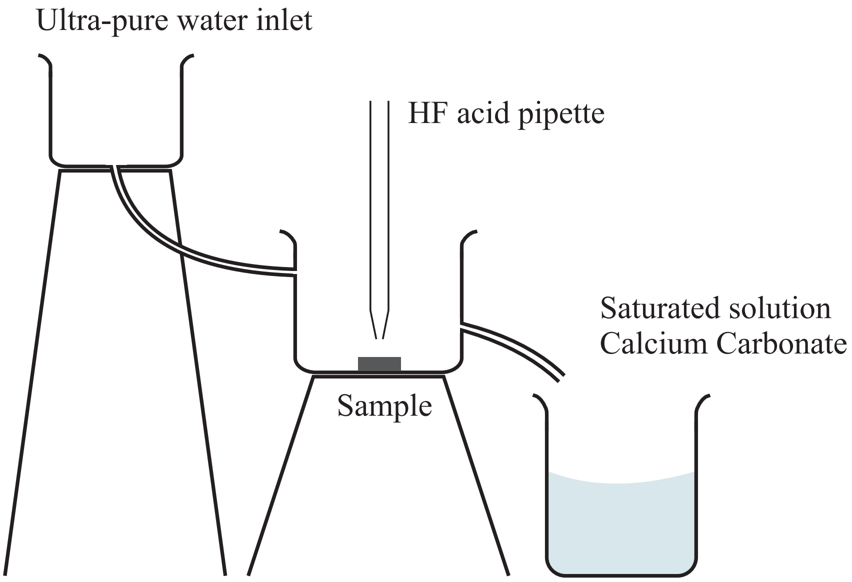

Figure 2.1.4: Apparatus used for wet etching substrates with hydrofluoric acid. The acid is slowly pipetted onto the sample and left for the desired amount of time. The top beaker is then flushed through with ultra–pure water to dilute the acid, which flows into the neutralising calcium carbonate beaker. This process is repeated until the acid had been sufficiently diluted, i.e. the reaction between the acid and alkali ceases. All beakers are made from PTFE so as not to be etched by the solution.

The use of hydrofluoric acid requires great care and attention due to its toxicity. Two fully trained operatives are required at all times, along with a calcium gel in case of contact with the skin. Layers of protective clothing, goggles and a face mask are required and the whole process must be performed on a clear wet bench with a sink, tap and fume hood. Polytetrafluoroethylene (PTFE) beakers must be used to prevent the solution from etching the apparatus.

Once the dried apparatus has been assembled, as shown in Figure 2.1.4, the sample is placed into the centre PTFE beaker. The acid is carefully added to the beaker with a precision pipette. Approximately 20 ml of solution is added for 30 seconds. The top beaker is then filled with ultra–pure water, which flows into the acid and begins to dilute it, stopping the etching. The output then flows into a neutralising solution of saturated calcium carbonate. The HF acid reacts with the calcium carbonate as follows,

$$\mathrm{CaCO_3} + 2\mathrm{HCl} = \mathrm{CaCl_2} + \mathrm{CO_2} + \mathrm{H_2O}. \tag{2.1.1}$$

When there is acid present in the output of the middle beaker, the production of carbon dioxide gas is visible as the acid and alkali react. The dilution of the acid is repeated until the reaction visibly stops. A further three full beakers of water are then flushed through to make absolutely sure the acid has been fully neutralised.

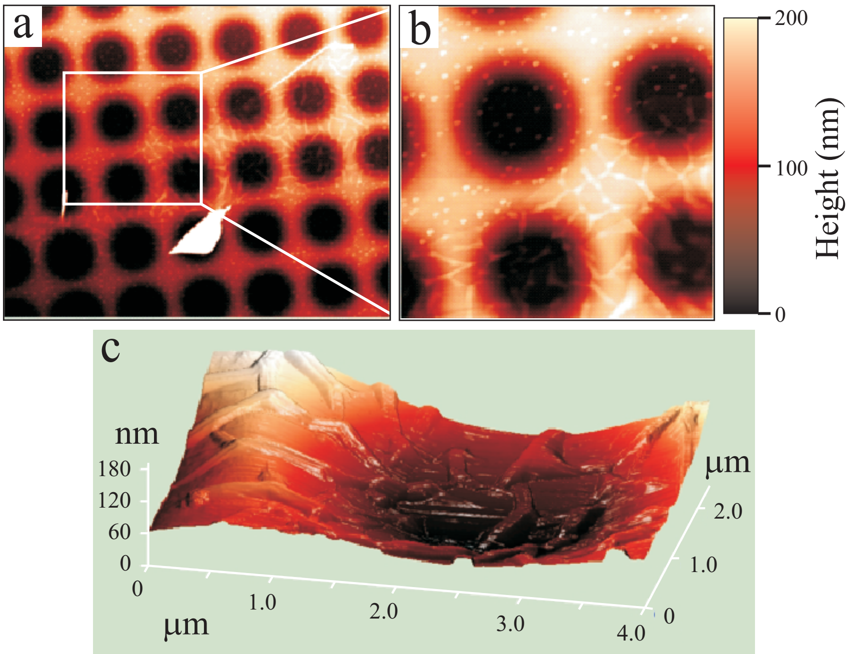

Figure 2.1.5: Atomic force microscope images of an attempted suspended flake on a HF–etched glass substrate. (a) AFM amplitude scan of a flake covering several etched holes. (b) The zoomed–in region from (a). (c) A high resolution scan of the flake within the etched region. The flake is clearly not suspended, but as a result of touching the substrate in all of the holes, it is forced to wrinkle.

After etching, graphene is deposited via the standard mechanical exfoliation technique, Section 2.1.1. Samples fabricated via this method have not produced suspended flakes. The HF etch is isotropic and so not only etches down into the substrate, but undercuts the masked regions. Figure 2.1.5 is an atomic force microscope (AFM) image of a typical HF–etched glass substrate with a deposited flake. The mask used here was 1.5 μm radius circles, separated by 4 μm (centre to centre). Although this method etched the glass to a depth of approximately 200 nm, the profile of the etch is extremely shallow and the flakes are found to be fully supported.

One interesting feature of these samples is the huge ripples found, Figure 2.1.5(c). Due to the periodic array of holes in both the $\hat{x}$ and $\hat{y}$ directions, for the flake to be able to touch the substrate everywhere it must ripple. This presents a useful method for the fabrication of intentionally rippled graphene samples, but does not provide the fully suspended samples that are required.

2.1.3.3 Reactive Ion Etching

To overcome the isotropic etching found with a wet chemical etch, suspended devices are fabricated using reactive ion etching (RIE). During this process, a sample is placed into a vacuum chamber and exposed to a large radio frequency (RF) electromagnetic wave between a top and bottom electrode. One or more gases are then vented into the chamber. The high power (up to 300 W) RF source causes the gases to ionise. Physical etching occurs due to the high kinetic energy of the ions in the presence of the accelerating field, producing a highly anisotropic etch profile. A chemical etch also removes material due to the highly reactive ions within the plasma.

To etch the glass coverslips, which are protected with a 20 nm patterned chromium mask, a mixture of 20 sccm (standard cubic centimetres per minute) of CHF_3 and 5 sccm of SF_6 are used. A PlasmaLab 80 Plus inductively coiled plasma (ICP) source is used with a forward power of 100 W and an ICP power of 150 W. Due to the physical and chemical nature of the etching, the power, gas pressure and duration of etching are all vital parameters but will vary from machine to machine. A 300 nm etch into the glass is obtained using a $3.5\ \mu$m square hole array for an etch time of 30 minutes. The protective chromium layer is then removed via a wet etch and the substrate is cleaned, Figure 2.1.6.

Once the substrate is cleaned one is left with a pristine glass substrate with a periodic array of sharp, etched holes. The rough profile of the bottom of the etched holes is unimportant, as any suspended flakes will have no knowledge of these regions. The area of glass protected by the chromium layer is returned to its pristine condition after a wet etch and so one is left with an ideal substrate for depositing flakes. The deposition of graphene follows with mono– and few–layer flakes being found and characterised.

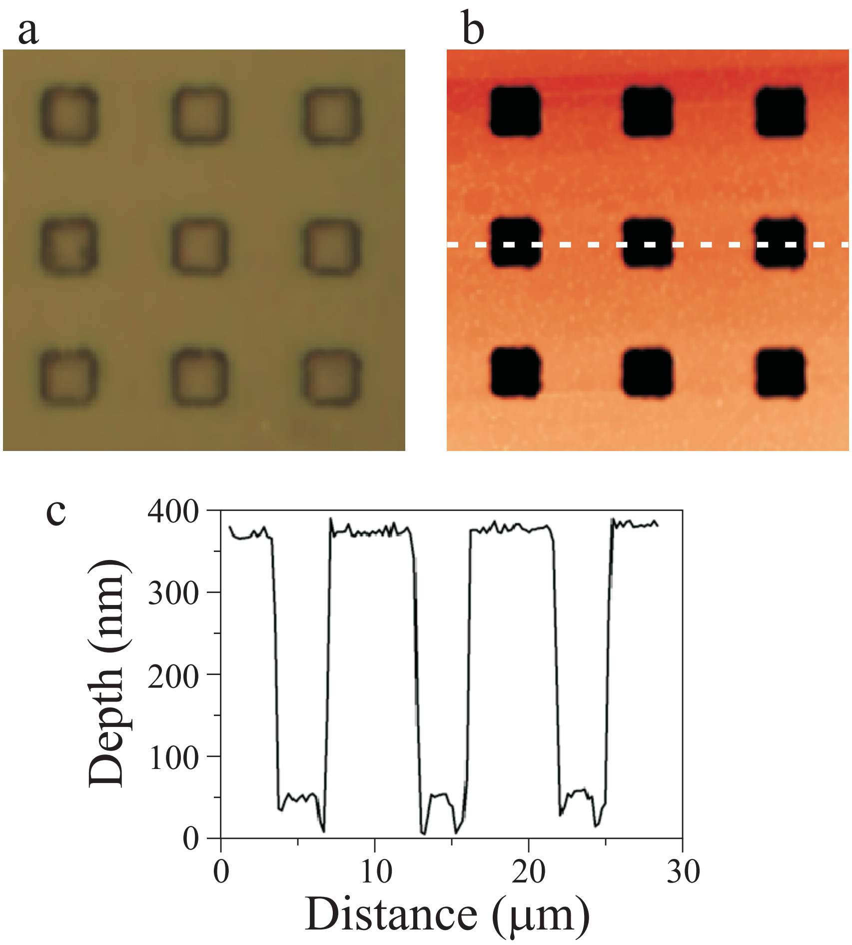

Figure 2.1.6: Images of a substrate after reactive ion etching, prior to deposition of graphene. (a) An optical image of the bare glass substrate showing the $3.5\ \mu$m etched holes. (b) An atomic force microscope image of the same region. The colour scale is $0 - 300$ nm. (c) Profile of the dashed line in the AFM image.

2.1.4 Contacted Samples

For all electrical measurements performed on graphene samples there is a requirement to fabricate devices in which the graphene can be integrated into a circuit. The following method is now a standard procedure for producing contacted graphene devices with a high success rate. For the vast majority of graphene samples that are fabricated, the substrate of choice is silicon with 300 nm of silicon dioxide thermally grown on top. To achieve thin, transparent substrates, the following technique uses glass coverslips, but the general procedure is identical.

Glass coverslides are first cleaned and a mask aligner is used to produce an array of $100\ \mu\text{m} \times 100\ \mu\text{m}$ separated chromium:gold crosses, see Section 2.1.3.1. These crosses are used as markers later in the procedure. Graphene is deposited via mechanical exfoliation and suitable flakes are found under an optical microscope. A schematic of the following procedure is illustrated in Figure 2.1.7.

An organic polymer resist, poly(methyl methacrylate), or PMMA, is spin–coated onto the substrate to create a uniformly thick layer. Under irradiation from an electron–beam source, exposed areas of PMMA break into shorter, more soluble chains. When placed into a developing solution it is then possible to remove the exposed areas, leaving behind all unexposed regions. This method, similar to the mask aligning procedure in Section 2.1.3.1, but with a much higher spatial resolution (~ 50 nm as opposed to ~ 0.5 μm), enables a pre–defined pattern to be transferred onto a given substrate. Whereas the mask aligning technique works well for regular arrays of samples with micron–sized dimensions, for the production of bespoke devices on a range of different flakes the electron beam system is more suitable.

An AutoCAD file is prepared to outline the shape of the contacts to be drawn onto the flake. This pattern is prepared in reference to the chromium:gold crosses deposited prior to the graphene. By doing this, the electron beam is not required to look directly at the sample during alignment, preventing exposure of unwanted areas.

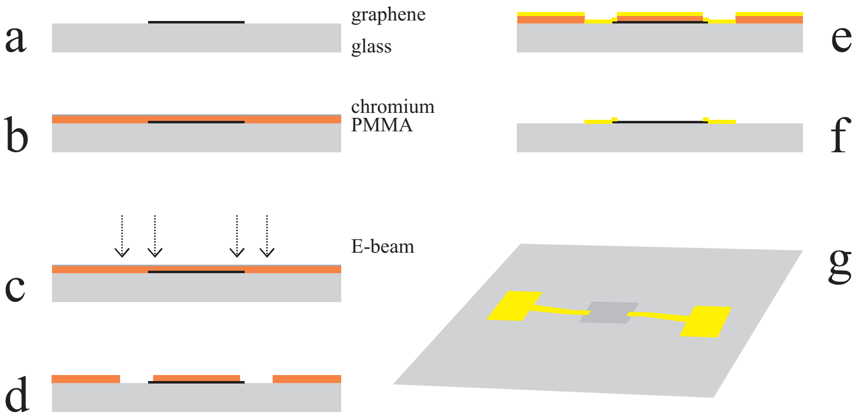

Figure 2.1.7: Schematic of the contacted sample fabrication procedure. (a) A graphene flake deposited onto a prepared glass substrate. (b) PMMA resist spun onto sample. (c) Exposure to electron–beam radiation with a pre–drawn pattern. (d) Development of sample to remove exposed areas of PMMA. (e) Evaporation of Cr, Au contacts. (f) Lift–off in acetone to remove all unwanted PMMA and metal. (g) Top view schematic of a completed device.

The sample placed into the electron beam chamber must be conductive in order to remove charging from the buildup of excess electrons that come from the electron–beam. For this reason, the samples prepared on glass coverslips have a thin, approximately 10 nm, layer of chromium evaporated onto the resist. This is connected to a ground within the chamber and removes all charging during exposure.

With an AutoCAD mask prepared, the sample is irradiated to break up the long–chain polymers within the selected regions. Subsequent development removes these areas,

Figure 2.1.7(d), and the sample is ready for metal deposition. Approximately 8 nm of chromium is evaporated onto the sample to provide an adhesion layer for the ~ 50 nm of gold which is evaporated on top.

The chromium and gold cover the substrate completely and are removed via overnight soaking in acetone. Any remaining PMMA is dissolved, lifting off the evaporated metal above it. All that remains is the flake and the contacts, Figure 2.1.7(f). Large bonding pads are drawn at the extremes of the flake contacts, which provide an area to connect bonding wires to. A Kulicke & Soffa ultrasonic wedge bonder is used to connect 25 μm thick gold wire to the bonding pads. The other end of the wire is then bonded to a firmer contact and can be connected to the required circuit.

For the measurements conducted in Section 7.1, there is a requirement for an optically transparent substrate. This takes full advantage of the transmission detector within the microscope setup and makes finding and measuring samples much easier. To achieve this, a bespoke sample holder is produced, Figure 2.1.8. A printed circuit board (PCB) is first cut into the required shape (to fit in the microscope holder) and a centre hole is drilled to enable imaging through the device.

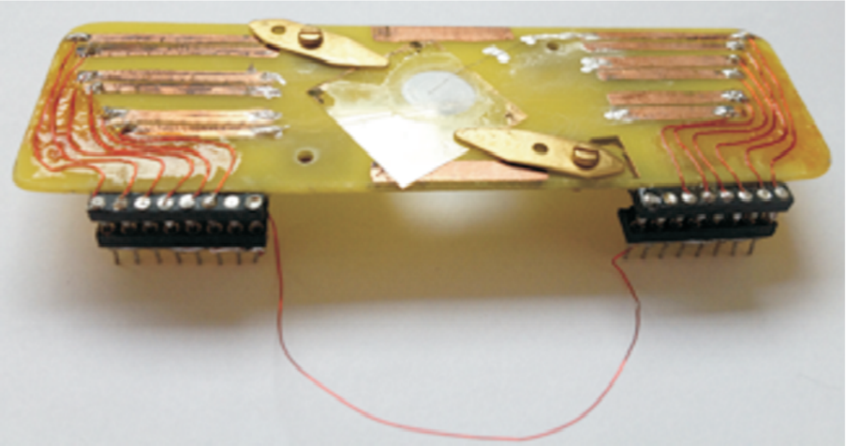

Figure 2.1.8: Image of the bespoke sample holder used for electrical measurements. The glass sample is held in place over the centre hole with up to four metal clamps. Twelve different copper tracks allow for multi–terminal devices to be connected via a wire bond. Each track is connected to a pin to enable the device to be incorporated easily into measurement setups. When not being measured, a grounding connector is attached to keep the entire device at the same potenital.

The circuit board consists of an insulating material with a thin copper coverage on the top and bottom. A felt tip marker pen is used to draw the regions on which the copper is required to stay. Submerging the board into a saturated solution of iron chloride ($FeCl_3$) removes the copper from the unprotected areas within approximately 5 minutes. The board is cleaned in acetone and one is left with a patterned device. Each remaining copper contact is soldered to a wire which, in turn, is soldered to a pin connector. The device can now be easily connected and disconnected into different measurement setups. For safety, a grounding plug, which connects all the pins together, is attached whenever the sample is not being measured. This prevents the sample from being destroyed due to different pins being at different potentials, causing a large current to flow through the sample.

2.1.4.1 Electrical Measurements

Electrical measurements are conducted via the constant–current measurement technique. This involves providing a large ballast resistor to the graphene circuit such that the modulation of the carrier density, and therefore sample resistance, during measurement does not change the overall resistance of the circuit. The current flowing through the device can therefore be assumed to remain constant.

Graphene samples typically show a resistance of the order 1 kΩ and so a 10 MΩ ballast resistor is used in conjunction with a 1 V alternating current (AC) source to apply a 100 nA current to the sample, Figure 2.1.9. A lockin amplifier is used to source this voltage. Measurement of the voltage drop between two contacts, which may or may not be the source and drain, allows the resistance of the sample to be calculated.

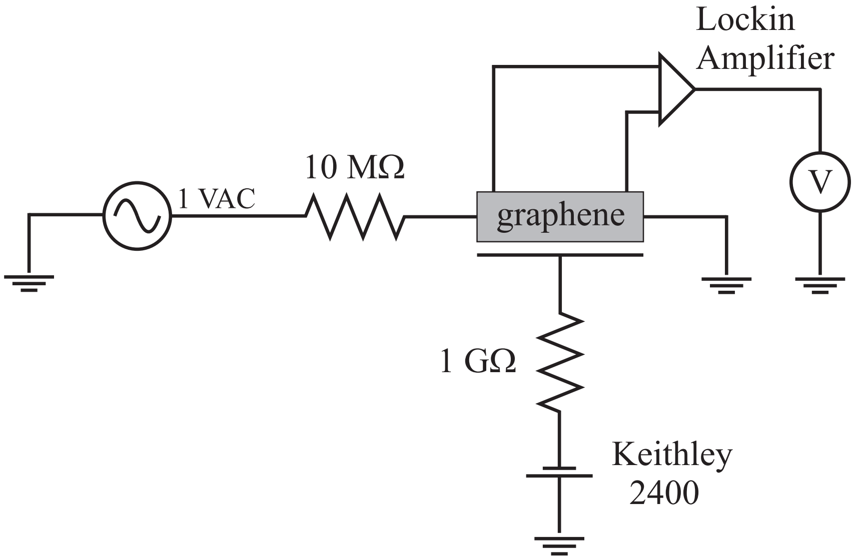

Figure 2.1.9: Circuit diagram of the constant–current measurement setup. A large ballast resistor prevents the resistance changes in the sample from altering the current flowing through the circuit. A lockin amplifier measures the potential drop across the flake, from which the resistance can be found. A Keithley 2400 provides a voltage to the back gate, V_{bg}, to modulate the carrier density.

Modulation of the charge density is achieved with the control of an externally applied electric field, which modifies the position of the chemical potential. For the majority of samples, a standard silicon substrate is used. The graphene is placed on a conducting silicon wafer, covered with an insulating oxidised layer, which electrically separates the flake from the substrate. A potential is created between the graphene and the conductive substrate using a Keithley 2400 SourceMeter. Electrons, or holes, are accumulated in the graphene via a capacitive coupling between the sample and the silicon. The number density of charge carriers per unit area, n, is given by

$$n = \frac{\epsilon V}{de}, \tag{2.1.2}$$

where $\epsilon = 3.9$ is the permittivity of the silicon dioxide layer, d is the thickness of the dielectric ($\sim$ 300 nm), and e is the electronic charge. It then follows that the number of charge carriers induced in this sample configuration is

$$n \approx 7.19 \times 10^{10} \left[\mathrm{cm}^{-2}/\mathrm{V}\right] \cdot \mathrm{V}_{\mathrm{bg}}. \tag{2.1.3}$$

By noting that graphene possesses a linear dependence of the Fermi energy, E_{F}, on the Fermi velocity, v_{F}, such that $\mathrm{E}_{\mathrm{F}} = v_{\mathrm{F}}\hbar k_{\mathrm{F}}$, one can substitute to find the dependence of the Fermi energy on applied gate voltage, V_{g}. The number density of electrons, n, is related to the density of states, $g(\mathrm{E})$, by

$$n = \int_0^{\mathrm{E}_{\mathrm{F}}} g(\mathrm{E}) d\mathrm{E}\,, \tag{2.1.4}$$

where, in two dimensions, $g(\mathrm{E})d\mathrm{E} = \mathrm{k}d\mathrm{k} \cdot (2\pi)^{-1}$. Substituting for the wavevector in graphene and applying the constants for the silicon dioxide layer, one finds the shift in Fermi energy as a function of applied back–gate voltage,

$$E_{\mathrm{F}} = 31 \left[\frac{\mathrm{meV}}{\mathrm{V}^{1/2}}\right] \cdot \sqrt{\mathrm{V}_{\mathrm{g}}}\,. \tag{2.1.5}$$

Here, a positive (negative) gate voltage produces an accumulation of electrons (holes) in the graphene, Figure 2.1.10.

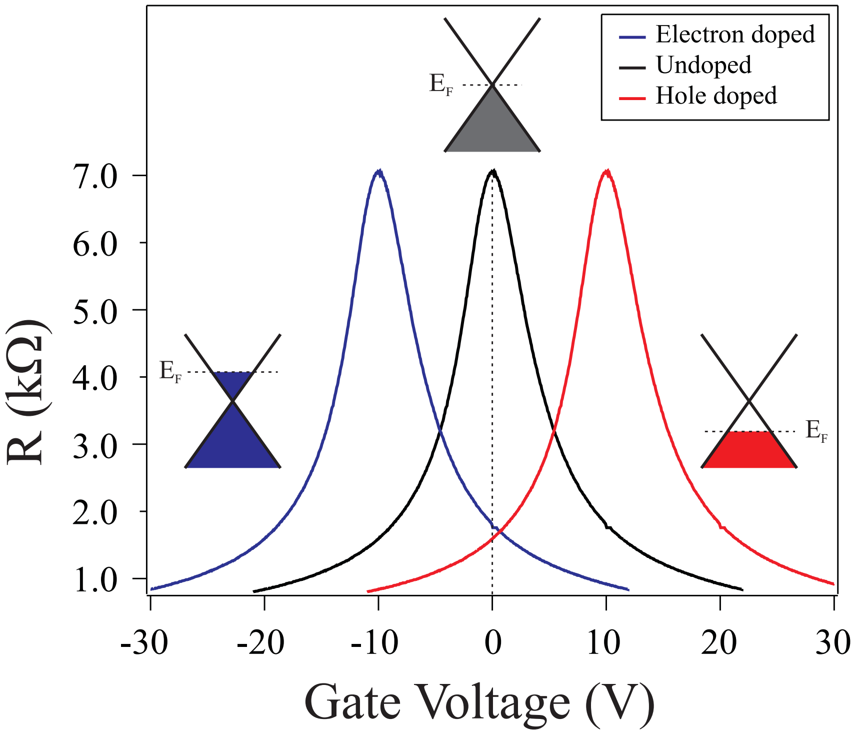

Figure 2.1.10: Resistance of a graphene sample as a function of applied gate voltage. Three examples are shown of a flake with electron doping (left, blue curve), no doping (black, centre curve) and hole doping (red, right curve). Sweeping the gate to change the Fermi level modifies the resistance of the sample, the maximum of which occurs when the density of states goes to zero at the charge neutrality point. This peak is only at zero applied voltage for undoped samples.

2.1.4.2 Electrolyte Gating

An alternative approach to gating the graphene involves the use of electrolytes. Instead of using capacitive coupling through a dielectric, where one is limited by the breakdown field, liquid and solid electrolytes may be employed to enhance the gating range[60–64]. Typically, for samples fabricated on oxidised silicon wafers, one observes breakdown of the dielectric for applied fields of approximately 100 V. This puts an upper limit on the carrier densities that can be reached to $\leq 1 \times 10^{13}$ cm^{-2} and a shift in the Fermi energy of $\sim$ 300 meV. For transport measurements this is more than sufficient, but optically this corresponds to a photon wavelength of 2 μm, well out of the visible range. In order to obtain an optically observable shift, one must increase the Fermi energy shift.

Electrolyte gating enhances the magnitude of shift in Fermi energy by reducing the distance between the graphene and the other conductive capacitor plate. When standard silicon dioxide substrates are employed, this distance is typically 300 nm. Electrolytes contain free ions which are able to migrate, under the influence of an applied potential, to the graphene surface. This reduces the distance between the effective capacitor plates to approximately 1 nm[60], therefore increasing the efficiency of the gate control.

In this work, a mixture of 1 : 8, by weight, of lithium perchlorate ($LiClO_4$) and polyethelyne oxide (PEO) provide the solid electrolyte. The two compounds are sonicated in methanol and dropcast onto a device, Figure 2.1.11.

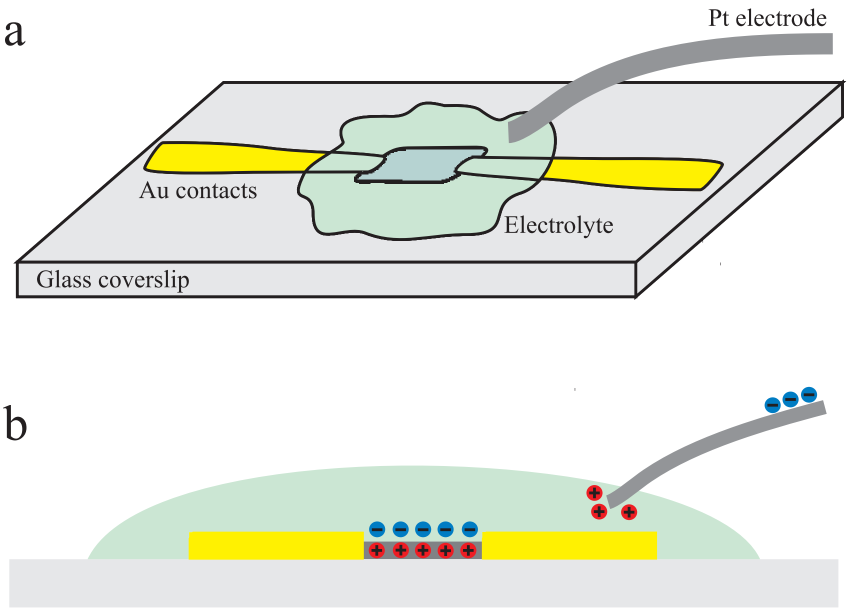

Figure 2.1.11: Schematic of a contacted graphene sample on a glass coverslip. (a) Top view. (b) Side view, showing the areas of accumulated charge due to the application of a negative potential to the platinum electrode. With a negative (positive) potential applied, holes (electrons) are induced into the flake.

The methanol is used to disperse a thin, uniform layer of the solid electrolyte over the device. The sample then is dried in ambient conditions. A platinum electrode is used to control the carrier concentration in the graphene as it does not react with the ions.

The Li^+ and ClO_4^- ions within the electrolyte are manipulated with the application of an electrode voltage. Applying a negative (positive) voltage to the electrode induces electrons (holes) into the graphene. This can be used to shift the Fermi level from the Dirac point by more than 800 meV with an electrode voltage of approximately 4 V[65]. This corresponds to an electron concentration of 5×10^{13} $cm^2V^{-1}s^{-1}$, a five–fold increase in the carrier concentration one is able to achieve with silicon dioxide back gates with only 4% of the applied field.

2.2 Ultrafast Optical Measurements

Two types of ultrafast, nonlinear, optical measurements are utilised in this work and are described in this section. For all types of nonlinear measurements, the signal intensity is strongly dependent on the incident intensity. Achieving high intensity, monochromatic laser radiation onto a sample is straightforward, but can result in damaging delicate samples before nonlinear effects can be observed. Pulsed lasers are therefore hugely important for the investigation of nonlinear effects due to their high peak intensity and low average power. Three types of pulsed laser systems are employed here and are discussed below, followed by an introduction into the measurements that they can be utilised for.

2.2.1 System Operation

Three separate ultrafast laser systems are employed in this work, each with their own advantages for certain types of measurement. Within these systems one is able to tune the emission wavelength from 690 nm – 2300 nm, with pulses ranging from 100 fs to 6 ps. An inverted microscope with scanning mirrors allows for micron resolution images to be taken of either linear or nonlinear processes in both the reflection and transmission directions.

2.2.1.1 Levante Optical Parametric Oscillator

For the nonlinear imaging experiments in Chapters 3, 4 and 5, a Levante (High-Q Picotrain) optical parametric oscillator (OPO) is used. A neodymium–doped yttrium orthovanadate (ND:YVO$_4$) seed laser produces 6 ps pulses at a wavelength of 1064 nm, with a repetition rate of 76 MHz and a maximum power of 10 W. This output is frequency doubled to 532 nm to excite a nonlinear crystal within the OPO. OPO's are particularly useful for nonlinear measurements as they are able, (with the use of nonlinear crystals with high second order susceptibilities) to convert one incoming photon into two lower energy photons. By varying the temperature and phase matching condition of the crystal, one is able to tune the wavelength of the output photons over a broad range. For this system, the higher energy (signal) photon has a wavelength range from 690 nm – 990 nm and the lower energy (idler) has a range of 1150nm – 2300 nm. The two photons are linked due to the condition that the frequency of the incoming pump photon must be equal to the sum of the outgoing signal and idler frequencies, i.e. $\omega_{\text{pump}} = \omega_{\text{signal}} + \omega_{\text{idler}}$. The signal and idler frequencies are therefore linked and can not be changed independently. To circumvent this, one may take advantage of the 1064 nm output from the seed laser and combine this with one (or both) of the OPO outputs, thus removing the tie between the signal and idler.

The pulses are aligned into an inverted optical microscope where the spatial resolution is of the order 1 μm and detection can be made in both reflection and transmission.

2.2.1.2 Mira 900D

For the pump–probe experiments in Chapter 6 and Section 7.1, a Mira 900D Ti:sapphire (Coherent) laser is used. A 532 nm V10 Verdi pump laser is used as the seed and the system is tunable between 660 nm and 990 nm, with a pulse width of ~ 200 fs and a repetition rate of 76 MHz.

When conducting the pump–probe measurements, the Mira is tuned to 830 nm as it provides the input for a Mira OPO (Coherent) with a wavelength range of 1100 nm to 1600 nm. The pulse duration is approximately 250 fs with a maximum power output of 300 mW. This longer wavelength output is utilised as the lower energy probe in the measurements.

For second–order nonlinear imaging the Mira is tuned to 800 nm. 400 nm band–pass filters are then used to detect the nonlinear emission from samples.

Similar to the Levante system, these outputs are aligned into an inverted microscope for micron–scale resolution imaging in both reflection and transmission.

2.2.1.3 Legend Elite

For the silicon carbide experiments outlined in Section 2.2.3, a regenerative amplifier (Coherent Legend Elite) is used. A Coherent Vitesse is pumped from a 532 nm seed laser to generate 85 fs pulses at a repetition rate of 80 MHz and a centre wavelength of 800 nm. These pulses enter the Legend Elite which acts as a separate cavity for amplification of the individual pulse energy.

Pulses enter the regenerative amplifier with an energy of approximately 12 nJ at a repetition rate of 80 MHz. The amplifier first selects individual pulses at a reptition rate of 1 kHz, stretches them using a grating before sending them around the Legend cavity multiple times for amplification. Broadening the pulses in time first prevents damaging the gain media in the cavity due to the large instantaneous pulse intensity that would be created. After approximately 20 round trips of the cavity the pulses are switched out and recompressed to a 100 fs pulse via a second grating. Although the pulse repetition rate is considerably reduced down to 1 kHz, the individual pulse energy is increased to 3 mJ. This huge increase in instantaneous pulse intensity is extremely valuable when looking at nonlinear processes.

Unlike the two previous systems, the Legend Elite output does not have a microscope for high spatial resolution. Measurements performed with this system involve much larger spot sizes and so large–area samples are required. A spot size of approximately 20 μm can be achieved with the use of high powered lenses, but for the large samples measured one tends to average the signal over a wider area and use millimetre–sized spots.

2.2.2 Degenerate Four–Wave Mixing Experimental Technique

Degenerate four–wave mixing is a third order nonlinear measurement involving a pump (signal) pulse of frequency ω_1, a probe (idler) pulse, ω_2, and an emitted pulse of frequency ω_e. For the special case of degenerate four–wave mixing, two pump photons are involved and the emitted photon has a frequency corresponding to the energy conservation, $\omega_{\mathrm{e}} = 2\omega_1 - \omega_2$.

The beam paths for the measurement are indicated in Figure 2.2.1. Alignment of the setup is of vital importance due to the nonlinear dependence of the emission signal on input intensity. If the pump and probe focal spots are not overlapped spatially in the x–y plane, ẑ direction or temporally, then the signal magnitude will fall off as the cube of the overlapped intensity.

The two beams are first aligned through a pair of widely spaced pinholes (greater than 2 metres apart) to ensure they are collinear. The collimation of the two beams is checked to ensure they are the same, if one beam were to be collimated differently this would change the focal position in the ẑ direction and result in a loss of signal magnitude. A set of beam expanders are used to enlarge the beams, thus ensuring the back aperture of the objective lens is filled, giving the smallest possible spot size at the sample.

The beams are then passed into an inverted microscope (Olympus IX71) through a Fluoview 300 confocal scan unit. Galvanometer scan mirrors within the unit oscillate to raster the beams through the objective, enabling imaging. An Olympus UPLSAPO 60× 1.2 numerical aperture (NA) water immersion objective lens is used, which gives a spatial resolution of $\sim 1\ \mu$m and a full scan area of $250\ \mu$m $\times$ $250\ \mu$m.

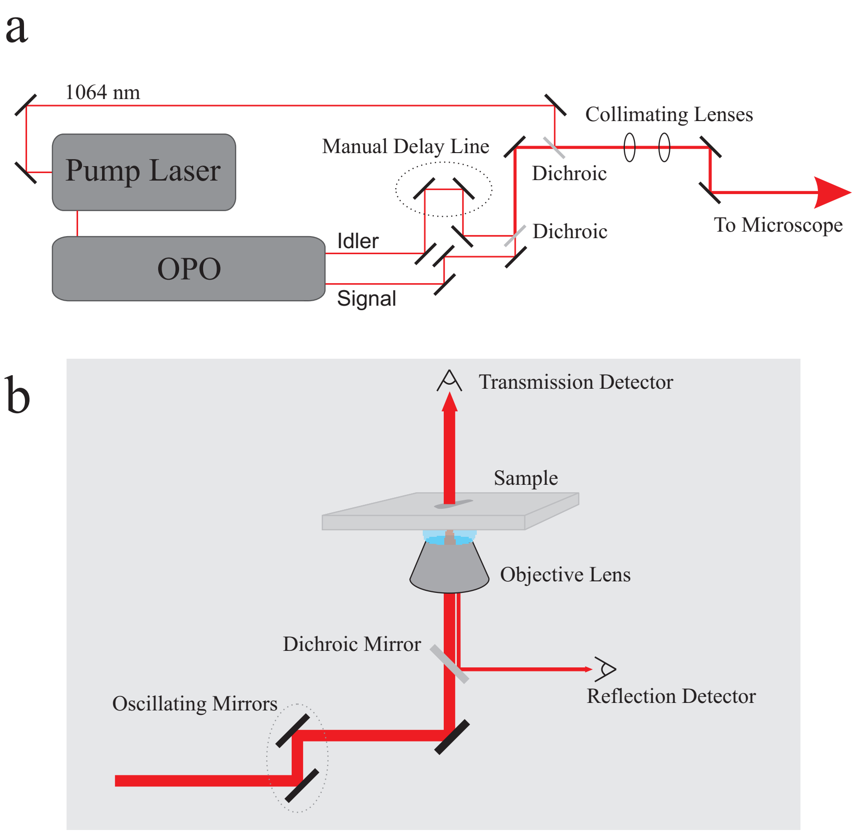

Figure 2.2.1: Simplified schematic of the four–wave mixing experimental setup. (a) Beam path alignment for the Levante OPO system. The signal and idler beams are combined at the first dichroic mirror and aligned into the microscope. A combination of 1064 nm and signal can also be used for higher resolution imaging. In both cases the collimating lenses ensure the back aperture of the objective lens is filled. (b) Schematic of the internal microscope alignment. The beams first pass through galvanometer mirrors which oscillate to raster the beam, enabling imaging. The high numerical aperture of the water immersion lens allows for a focal spot of $\sim 1\ \mu$m. Data can then be collected in both the forward (transmission) and epi (reflection) directions.

Overlapping of the signal and idler pulses in time is achieved with a manual delay line in the idler path. This is adjusted such that the temporal alignment is exact and is a useful check for confirmation of nonlinear signal, i.e. does the signal disappear when the delay is altered.

Since the efficiency of producing nonlinear signals is small, many orders of magnitude lower than Rayleigh scattering, a precise set of optical filters are required to distinguish between the different frequencies. Filters are chosen to reflect or transmit in specific wavelength ranges. For example, the dichroic filter within the microscope, Figure 2.2.1(b), is chosen to transmit both the signal and idler frequencies but preferentially reflect only the emission frequency onto the detector. High extinction band pass filters are placed in front of each detector to further block the transmission of the laser frequencies by a factor $\sim 10^5$.

In reflection, a photomultiplier tube (PMT) (Hamamatsu R3896) collects the light that is able to pass through the filters and produces a nonlinear image. A condensing lens collects the transmitted light onto a second PMT, again through a set of high extinction band pass filters.

With the use of the Fluoview software package, one is able to manipulate the beams and take a range of different measurements. The area of a scan can be varied up to a full field of view of $250\ \mu$m $\times$ $250\ \mu$m. Adjustment of the focal plane enables depth scans to be taken, the duration of a scan can also be varied, as well as the number of accumulations to average over. One may also select a specific region of the image to raster, giving the option to preferentially investigate one particular micron–sized portion of the sample.

2.2.2.1 Spectrometer

To ensure the signal being measured is truly nonlinear, a spectrometer is employed to analyse the wavelength of light being emitted by the samples. When measuring nonlinear samples with a photomultiplier tube, the signal recorded is simply a measure of the intensity at a point on the image. No information regarding the wavelength of the photon is known. To be certain of nonlinear processes, a full spectra must be taken to ensure that the expected emission wavelength (in this case $\omega_{\mathrm{e}} = 2\omega_1 - \omega_2$) is indeed observed.

An Andor Technology Shamrock SR-303i spectrometer, with an Andor iDUS charge coupled device (CCD) camera, is aligned in place of the reflection detector. The CCD is cooled to -55°C to remove noise. A diffraction grating disperses the incident light onto the CCD and a spectrum is obtained.

2.2.3 Time–Resolved Pump–Probe Measurement Technique

The principle of the pump–probe technique revolves around the control of the delay between two ultrafast pulses. A weak probe pulse is measured under the influence of an intense pump pulse. By varying the time at which the pulses arrive at the sample, one can monitor the time–dependent change in the transmission (or reflection) of the probe due to the presence of the pump.

The intense pump acts to photoexcite the sample. Figure 2.2.2 illustrates the process with respect to the low energy dispersion in graphene. When an instantaneous pulse is absorbed by a graphene sample, electrons are excited from the valence to conduction band. This leaves available states in the valence band and occupied states high in the conduction band. Eventually, these hot, excited electrons will find a path back to the low energy states in the conduction band. The power of time–resolved pump–probe spectroscopy is the ability to monitor this process, via the modulation of the probe pulse, and gain an insight into the ultrafast relaxation dynamics of different systems.

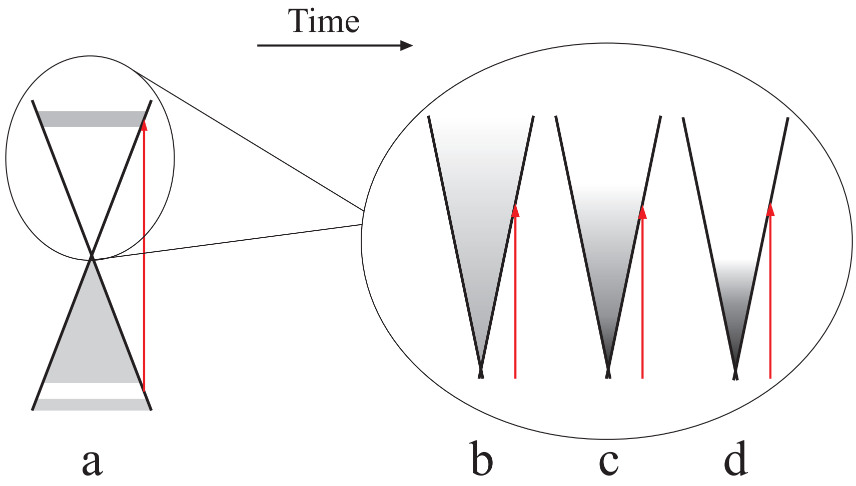

Figure 2.2.2: (a) The electron and hole distributions at the K point in graphene immediately after excitation from an ultrafast pulse. (b) Evolution of the electron distribution in the conduction band, as a function of time, as the electrons begin to scatter and form a distribution within the band, ≤ 100 fs. (c) Once a distribution is formed, electron–phonon interactions dominate the relaxation. (d) The system continues to evolve on the timescale of picoseconds. Once all the excited electrons have relaxed, the unperturbed electron and hole distributions are recovered in both the conduction and valence bands.

In graphene one observes two distinct timescales. A fast component, of the order ≤ 100 fs and a slower component, of the order ~ 3 ps. Early experiments attributed these timescales to electron–electron and electron–phonon scattering[66,67], whereas more recent works[68–76] show the biexponential decay dynamics are in fact attributed to electron–electron scattering and the decay of hot optical phonons.

The electron–electron scattering rapidly forms a distribution of electrons through the conduction band, Figure 2.2.2(b). The fastest way for the electron distribution to relax is then via optical phonon scattering, which eventually relaxes all the electrons to their original valence band states.

Time–resolved measurements are achieved by aligning the pump beam on a motorised delay line. As the path length of the pump beam is altered, so is the time taken for the pump pulse to arrive at the sample. An example of the experimental setup used in Chapter 6 and Section 7.1 is illustrated in Figure 2.2.3(a). The two separate beam paths can have arbitrary lengths up until the dichroic mirror, at which point the beams are collinearly aligned. The use of a moveable delay stage enables one to adjust the path length until the pulses from the pump and probe are temporally overlapped at the dichroic mirror, and therefore the sample.

The probe signal is collected in reflection and focussed onto a diode, Figure 2.2.3(b), the output of which is fed into a lockin amplifier. The mechanical chopper, placed in the pump path, sends a reference frequency (~ 820 Hz) to the lockin amplifier. The signal measured from the diode, at the chopper frequency, is auto–phased to the maximum real value to reveal the differential reflectivity of the sample.

Figure 2.2.3(c) is a schematic of the pump and probe pulses incident onto a sample. By varying the position of the delay stage the two pulses can be separated in space, and therefore in time. The shift between the pulses is denoted as δt. By elongating the pump path, causing the pump beam to take longer to reach the sample, the pulses become overlapped, this corresponds to $t = 0$ in Figure 2.2.3(d). At this point the two pulses arrive on the sample together, the intense pump pulse excites electrons into the conduction band, blocking available transitions for the probe. In transmission (reflection) this is observed as a positive (negative) peak.

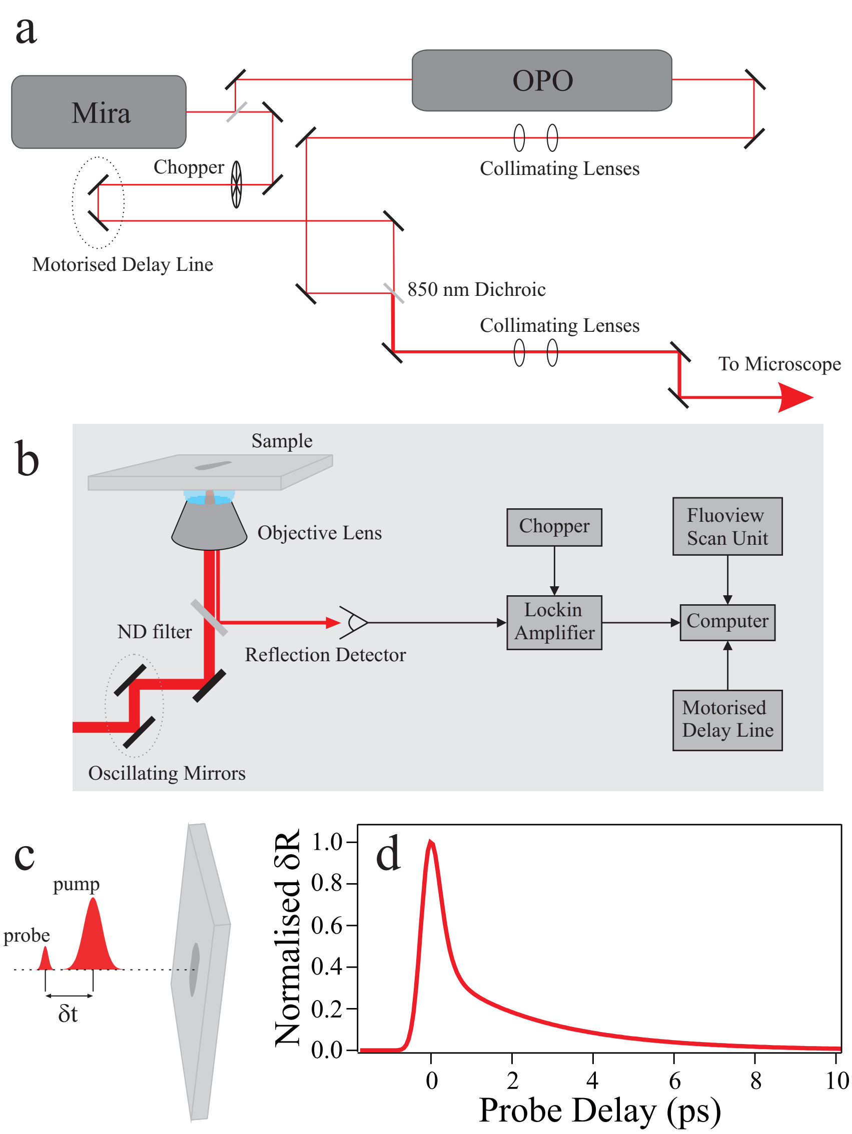

Figure 2.2.3: Schematic of the collinearly aligned pump–probe experimental setup with the Mira 900D and Mira OPO. (a) Alignment of beam paths entering the microscope. (b) Probe light is detected in reflection and sent to a lockin amplifier. A mechanical chopper (in the pump beam) provides the reference frequency for the measurement. A motorised delay line varies the temporal overlap of the pump and probe pulses which is fed into a LabView program to collect the differential reflection data. The Fluoview scan unit ensures the beams are only scanned over the desired area. (c) Schematic of the delayed pulses arriving at a sample. (d) A typical measurement of differential reflection as a function of probe delay for a graphite sample.

The system now evolves as a function of time. This is measured by further delaying the pump pulse until the change in reflection (or transmission) has returned to zero, i.e. the electron distribution has returned to its original state. Analysis of the shape of the response returns information about the system being probed.

Time resolved pump–probe spectroscopy is achieved in two experimental setups. For the work carried out in Chapter 6 and Section 7.1, the inverted microscope is employed, similar to the degenerate four–wave mixing alignment in Section 2.2.2. The alignment of the beam paths is illustrated in Figure 2.2.3. The ability to have a micron–sized focal spot and a range of different wavelength femtosecond, near–infrared pulses is of great use. The scanning mirrors also enable one to selectively measure individual samples, a key reason for utilising this apparatus.

To further illustrate the pump–probe measurement technique, an example measurement of large–area epitaxial graphene on silicon carbide is described. For this particular measurement one is able to measure with the Legend Elite system, since the samples are of large area.

2.2.3.1 Pump–Probe Measurements on Graphitised Epitaxial SiC

Initial experiments, performed on large area SiC, are conducted utilising the Legend Elite amplified system. This provides a high temporal resolution (pulse FWHM $\sim$ 100 fs) combined with extremely high intensity pulses. A schematic of the pump and probe beam paths is illustrated in Figure 2.2.4.

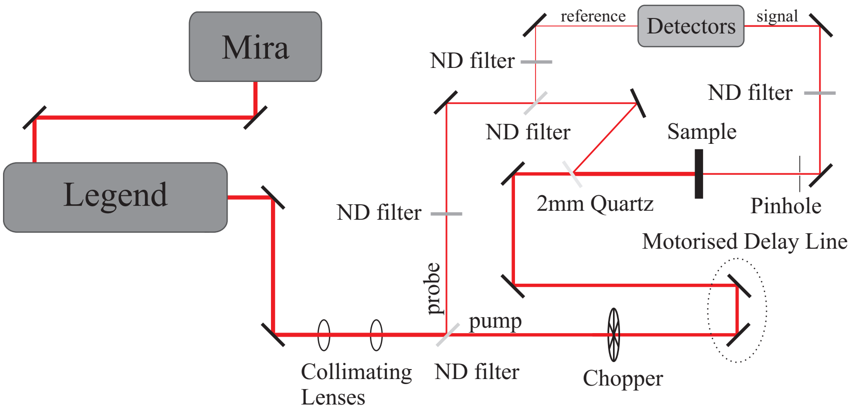

Figure 2.2.4: Schematic of the collinearly aligned pump–probe experimental setup with the amplified Coherent Legend Elite. The beam is first split with a neutral density filter into an intense pump and a weak probe path. The delay line is used to find the temporal overlap of the pump and probe pulses, while the use of two detectors allows for a balanced detection experiment. The pump beam is slightly angled such that it does not pass through the small pinhole and reach the signal detector.

The pump and probe paths are separated with a neutral density (ND) filter. The pump beam passes through a mechanical chopper, locked to half the frequency of the Legend system (525 Hz), through the delay line retro–reflector and onto the sample through a thick quartz slide. The probe beam follows a separate path to the sample and a fraction of the beam is split into a reference detector. The probe reflects off the quartz and is aligned into the centre of the pump spot on the sample. The use of thick quartz allows one to readily distinguish between the reflection from the front and rear faces.

The sample is placed onto an XYZ micrometre stage with the carbon–terminated face facing towards the laser. The beams are collinearly aligned through the transparent sample onto a small pinhole approximately 60 cm away. To remove any noise from the pump it is misaligned slightly so as not to pass through the pinhole. A weak lens is placed into both beam paths to bring them to focus at the pinhole. This allows for a narrow aperture and so the smallest misalignment of the pump.

The amount of light incident onto the signal and reference detectors is controlled with neutral density filters. A radial filter in front of the signal detector is adjusted to allow for a balanced detection. A change in the amount of incident light onto the signal diode can then be accurately measured. Fluctuations from the laser are removed with the use of the reference diode.

The diodes are connected to a lockin amplifier and measured at the chopper frequency. The difference between the outputs of the two is measured as a function of time (or position of the delay line).

For these measurements the pump and probe beams are both fixed at 800 nm. This is found to cause a large, instantaneous signal from the silicon carbide bulk. In order to extract the ultrafast signal originating from the graphene layers, one must first remove the background. Considering the attenuation of the pulses through the layers, a simple subtraction of a blank silicon carbide measurement is not sufficient. The correct subtraction has the form

$$\mathrm{S_{graphene}} = \mathrm{T'} - \mathrm{T} \cdot 0.977^{\mathrm{N}} \tag{2.2.1}$$

where S_{graphene} is the signal arising purely from the graphene layers, T' is the signal from the entire graphitised sample, T is the signal through the reference sample and N is the number of layers. The full derivation is shown in Appendix A.

The silicon carbide sample is found to have a coverage of approximately six layers, see Appendix A. The sample is measured with pump and probe spot sizes of 4 mm and 1 mm respectively, ensuring the area being probed is uniformly illuminated by the pump. The pump is incident with 5.4 mW resulting in an energy per unit area (fluence) of approximately 10^{-1} Jm^{-2}. The probe is incident with 150 nW, which corresponds to a fluence of approximately 10^{-3} Jm^{-2}, well below the pump fluence so as not to perturb the electron distribution.

Figure 2.2.5 illustrates a differential transmission measurement of the silicon carbide sample. A step size of 20 fs and a lockin time constant of 300 ms are used. The step dwell time is set to 500 ms.

One first observes a large differential transmission signal at $t = 0$ and a large, unexpected, feature at $t = 6.5$ ps. This arises from the reflection of the pump pulse from the back interface of the sample, which re–excites the carbon layers on the front face. Since the substrate is approximately 400 μm thick, with a refractive index of ~ 2.65, the feature is confirmed as a pump reflection.

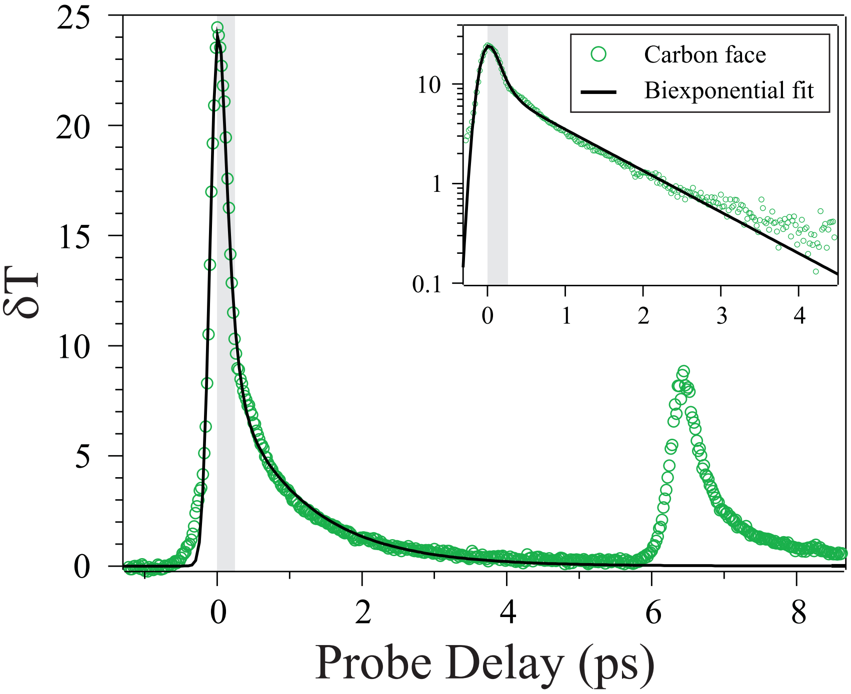

Figure 2.2.5: Differential transmission as a function of probe delay for epitaxial graphene on SiC. Pump and probe wavelengths are 800 nm. The ultrafast response from the silicon carbide has been removed and the data fitted with a biexponential decay, convoluted with the Gaussian profile of the pulses. The feature at 6.5 ps is due to the reflection of the pump pulse from the back interface re–exciting the sample. Inset: The same data plotted on a logarithmic scale. The two timescales can readily be observed. The grey area indicates the faster relaxation component.

To fit the data, a biexponential decay of the form

$$\Delta\mathrm{T} = \mathrm{A}e^{-t/\tau_1} + \mathrm{B}e^{-t/\tau_2} \tag{2.2.2}$$

is convoluted with the Gaussian profile of the excitation pulses. Here, ΔT is the increase in signal magnitude, A and B are the amplitudes of the two exponential terms and τ_1 and τ_2 are the decay rates. The FWHM of the pulse is fixed at 100 fs.

The convoluted biexponential fit returns a fast relaxation rate $\tau_1 = 106$ fs and a slower $\tau_2 = 1.05$ ps. This simple fitting function, with no knowledge of the system other than the pulse width and the nature of the biexponential decay, returns remarkably good results compared to the more complete fitting function used in Chapter 6.

One can immediately see that even with the ultrafast pulses from the Legend Elite system, the initial relaxation in the sample can not be resolved (FWHM $\sim$ 100 fs). The thermalisation of charge carriers is extremely fast in graphene, as will be seen in Chapter 6, allowing one to measure with broader pulses when the investigation of carrier thermalisation is not the goal.

2.3 Raman Spectroscopy

Raman spectroscopy is an extremely powerful tool for a quick and non–invasive characterisation of monolayer samples, see Section 1.4.3. A Renishaw RM1000 Raman microscope is used to collect the spectral data. A 50 mW, 532 nm continuous wave laser is used to illuminate the samples through a 50× objective lens, resulting in a spot size of $\sim$ 1 μm. A high extinction 532 nm edge filter prevents the intense laser reflection from passing through to the grating. Raman–shifted light is then dispersed onto a CCD and a spectrum of signal intensity against Raman shift (measured in cm^{-1}) is plotted.

The system has a resolution of $<$ 1 cm^{-1} and so enables the user to readily distinguish between the 2D profiles of monolayer graphene (FWHM $\sim$ 30 cm^{-1}) and bilayer graphene (FWHM $\sim$ 55 cm^{-1}).

To prevent photodamage from the laser, a 10% transmission filter is placed in the beam. Calibration of the system is performed on the intense, 520 cm^{-1} silicon peak, prior to measurements. This ensures the absolute shifts measured are comparable.

Chapter 3

Coherent Nonlinear Optical Response of Graphene

3.1 Introduction

In this chapter, the third–order nonlinear optical response of exfoliated graphene is measured for the first time. It is found that, at near–infrared frequencies, graphene exhibits a remarkably high third–order optical nonlinearity, $\chi^{(3)}$. For the wavelength range studied, the magnitude of $\chi^{(3)}$ is weakly wavelength dependent and is several orders of magnitude larger than the third–order response of typical dielectric materials. For this reason, the nonlinear emission from graphene can be utilised for high contrast imaging, with a flake contrast several orders of magnitude higher than for standard white light reflection microscopy.

It has been shown theoretically that graphene should demonstrate strongly nonlinear optical behaviour at THz frequencies[77], which could lead to important device applications. In this chapter it is shown that the third–order nonlinear optical response, described by the nonlinear susceptibility $|\chi^{(3)}| \sim 10^{-7}$ esu (electrostatic units), is comparable to that of other strongly nonlinear materials, such as carbon nanotubes[78–82]. In contrast to carbon nanotubes[82], however, this nonlinear response is essentially dispersionless over the available wavelength range in these experiments (emission with wavelength of $760 - 840$ nm).

The large response from graphene is quantified via a comparison with another strongly nonlinear material, a thin film of gold. Quantum kinetic theory is employed to estimate the magnitude of the expected response and is in good agreement with the experimental data.

3.2 Nonlinear Measurement

To investigate the nonlinear response of graphene, the four–wave mixing technique[83] is employed, see Section 2.2.2. Figure 3.2.1 illustrates the principle of the method: two incident pulses with wavelengths λ_1 (signal, tunable from 670 nm to 990 nm) and λ_2 (idler, tunable from 1130 nm to 1450 nm) are focused collinearly onto a sample and mix together to generate a third, coherent beam of wavelength λ_e. The pump beams are generated by an optical parametric oscillator which results in collinear, 6 ps pulses, which overlap in time. The incident pump pulses are focused onto the sample using a water immersion objective lens, with a numerical aperture of 1.2, giving rise to excitation powers at the sample of approximately 1 mW.

The nonlinear emission is collected in the backward direction using an 850 nm long–pass dichroic mirror, followed by a 750 nm band pass filter (210 nm bandwidth), used to isolate the nonlinear emission from the pump beams. The emission is detected by either a red–sensitive photomultiplier tube (for imaging) or by a spectrometer. Imaging is achieved via raster scanning of the excitation beams over the sample and acquiring the emitted signal as a function of its position. Images consisting of 512×512 pixels are acquired with a pixel dwell time of 2.6 μs, resulting in an image frame rate of approximately 0.6 seconds. To acquire a spectra of the samples, the signal is instead focussed into a spectrometer. The signal intensity as a function of wavelength may then be measured.

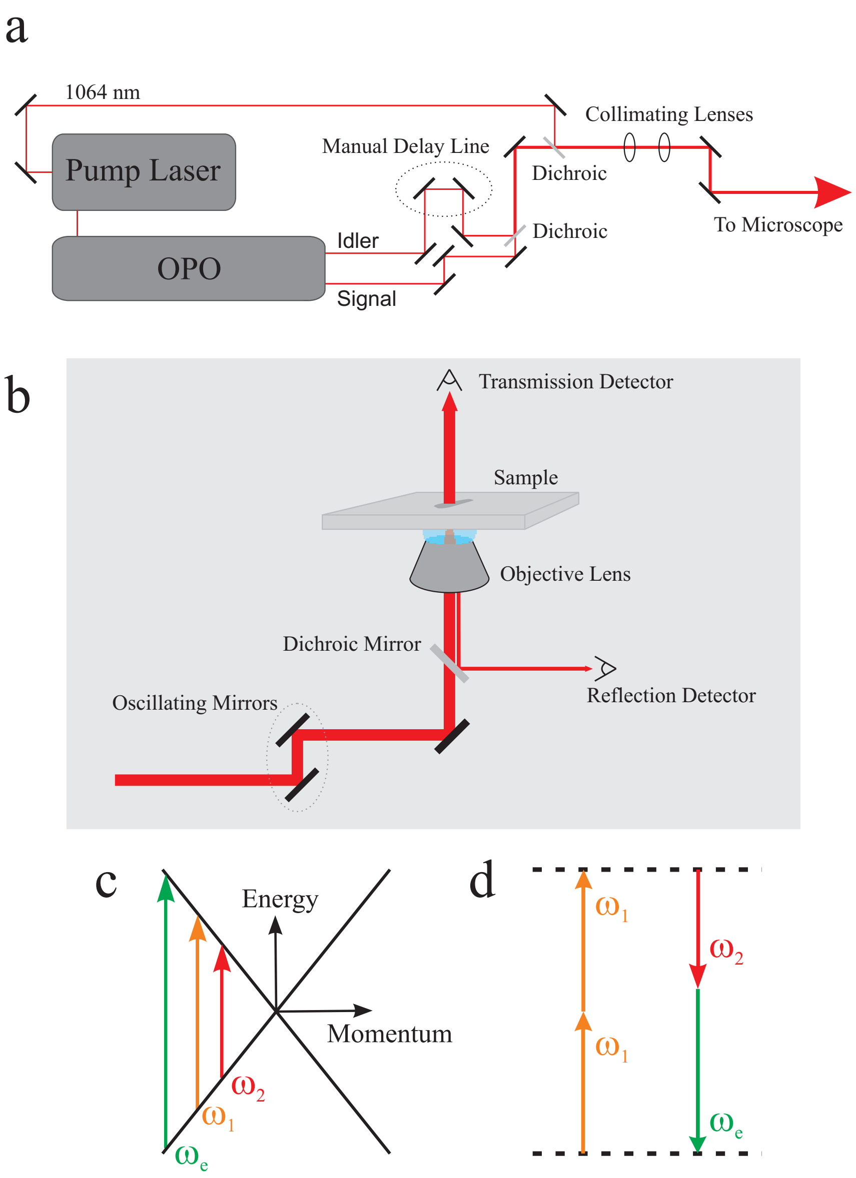

Figure 3.2.1: Schematic of the four–wave mixing experimental setup. (a) Beam paths for the collinearly aligned setup. Measurements may be taken with the use of the signal, idler and 1064 nm beams. (b) Schematic of the microscope where raster scanning is achieved. (c) The low energy electronic band structure of graphene at the K point of the Brillouin zone. Relevent optical transitions are shown and are all resonant. (d) Simple two level model for the four–wave mixing process when measuring $\omega_e = 2\omega_1 - \omega_2$.

3.3 Emission Over Large Wavelength Range

Graphene and few–layer graphene samples are fabricated using the standard method of mechanical exfoliation, described in Section 2.1, and deposited onto a 100 μm thick glass coverslip. Prior to investigation in the nonlinear microscope, the layer thickness is determined via contrast measurements under an optical microscope. The calculated reflection coefficients for a system with N layers, assuming the dielectric constant of each layer to be that of graphite, is shown in Section 1.4.2. Samples of thickness $1 \leq N \leq 6$ are identified, with monolayers and bilayers confirmed via the profile of their 2D Raman peaks.

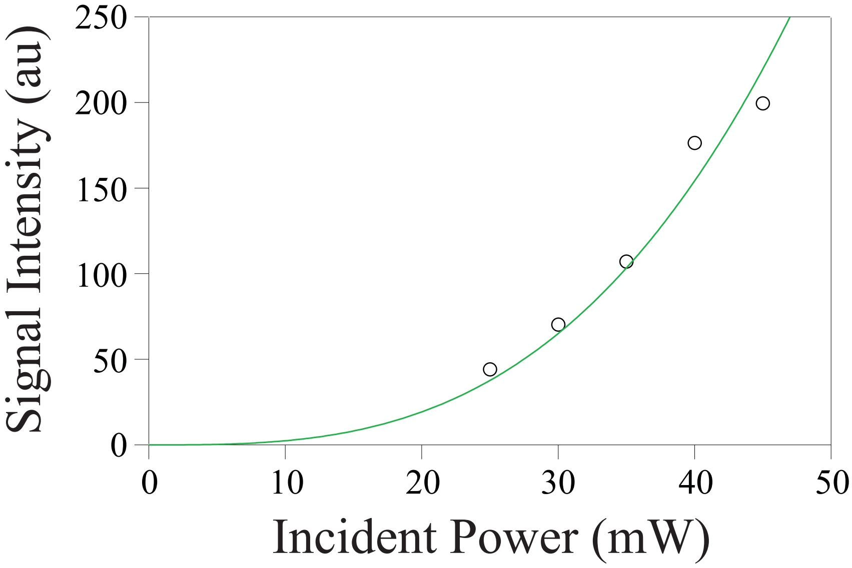

Figure 3.3.1: Nonlinear signal magnitude as a function of incident power for a monolayer sample. The data follows a cubic dependence (solid fit) confirming the third–order nature of the response.

When considering the nonlinear response of a material, one begins with a Taylor expansion of the polarisation, P, which has the form

$$\mathbf{P}(\omega_e) = \epsilon_0 \left[\chi^{(1)}\mathbf{E}(\omega_1) + \chi^{(2)}\mathbf{E}(\omega_1)\cdot\mathbf{E}(\omega_2) + \chi^{(3)}\mathbf{E}(\omega_1)\cdot\mathbf{E}(\omega_2)\cdot\mathbf{E}(\omega_3) + \ldots\right] \tag{3.3.1}$$

where ω_1, ω_2 and ω_3 describe the frequencies of the electric fields, E, of the incident beams, as described in Section 1.4.1. For low electric fields, the polarisation of a material is linear and described by the susceptibility $\chi^{(1)}$. Here, the electric field induces a polarisation in the material which is directly proportional to the driving field. As the driving field is increased, higher order terms may begin to contribute. Nonlinear optics describes systems where the higher order susceptibilities become significant. Since the nonlinear terms are much smaller in magnitude than the typical linear response, for the higher orders to contribute the electric field intensity must increase. One can get an estimate of the required increase by noting the approximate scale of susceptibilities[84],

$$
\begin{aligned}
\chi^{(2)} &\sim \frac{\chi^{(1)}}{E_{\text{at}}} \sim 10^{-8}\,\text{esu} \\
\chi^{(3)} &\sim \frac{\chi^{(1)}}{E_{\text{at}}^{2}} \sim 10^{-15}\,\text{esu}\,,
\end{aligned}
\tag{3.3.2}
$$

where $E_{\text{at}} \sim e/a_{\text{B}}^2$ is the interatomic electric field and a_{B} is the Bohr radius. The applied field is therefore required to be increased by the order of the core electron restoring force. In order to measure higher orders, which quadratically or cubically depend on the incident electric fields, continuous wave excitation is no longer viable. However, pulsed lasers allow for large instantaneous energies at the sample whilst keeping the average power low enough to prevent damage.

For materials which are excited with energies well below their interband transitions, this results in extremely low optical nonlinearities. Normal dielectric materials, such as glasses, are described by $|\chi^{(3)}| \approx 10^{-15}$ esu[84,85]. Strong enhancement of optical nonlinearities can arise when the mixing or emission frequencies (ω_1, ω_2 or ω_e) match the energy difference between electronic levels[82]. It is therefore interesting to study the magnitude and frequency dependence of the nonlinear response of graphene, a gapless semiconductor with a linear dispersion relation, since electronic transitions in this material match all optical energies simultaneously, Figure 3.2.1(c).

Samples are measured using degenerate four–wave mixing, Section 2.2.2. When overlapped in time, the incident signal and idler pulses mix within the sample to generate a third coherent pulse. The nonlinear nature of the graphene signal is confirmed in several ways. Firstly, the enhanced signal is extremely sensitive to the temporal overlap of the incident pulses. By varying the overlap of the beams, with the use of a manual delay line, Figure 3.2.1(a), the increased signal can only be observed at temporal overlap. Secondly, by varying the intensity of the pump pulses, one observes the amplitude of the emission peak to follow a cubic dependence, Figure 3.3.1, which confirms the third–order nature of the process. Thirdly, and most significantly, the third–order signal is confirmed with the use of a spectrometer. The absolute value of the emission wavelength can be calculated and the spectrum, shown in Figure 3.3.2, shows complete agreement. Here, incident beams of wavelength 945 nm and 1217 nm are mixed and for the condition $\omega_{\text{e}} = 2\omega_1 - \omega_2$ one predicts a nonlinear emission at 772 nm, precisely as observed. The grey area denoted in Figure 3.3.2 shows the ~ 200 nm bandpass filter used to exclude the pump beams. A background signal can be observed due to white light generation from both the 945 nm and 1217 nm beams. By plotting the data out to 950 nm one is able to observe the peak from the 945 nm pump. This is included to illustrate that although the nonlinear response is strong (the large spike at 772 nm) it is still orders of magnitude below the reflection of the incident beams (since outside the filter region the extinction coefficient is of the order

10^5).

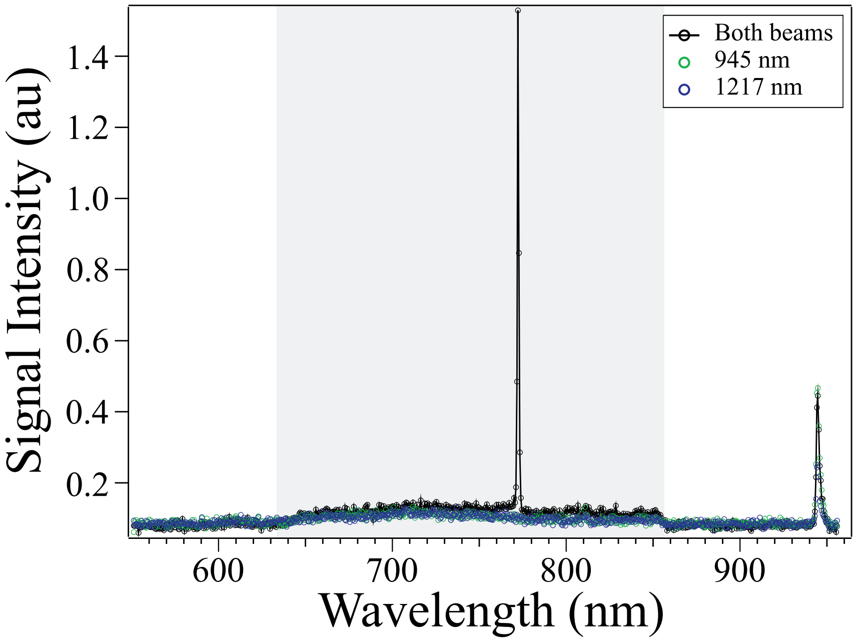

Figure 3.3.2: Spectrometer signal, measured as a function of emission wavelength, for a graphene sample illuminated with 945 nm and 1217 nm picosecond pulses. The 750 nm bandpass filter is highlighted by the grey shaded region. One can clearly observe the emission from the sample at 772 nm, corresponding to the condition $\omega_e = 2\omega_1 - \omega_2$. The peak at 945 nm is the pump beam leaking through the filters.

Centro–symmetric materials, such as isolated sheets of graphene, do not possess second–order optical nonlinearities within the dipole approximation. From Equation 3.3.1, the second order polarisation, $\mathbf{P}^{(2)}$, is expressed as

$$\mathbf{P}^{(2)}(\omega_e) \; = \; \chi^{(2)} \cdot \mathbf{E}(\omega_1) \cdot \mathbf{E}(\omega_2)\,. \tag{3.3.3}$$

By reversing the direction of the applied fields, due to the symmetry of the sample the polarisation is also reversed,

$$-\,\mathbf{P}^{(2)}(\omega_{\mathrm{e}}) \; = \; \chi^{(2)} \cdot -\mathbf{E}(\omega_1) \cdot -\mathbf{E}(\omega_2)\,. \tag{3.3.4}$$

For Equations 3.3.3 and 3.3.4 to be equated, the condition $\chi^{(2)} = 0$ must be met.

Similarly to Equation 3.3.3, the third–order polarisability of a material is described by

$$\mathbf{P}^{(3)}(\omega_{\mathrm{e}}) \; = \; \chi^{(3)}\mathbf{E}(\omega_1) \cdot \mathbf{E}(\omega_2) \cdot \mathbf{E}(\omega_3)\,. \tag{3.3.5}$$

In the degenerate four–wave mixing process used in these experiments, two of the mixing frequencies are equal: $\omega_1 = \omega_3$. Due to energy conservation, the frequency of emitted light is $\omega_e = 2\omega_1 - \omega_2$, Figure 3.2.1(d). For bulk materials, the degree of optical nonlinearity is characterised by the magnitude of the third–order susceptibility, $\chi^{(3)}$.

Due to the gapless, linear dispersion relation in graphene, to a first approximation the choice of incident wavelengths is somewhat arbitrary considering that each optical transition is resonant. One is only restricted by the output wavelengths of the OPO and the choice of optical filters.

Figure 3.3.3 shows the measured nonlinear signal from a monolayer flake as a function of emission wavelength, λ_e, for several combinations of pump wavelengths, λ_1 and λ_2. In all measurements one observes a clear spike in emission at the wavelength corresponding to the condition $\omega_\mathrm{e} = 2\omega_1 - \omega_2$.

The wavelength range used is limited at short emission wavelengths by the restriction that $\omega_1 - \omega_2$ must be smaller than the frequency of the 2D Raman peak in graphene in order to avoid coherent anti–Stokes Raman scattering. When $\omega_1 - \omega_2$ corresponds to an optically active phonon frequency, one can observe coherent anti–Stokes Raman scattering. Since this work focuses on the electronic enhancement of $\chi^{(3)}$, excitation of optical phonons is avoided. This limits the signal and idler wavelengths to 931 nm and 1241 nm, as $\omega_1 - \omega_2 = 2685$ cm^{-1}, resulting in the shortest available emission of 745 nm. On the long wavelength side, the emission range is limited by the filters used in the experimental set up. Both the dichroic mirror within the microscope and the band–pass filter in front of the detector have cut–off wavelengths of 850 nm. The constraints on the signal and idler are therefore 980 nm and 1164 nm, corresponding to an emission wavelength of 846 nm and a coherent anti–Stokes Raman shift of 1611 cm^{-1}. The zone–centre optical phonon at $\sim$ 1580 cm^{-1} is therefore also avoided.

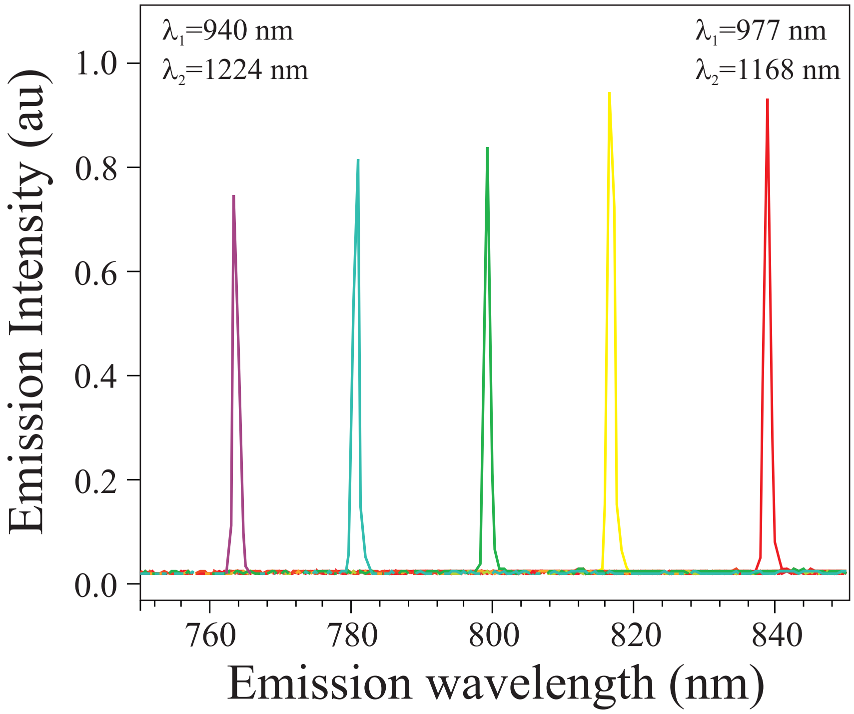

Figure 3.3.3: Emission spectra for a graphene flake with pump pulses of varying wavelengths, (λ_1, λ_2): (940 nm, 1224 nm), (950 nm, 1210 nm), (958 nm, 1196 nm), (967 nm, 1183 nm) and (977 nm, 1168 nm). The corresponding emission wavelengths are therefore 763 nm, 782 nm, 799 nm, 818 nm and 840 nm.

By varying the pump wavelengths, one is able to investigate the magnitude of the nonlinear emission over a large wavelength range. One can clearly see that, for equivalent pump intensities, the amplitude of the emission only changes by $\sim$ 10% over the range of incident wavelengths. This is in stark contrast to the emission from other materials, such as carbon nanotubes[80] or coupled quantum wells[86], where the emission intensity varies strongly with wavelength due to resonant excitation of band gaps or discrete energy levels.

3.4 Calculating the Magnitude of $\chi^{(3)}$ in Graphene

In this section, the magnitude of the nonlinear response from graphene and few–layer graphene is estimated from both experiment and theory. Experimentally, the emission from graphene is compared to that of a well characterised system, a gold film, which is used to calibrate the signal magnitude. Theoretically, the quantum kinetic equation is solved for graphene, a calculation performed by Dr. S. A. Mikhailov and briefly summarised here for completeness[5].

For bulk materials, the third–order nonlinearity is characterised by the third–order susceptibility $\chi^{(3)}$, which relates the polarisation per unit volume P to the third power of the electric field E. In a two–dimensional conducting material, like graphene, it is more appropriate to describe the nonlinear response in terms of the sheet current, $j^{(3)}$, and the third–order surface dynamical conductivity, $\sigma^{(3)}$,

$$j^{(3)}(\omega_{\mathrm{e}}) \;=\; \sigma^{(3)} E_1(\omega_1) E_2(\omega_2) E_3(\omega_3)\,. \tag{3.4.1}$$

To calculate this, one first begins by considering a uniform electric field incident onto a graphene sheet,

$$\mathbf{E}(t) \;=\; \mathbf{E}_1 \cos(\omega_1 t) \;+\; \mathbf{E}_2 \cos(\omega_2 t)\,. \tag{3.4.2}$$

For the degenerate measurements performed here, two of the mixing frequencies are equal, i.e. $\omega_1 = \omega_3$. The quantum kinetic equation,

$$(i\hbar)\,\frac{\partial \hat{\rho}}{\partial t} \;=\; \left[\hat{H}, \hat{\rho}\right]\,, \tag{3.4.3}$$

is solved using the Hamiltonian which describes the interaction of electrons in graphene with electric fields of frequency ω_1 and ω_2,

$$\hat{H} \;=\; \hat{H}_0 \;+\; ex\left[E_1 \cos(\omega_1 t) \;+\; E_2 \cos(\omega_2 t)\right]\,. \tag{3.4.4}$$

Here, $\hat{H}_0$ is the tight binding Hamiltonian of graphene (Equation 1.2.10), $\hat{\rho}$ is the density matrix and x is the coordinate in the direction of the electric field.

The incident field amplitudes $E_{1,2}$, induce a third–order electric current, $j_{\mathrm{e}}^{(3)}$, with several frequency harmonics, ω_1, ω_2, $3\omega_1$, $3\omega_2$, $2\omega_1 \pm \omega_2$ and $2\omega_2 \pm \omega_1$. For the experiments presented, the third–order electric current component of relevance has the form

$$j_{\mathrm{e}}^{(3)} \;=\; j_{\mathrm{e}} cos\left((2\omega_1 - \omega_2)t\right)\,. \tag{3.4.5}$$

This result is obtained with several conditions, firstly $\hbar\omega_{1,2} \;\gg\; \mu$, where μ is the chemical potential, which is true for the high frequency, optical pulses utilised. Secondly, $\omega_{1,2}\tau \;\gg\; 1$, where τ is the relaxation time which, again, is satisfied for the high frequency optical pulses, such that scattering of electrons is not included.

For these conditions, the emission at $\omega_{\mathrm{e}} \;=\; 2\omega_1 - \omega_2$ is calculated as[5]

$$j_{\mathrm{e}} \;=\; \frac{3}{32}\frac{e^2}{\hbar} E_2 \left(\frac{eVE_1}{\hbar\omega_1\omega_2}\right)^2 \xi(\omega_1, \omega_2), \tag{3.4.6}$$

where, apart from $\xi(\omega_1, \omega_2)$, which is a function weakly dependent on frequency,

$$\xi(\omega_1, \omega_2) \;=\; \frac{\omega_2^2 - 2\omega_1\omega_2 - 2\omega_1^2}{\omega_1\left(2\omega_1 - \omega_2\right)}\,, \tag{3.4.7}$$

the induced current is dependent on three terms, the linear conductivity, $\sim\ e^2/\hbar$, the electric field, E, and the nonlinear electric field parameter, $eVE/\hbar\omega_1\omega_2$. This parameter is the work done by the electric field in one oscillation period, $\sim\ eVE/\omega$, divided by the quantum energy $\hbar\omega$. Notice here that the nonlinear response falls as $\sim\ \omega^{-4}$.

Equation 3.4.6 can then be used to estimate the magnitude of the nonlinear response from graphene. Since $\omega_1\ \approx\ \omega_2$, the nonlinear conductivity may be approximated as

$$\sigma^{(3)}\ \sim\ \frac{e^2}{\hbar}\left(\frac{eV}{\hbar\omega^2}\right)^2\ . \tag{3.4.8}$$

An effective third–order susceptibility, $\chi^{(3)}_{\text{gr}}$, is introduced, which is related to the conductivity as,

$$\chi^{(3)}_{\text{gr}}\ \simeq\ \frac{\sigma^{(3)}}{\omega d_{\text{gr}}}\ , \tag{3.4.9}$$

where d_{gr} is taken to be the thickness of the graphene layer, approximately 3 Å. The third–order susceptibility of an insulator is typically $\left|\chi^{(3)}_{\text{ins}}\right|\ \approx\ a_{\text{B}}^2/e^2\ \approx\ 10^{-15}$ esu[84]. Taking the third–order susceptibility of graphene from Equation 3.4.9 and substituting in Equation 3.4.8, the signal magnitude can be normalised to that of an insulator,

$$\begin{aligned}\frac{\left|\chi^{(3)}_{\text{gr}}\right|}{\left|\chi^{(3)}_{\text{ins}}\right|}\ &\simeq\ \frac{\sigma^{(3)}\text{gr}}{\omega d_{\text{gr}}}\frac{e^2}{a_{\text{B}}^4}\\ &\simeq\ \left(\frac{e^2}{\hbar c}\right)^3\frac{v^2}{c^2}\frac{\lambda^5}{a_{\text{B}}^4 d_{\text{gr}}}\ .\end{aligned} \tag{3.4.10}$$

If one assumes $\lambda\sim 1\ \mu$m, $a_{\text{B}}\simeq d_{\text{gr}}$, $e^2/\hbar c = 1/137$ and $v/c\simeq 1/300$,

$$\begin{aligned}\left|\chi^{(3)}_{\text{gr}}\right|\ &\simeq\ \left|\chi^{(3)}_{\text{ins}}\right|\ \times\ 10^8\\ &\simeq\ 10^{-7}\,\text{esu}.\end{aligned} \tag{3.4.11}$$

This predicted value is extremely large and may be utilised for high–contrast imaging. In order to perform electrical measurements graphene must first be deposited onto a non-conducting, dielectric substrate. With a predicted nonlinear response several orders of magnitude greater than that of a typical dielectrics, visualising graphene via nonlinear imaging is predicted to be orders of magnitude better than for standard reflection.

To quantify the magnitude of the observed nonlinear response in graphene experimentally, the monolayer signal is compared with a well characterised, quasi 2D material: a thin film of gold evaporated onto a glass microscope coverslip[87,88]. It is known that a strong nonlinear response of thin gold films arises from the excitation of localised plasmons[87,88]. In Figure 3.4.1, the comparison between the nonlinear emission of a 4 nm thick gold film with that of a monolayer graphene flake is shown. One can see that the nonlinear emission from the gold film is very different from that in graphene. For graphene, one observes a large peak at the emission wavelength, while in gold one can see a significantly smaller peak on top of a smooth background, caused by two–photon luminescence[89]. To compare the magnitudes of the third–order susceptibilities, one has to compare the magnitude of the graphene peak, I_{gr} with that of the gold peak, I_{Au}, with respect to the background. For the results presented in Figure 3.4.1, the ratio of the peak intensities in the two materials is approximately ten. From this, the nonlinear susceptibility of graphene, $\chi^{(3)}_{\text{gr}}$, can be found from that of the gold film $\left(|\chi^{(3)}_{\text{Au}}| \sim 10^{-9} - 10^{-8}\ \text{esu}\right)$[87,88] using the relation[81,87]

$$\frac{|\chi^{(3)}_{\text{gr}}|}{|\chi^{(3)}_{\text{Au}}|} \approx \frac{L_{\text{gr}}}{L_{\text{Au}}}\sqrt{\frac{I_{\text{gr}}}{I_{\text{Au}}}}, \tag{3.4.12}$$

where L_{gr} and L_{Au} are the thicknesses of the graphene system and the gold film, respectively, and I is the measured intensity of the four–wave signal. Given that $L_{\text{Au}} \sim 10 \times L_{\text{gr}}$, one can estimate that for a single layer of graphene $|\chi^{(3)}_{\text{gr}}| \approx 10^{-7}$ esu, in good agreement with the theoretical prediction.

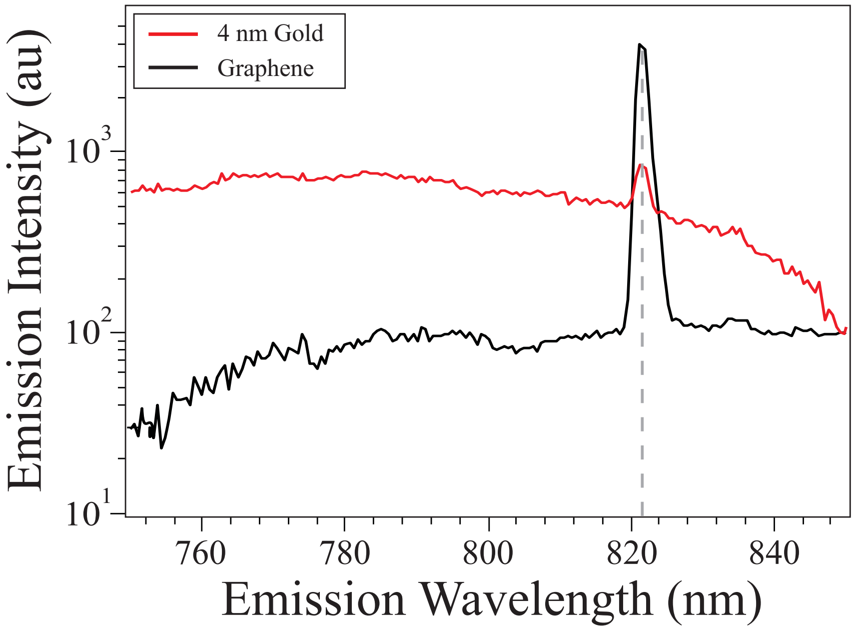

Figure 3.4.1: Nonlinear signal intensity, as a function of emission wavelength, for a graphene sample and a thin (4 nm) evaporated film of gold, measured under the same experimental conditions. The samples are illuminated with 969 nm and 1179 nm, producing a nonlinear emission at 823 nm. The gold film shows a peak at the expected emission wavelength on top of a broad luminescence background. The graphene sample shows an order of magnitude increase in signal intensity, with a smaller luminescence background.

While this estimate of the nonlinear susceptibility of graphene is comparable in magnitude to those measured for nanotubes, it is demonstrated that the response is relatively constant with wavelength, Figure 3.3.3. This frequency independence in the nonlinear response could be useful in graphene applications where a constant response is important, for example, in such nonlinear devices as bistable mirrors for mode–locking, optical limiters and switchable elements.

It is interesting to compare the nonlinear optical properties of graphene to those of other carbon materials, such as carbon nanotubes, which have raised considerable interest in recent years[78–82,90,91]. Carbon nanotubes can be purely metallic or possess a finite band gap, depending on the manner in which the edges of the graphene layer join to form the tube. Since nonlinear properties are known to be very dependent on the nature of electronic transitions[82], carbon nanotubes exhibit a broad range of nonlinear polarisabilities in the optical and near–infrared range. For thin films of nanotubes, $|\chi^{(3)}| \sim 10^{-6} - 10^{-8}$ esu has been reported using a variety of experimental techniques[78–81]. In particular, four–wave mixing measurements, similar to those carried out here, gave $|\chi^{(3)}| \sim 10^{-8}$ esu[81] for nanotube films. Due to the singularity in the electron density of states at the band edges of nanotubes (Van Hove singularity)[82,90,91], theoretical predictions suggest that homogenous ensembles of identical tubes will exhibit $|\chi^{(3)}|$ which varies over six orders of magnitude on varying excitation wavelengths[82]. This strongly resonant nature has a typical resonance width < 1 nm[82].

3.5 Graphene and Few–Layer Graphene on Dielectric Substrates

Investigating the magnitude of the nonlinear response in few–layer graphene, Figure 3.5.1, one observes a linear relationship between the nonlinear contrast and the number of graphene layers. Here, a range of exfoliated flakes are measured and the optical contrast, Equation 1.4.10, is used to calculate the number of layers. The linear relation demonstrates how the induced polarisation in each of the few–layer samples is constructively summed. Due to the huge response observed in graphene and the weak nonlinearity for dielectrics, the contrast observed is approximately seven orders of magnitude greater than for standard optical reflection microscopy[30,31,92].

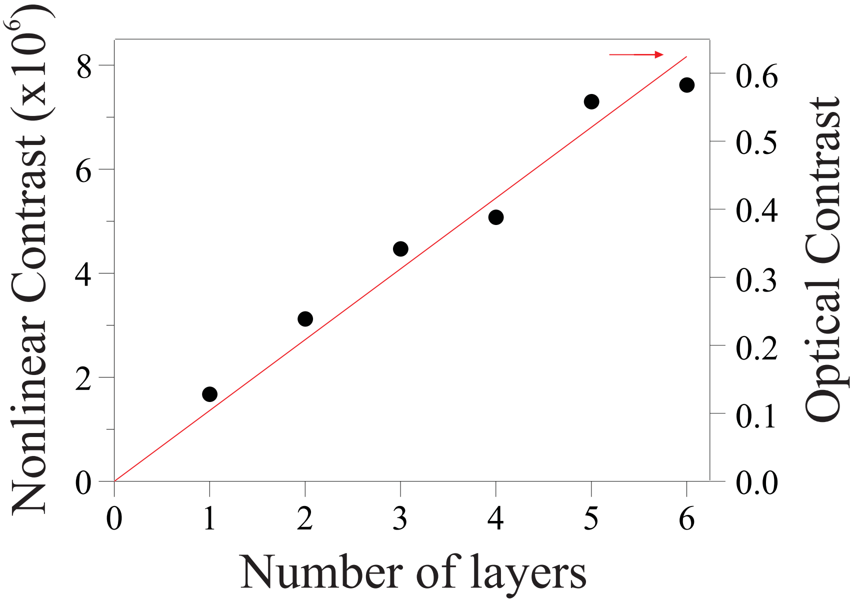

Figure 3.5.1: Nonlinear contrast, as a function of layer number, for graphene and few–layer graphene on a glass substrate. For comparison, the right hand axis shows the reflection contrast for white light illumination, with an increase in contrast of the order 10^7 observed. The layer number is found from the optical contrast and displayed along side a linear fit.

The striking images produced from this nonlinear technique are demonstrated in Figure 3.5.2, where a comparison is made between optical reflection and four–wave mixing. The folded monolayer and large trilayer are imaged with a 100× objective lens and a 550 nm band–pass filter. Comparing the same flakes in the nonlinear microscope (emission at 772 nm), shows the enormous contrast enhancement. Taking a profile across the folded monolayer (dashed white line) illustrates the clarity with which the flakes are imaged with. As the dielectric substrate does not show any measurable nonlinear signal, this contrast is very large: for a monolayer $C = 1.7 \times 10^6$ compared to $C = 0.08$ for standard optical reflection microscopy[92]. (Similar enhanced imaging of carbon nanotubes using nonlinear optics has been recently observed by Kim *et. al*[93]). It should be noted that the nonlinear image contrast is limited only by the noise of the detector, since the nonlinear signal from the glass substrate is negligibly small. One expects similarly high contrast for graphene on most dielectric substrates, since these materials have very weak optical nonlinearities[85]. This makes the method of visualising graphene flakes using nonlinear optical response rather universal.

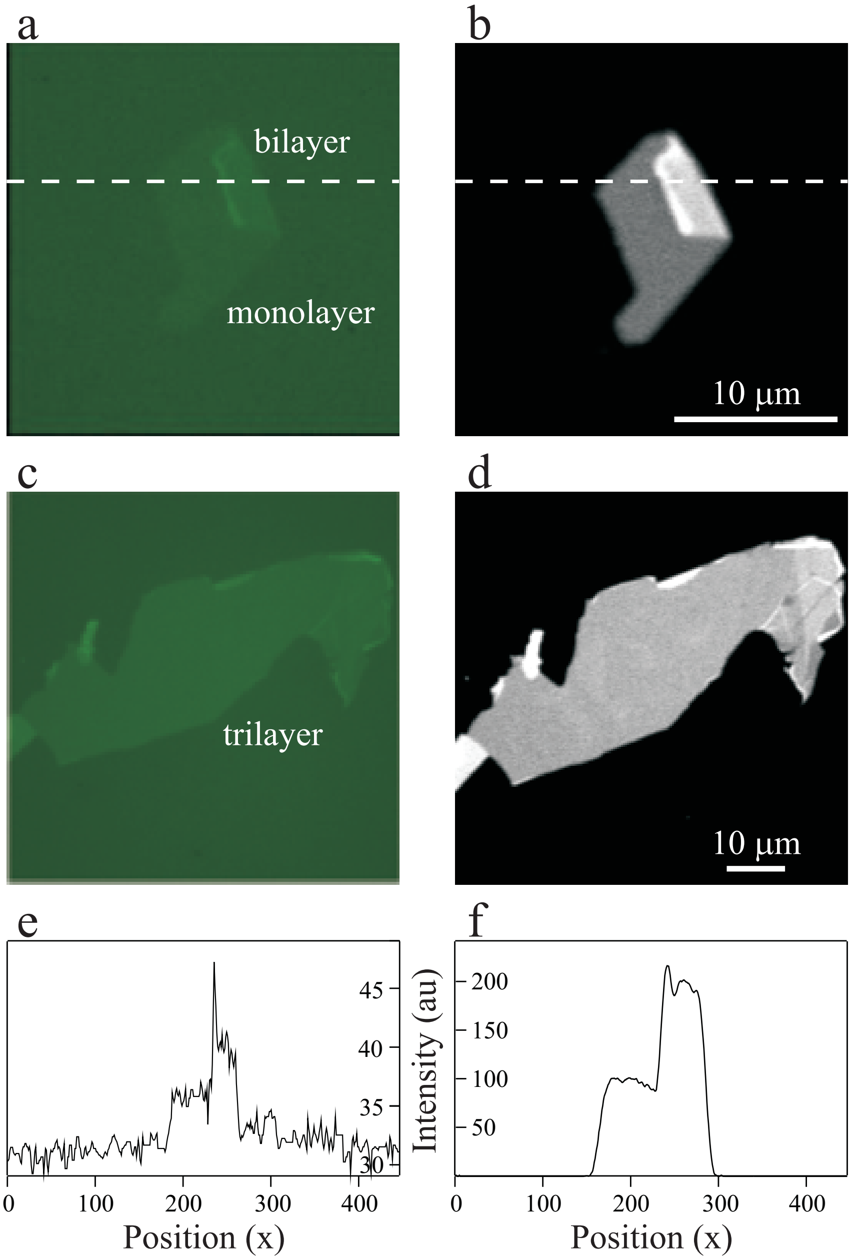

Figure 3.5.2: Reflection and nonlinear images of monolayer, bilayer and trilayer graphene. (a) A reflection image of a folded monolayer flake taken with a 550 nm band–pass filter. (b) The same flake imaged with four–wave mixing. The pump (945 nm) and probe (1217 nm) pulses generate signal at 772 nm. (c) Optical image of a trilayer flake taken with a 550 nm band–pass filter. (d) Four–wave mixing image of the trilayer, emission at 772 nm. (e,f) Profiles of the folded monolayer taken along the dashed white line.

Imaging thicker flakes reveals an interesting phenomenon as the nonlinear contrast falls to zero for much thicker samples. By considering the nonlinear response of an N–layered system[5], the signal intensity as a function of layer thickness is estimated. First, the reflection, transmission and absorption coefficients are calculated. One assumes that the thickness of the N–layered system is smaller than the wavelength of the incident light, such that the induced oscillating current in each layer is coherent and can be summed over all the layers. The resulting coefficients are shown in Figure 3.5.3(a).

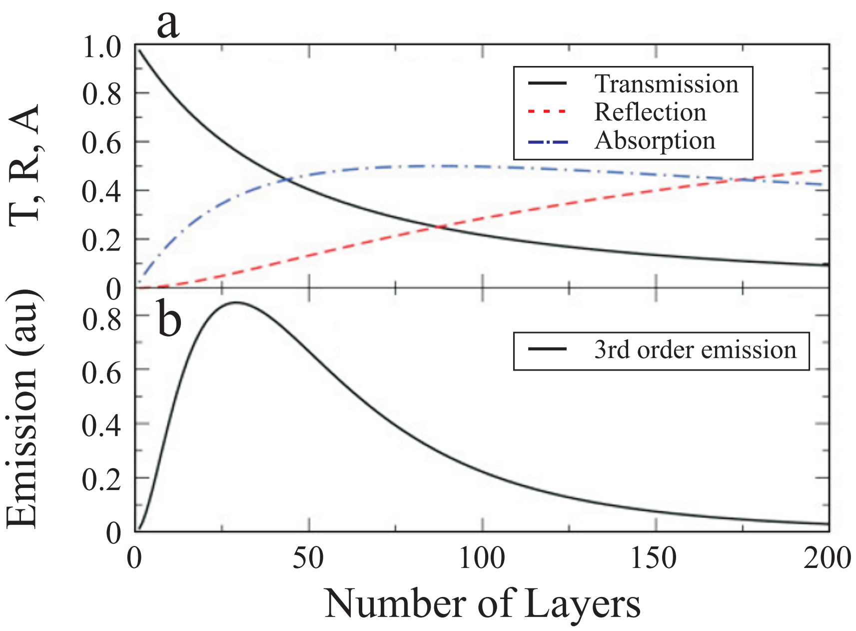

Figure 3.5.3: (a) Transmission, reflection and absorption as a function of the number of graphene layers, plotted for optical frequencies. (b) Estimated nonlinear emission as a function of the number of graphene layers. The theoretical peak signal is found at approximately 30 layers. Image adapted from[5].

The intensity of the nonlinearly emitted frequency, $I^{(3)}_{\omega_e}$, for the N–layered system is calculated as[5]

$$I^{(3)}_{\omega_e} = \frac{4^3\pi^4[\sigma^{(3)}]^2}{c^4} I_1^2 I_2 \frac{N^2}{\left(1+\frac{N\pi\alpha}{2}\right)^8}, \tag{3.5.1}$$

plotted in Figure 3.5.3(b), which predicts a peak response for $N \approx 30$ layers. As the number of layers is increased beyond this number, the polarisability of the material is suppressed due to the increase in the magnitude of the reflected field. This results in a decrease in the generated nonlinear signal. To confirm this trend, a larger thickness range of exfoliated flakes are investigated. The layer number is estimated via optical contrast which, for $N \gtrsim 10$ quickly becomes inaccurate due to the difficulty in distinguishing thicker layers. Figure 3.5.4 plots the nonlinear contrast as a function of the estimated layer thickness. The trend of increasing signal up to $N \sim 20$ is observed, along with a subsequent reduction in signal for thicker layers.

Whilst the quantum kinetic approach gives a good order of magnitude estimate for the nonlinear response in graphene, to fully quantify the predicted response a more detailed approach is required. By including carrier relaxation and quantum decoherence timescales, Zhang *et. al*[94] have shown excellent agreement with the experimental data. By varying the pump wavelengths and decay rates it can be shown that the nonlinear response in graphene may vary between $10^{-10} - 10^{-6}$ esu. With the relaxation and decoherence timescales specific to individual flakes, the absolute value of the response will be sample dependent. Estimating the layer thickness via optical contrast introduces large errors for thicker flakes and will contribute to the discrepancy in the peak response, shown in Figure 3.5.4.

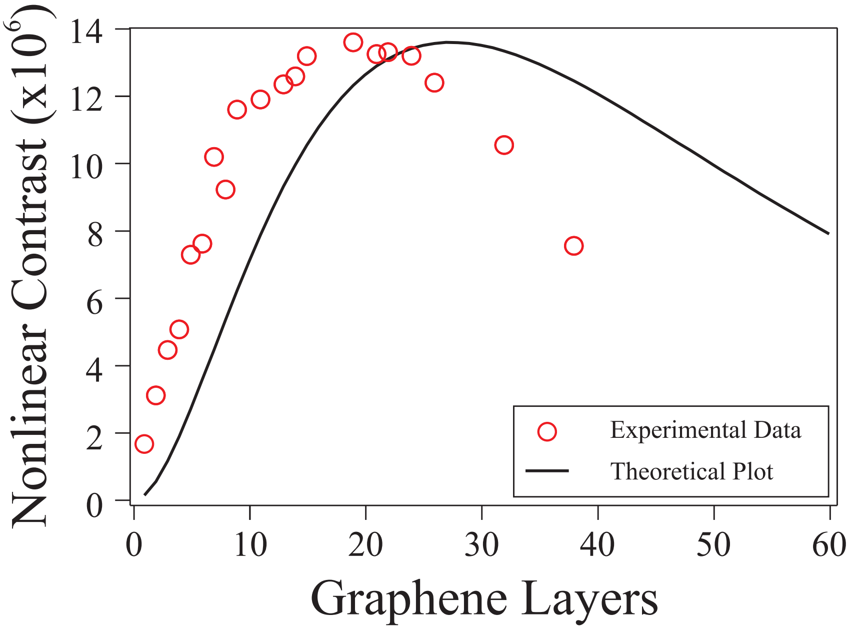

Figure 3.5.4: Nonlinear contrast as a function of the number of graphene. The theoretical curve[5] (shown in Figure 3.5.3(b), with no fitting parameters) agrees qualitatively with the increase in response for thinner layers, the peak at approximately 25 layers and the subsequent decrease for thicker layers. The theoretical curve is scaled to the measured nonlinear peak contrast and the number of layers are estimated from white light reflection contrast.

3.6 Summary

In summary, it is shown that graphene exhibits almost wavelength–independent, strongly nonlinear optical properties in the near–infrared spectral region, described by a third–order susceptibility $|\chi^{(3)}| \sim 10^{-7}$ esu.

It is demonstrated that nonlinear optical measurements are a useful tool for visualising graphene flakes on dielectric substrates. Studies of nonlinear properties of graphene represent a promising direction for optical experiments on this new material. It would be interesting to extend these studies to a broad range of frequencies, including the low–energy (THz) range. Experimental studies of nonlinear optical properties of graphene should be carried out in conjunction with theoretical investigations, which are currently rather limited[77,94–96].

Investigating the magnitude of the nonlinear response as a function of layer number shows a linear increase in flake contrast for few–layer samples, making this technique useful for quantifying layer thickness. Due to the increase in the reflection coefficient in thicker samples, the nonlinear contrast falls to zero for $N \gtrsim 100$ layers and is in good agreement with the theoretical prediction.

Chapter 4

Imaging Epitaxial Graphene on Silicon Carbide

4.1 Introduction

The global interest in graphene research stems not only from the fundamental physics that can be investigated, but also the potential to use graphene in devices. Engineering a band gap in graphene, either by modifying the graphene with adatoms[42,97,98], strain engineering[99,100] or fabricating nanoribbons[101,102], has the potential to enable the industry to challenge silicon as the front–runner for electronics. One major hurdle to overcome is the fabrication of large area, high quality samples. Currently, research is focussed into two main areas, epitaxially grown graphene on silicon carbide and growth via metal substrates, these techniques are discussed in Section 2.1.2.

In this chapter, four–wave mixing is employed to investigate the surface of epitaxially grown graphene on the silicon– and carbon–terminated faces of SiC. Due to the presence of nonlinear signal arising from the bulk, a method of luminescence imaging is presented. By varying the input signal (and therefore idler) wavelength, the third–order nonlinear emission can be tuned to outside the optical band–pass filter. Only second order luminescence signal is therefore measured, which is shown to be sensitive to the interface carbon only. The differences in the measured signal from the carbon– and silicon–terminated faces is investigated via Raman spectroscopy.

4.2 Z–Scan profiles

Similar to the experiments performed in Chapter 3, third–order nonlinear imaging is achieved utilising the four–wave mixing technique, Section 2.2.2. Silicon carbide samples are provided by C. Marrows, G. Creeth and A. Strudwick at the University of Leeds, with one or two layers of carbon grown on the carbon–terminated face of 4–H SiC.

With exfoliated flakes deposited on glass substrates the background nonlinear response is negligibly small. Imaging large area epitaxial graphene on silicon carbide produces a large nonlinear response from within the bulk; a feature which should be removed for surface imaging. The nonlinear signal is generated where the signal and idler beams are temporally and spatially overlapped. With the high numerical aperture lens used the spatial resolution is of the order 1 μm, however, the focal volume extends of the same order into the substrate. Mixing of the incidents beams to generate nonlinear signal therefore occurs over a $z \sim 1$ nm for the carbon surface but over $z \sim 1$ μm for the bulk.

Surface imaging is achieved by removing all third order signal and measuring instead the luminescence produced from both the carbon interface and the bulk. A typical image of the carbon–terminated face of SiC is illustrated in Figure 4.2.1. The image is taken to include the edge of the sample.

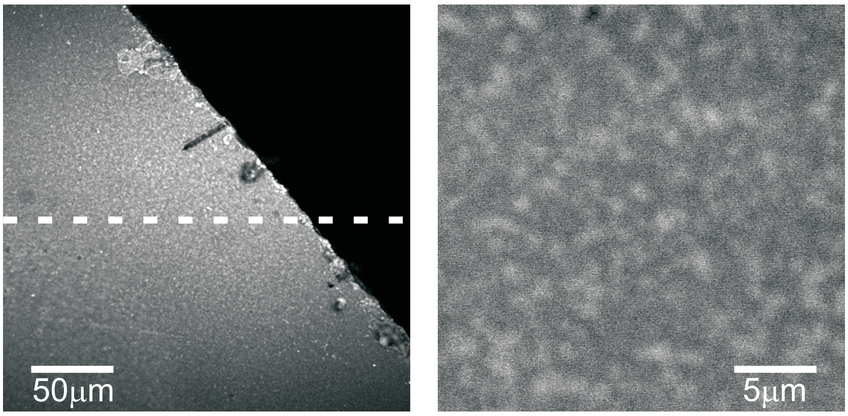

Figure 4.2.1: Typical four-wave mixing images of the carbon face of epitaxial SiC for low (left) and high (right) magnification. Dashed line denotes the position of the XZ slice in Figure 4.2.2. Imaging is achieved with an emission wavelength of 780 nm.

By varying the focal position it is possible to investigate the signal intensity as a function of depth. To achieve this, a depth scan is taken along the dashed line in Figure 4.2.1. The focus is optimised at the interface and then scanned from +15 μm (within the SiC) to -15 μm (below the interface). The signal intensity as a function of focal position can then be investigated.

A signal wavelength of 926 nm, coupled with an idler wavelength of 1250 nm, produces a third–order nonlinear emission at 735 nm. The nonlinear signal is collected through a 750 nm centre wavelength, 210 nm FWHM band–pass filter, and focussed onto a PMT. Scanning of the focal position through the sample is shown in Figure 4.2.2. Below the interface there is no signal collected, as one would expect. Pushing the focus into the bulk returns a large nonlinear response, comparable to that of the interface carbon signal.

By elongating the signal wavelength the magnitude of the bulk signal is observed to decrease. Once a signal wavelength of 990 nm is used the emission from the bulk becomes negligible and a sharp, high contrast feature is observed at the interface.

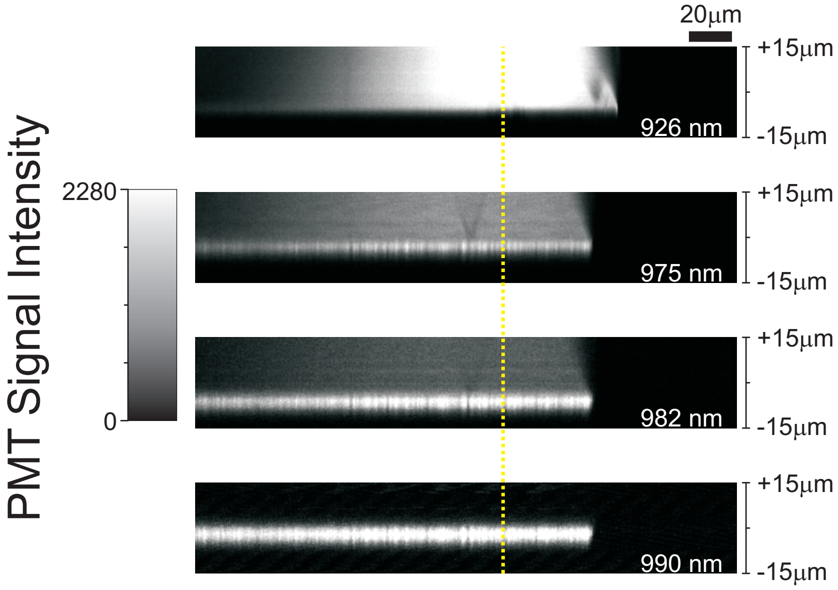

Figure 4.2.2: Z–scan images at varying pump (and therefore probe and emission) wavelengths. Images are obtained by measuring along the dashed line in Figure 4.2.1(a) The focal position is varied from within the bulk of the silicon carbide to below the interface. Lowering the pump energy is shown to remove all bulk signal, returning signal purely from the interface. The various pump wavelengths are indicated with all images scaled to the same PMT intensity range.

The reduction in the bulk signal arises from the removal of all third–order nonlinear signal. With incident signal and idler wavelengths of 990 nm and 1150 nm respectively, the third–order emission peak is found at 870 nm, outside the band–pass region of the optical filter. Since the filter is relatively broad (210 nm FWHM), luminescence signal is transmitted. This signal is usually dominated by the nonlinear contribution. A limited number of studies involving luminescence in graphene have been undertaken in recent years[103–107] with a demonstration that luminescence can be used to provide high–contrast imaging[105].

Taking a slice through the data in Figure 4.2.2 (yellow dashed line) the interface signal is plotted as a function of pump wavelength, Figure 4.2.3. The graphitised interface is first compared to the interface of a dummy silicon carbide sample with an emission wavelength of 858 nm. For two different line scans, 70 μm and 140 μm in from the sample edge, the graphitised sample shows a large luminescence peak which is not present in the dummy sample. The luminescence is therefore confirmed as carbon signal.

Focussing now on the wavelength dependence of the interface and bulk signal, Figure 4.2.3(b,c) plots the signal intensity, as a function of focal position, for a range of input signal wavelengths in both reflection and transmission. For a pump wavelength of 926 nm the idler and emission wavelengths are 1250 nm and 735 nm respectively. The nonlinear signal from the carbon and the bulk therefore pass through onto the PMT and a large signal is measured as the focal point is stepped into the bulk. Elongating the signal wavelength produces a lower energy emission photon. Once the signal wavelength approaches 980 nm (emission at 846 nm) a considerable reduction in the bulk signal is observed. Pushing the emission past the edge of the optical filters completely removes the bulk contribution.

The increased noise observed in transmission is due to the passage of the beams through the bulk substrate. Note that the peak signal does not appear at zero distance from focus. This error is introduced by beginning the measurements at the focal position found manually with a white light source. A small difference in the focal position between the eyepiece and the PMT accounts for this systematic error.

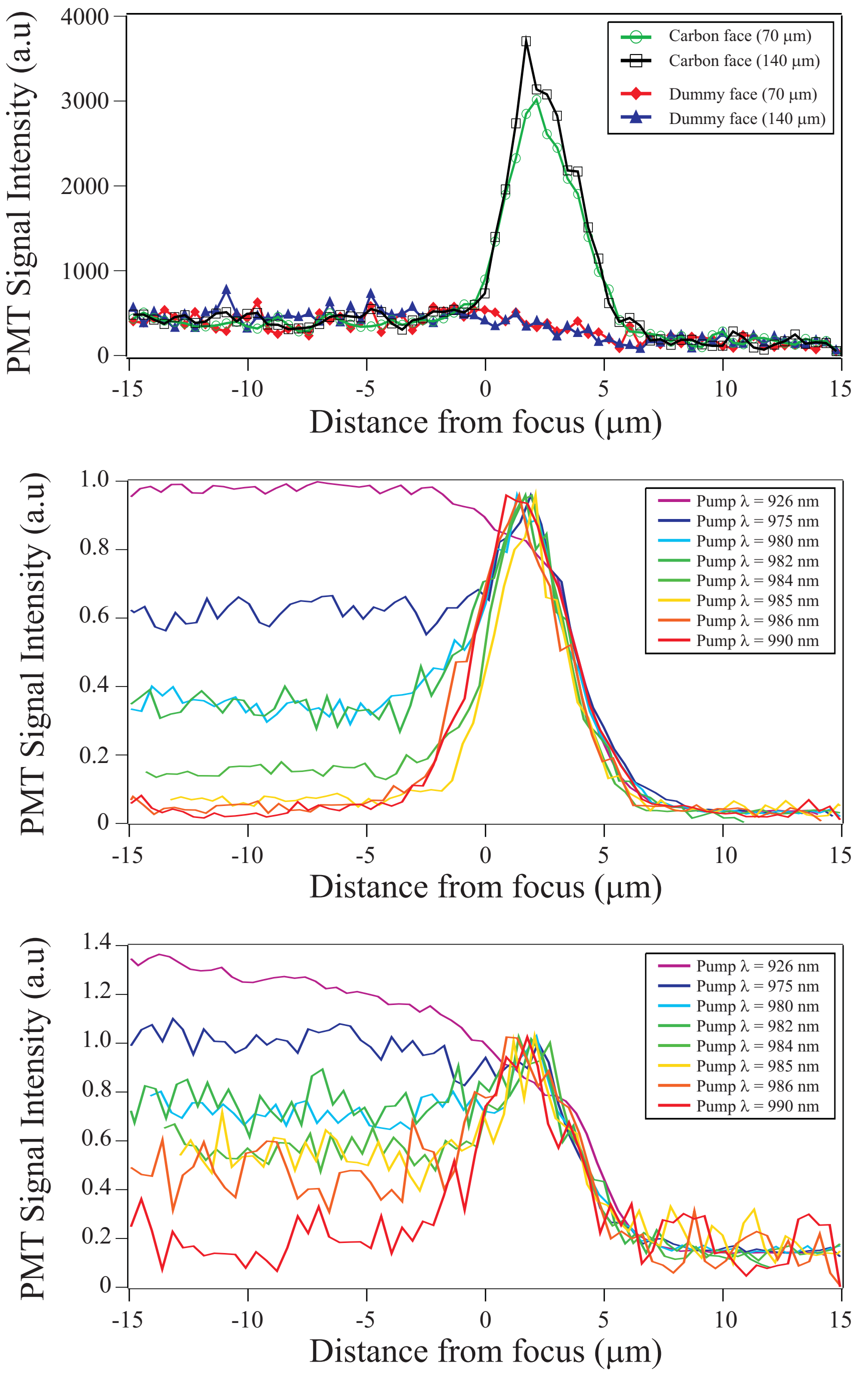

Figure 4.2.3: Interface signal as a function of pump wavelength and focal point. (a) Comparison between the carbon terminated face of epitaxial SiC and a dummy sample. Measurements taken 70 μm and 140 μm from the sample edge, with a pump wavelength of 985 nm. Reflection (b) and transmission (c) data for varying pump wavelengths. Data scaled to the peak intensity.

4.3 Signal Intensity Variation Measured by Raman Spectroscopy

Removal of a bulk contribution to the interface of graphitised epitaxial silicon carbide allows for high contrast imaging, purely from the carbon layers. Imaging with a nonlinear emission of 858 nm (signal and idler wavelengths of 985 nm and 1157 nm) the luminescence from the interface of the graphitised sample is shown in Figure 4.3.1(a,b) for both the carbon– and silicon–terminated faces. Intriguingly, the two faces show remarkably different features. For the carbon–terminated face one observes a grey background with micron–sized brighter regions. The silicon face instead shows dark regions on top of the grey background. Since the epitaxial growth is much faster on the carbon–terminated face[53] than the silicon–terminated face, one would expect regions of extra growth. Therefore, one may postulate that the difference in signal from the two faces arises from extra layers on the carbon face and an absence of layers on the silicon face.

To investigate this observation, the 2D Raman peak is measured on both faces of the sample. Due to the presence of silicon carbide peaks between 1400 cm^{-1} and 1800 cm^{-1} [108], the G peak is not used for this analysis.

Four well–spaced, random areas are chosen on both growth faces. A line scan is taken at each location which consists of 10 individual points spaced by 1 μm. Each measurement is taken with a 50× objective lens, resulting in a spot size of 1 μm. Since the features in the luminescence image are of the same scale one should resolve the differences in the two faces. The line scans are plotted in Figure 4.3.1(c,d). The static scan, centered at 2700 cm^{-1}, measures between 2472 cm^{-1} and 2916 cm^{-1}.

With no indication of a variation in peak intensity across both the silicon– and carbon–terminated faces, the postulation that the bright and dark areas are a result of extra layers on the carbon face and a lack of growth on the silicon face does not hold. A larger response is observed, as expected, on the carbon face due to the faster rate of growth.

The lack of any correlation between the luminescence images and the Raman spectra suggests that the observed features are not related to the number of carbon layers[109]. With electronically decoupled layers on the carbon–terminated face, one would expect discrete steps in the magnitude of the 2D peak as the number of carbon layers is increased. With a slower rate of growth on the silicon face, one would imagine that areas with no growth would be imaged since the samples are grown to have approximately one monolayer growth on the carbon face.

The question remains as to the origin of the luminescence features. The data suggests that the nonlinear imaging utilised here is a useful probe for features on the sample that Raman spectroscopy is not sensitive to. One possibility is large inhomogeneous doping of

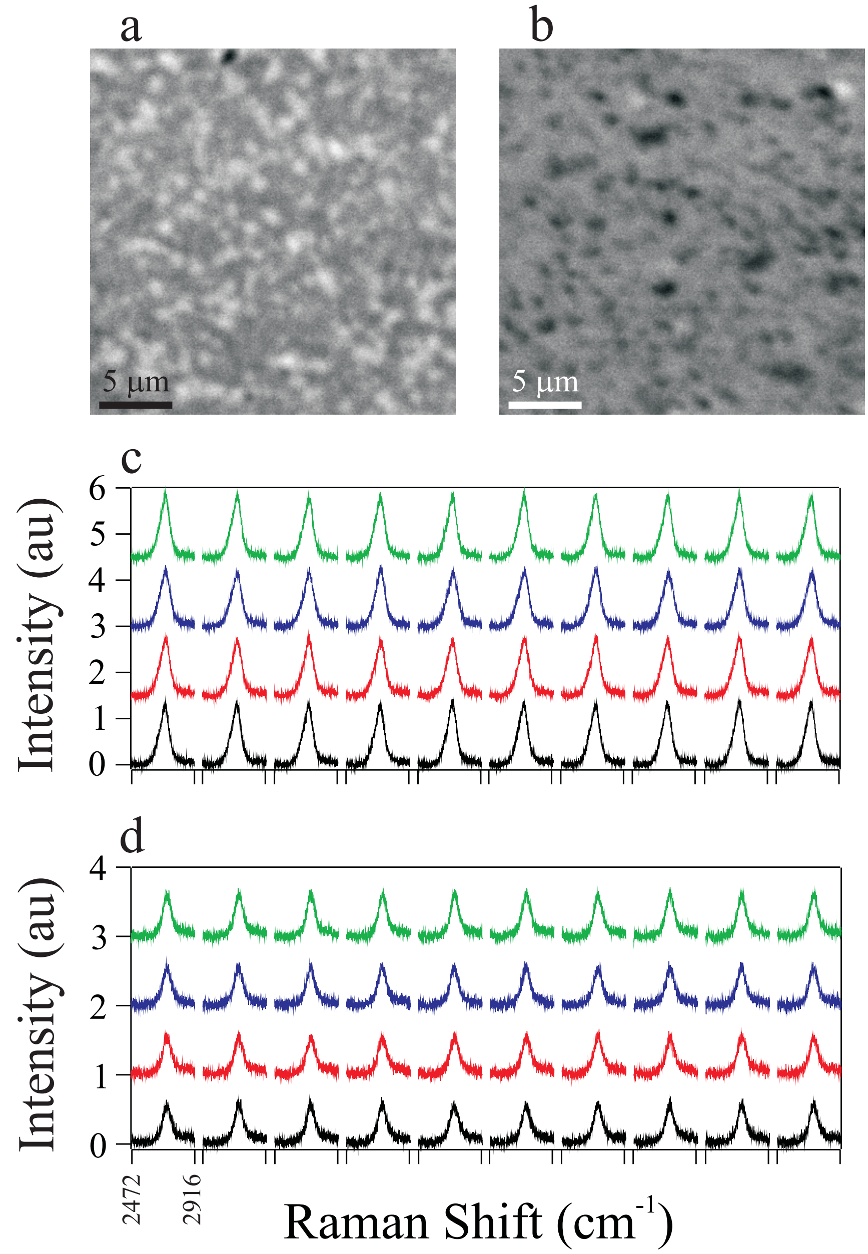

Figure 4.3.1: Luminescence image of the carbon–terminated (a) and silicon–terminated (b) faces of epitaxial graphene on silicon carbide. (c) 2D Raman peak for the carbon–terminated face. Four separate line scans are taken, each with 10 individual static Raman spectra. The data is offset in the x–axis for clarity. (d) Corresponding Raman spectra for the silicon–terminated face.

the epitaxial graphene. Nonlinear imaging could be sensitive to large doping in graphene samples and will be discussed further in Chapter 5.

4.4 Summary

In summary, luminescence from epitaxially grown graphene is used as an imaging technique for both the carbon– and silicon–terminated faces of silicon carbide. It is shown that a comparable nonlinear signal is returned from the bulk SiC substrate in both the forwards and epi directions. By imaging with a nonlinear emission wavelength outside the band–pass filter, the luminescence from the carbon layers is shown to dominate the bulk response, producing a high–contrast, surface sensitive signal.

The differences between the two growth regions is investigated via Raman spectroscopy which suggests the carbon layers are of uniform thickness. Lui *et al.*[72] discuss the origin of graphene luminescence after excitation by ultrafast laser pulses as arising from recombination between hot electron and hole systems. Luminescence intensity can therefore be expected to be strongly dependent on the relaxation timescales for hot electron/hole distributions. In Chapter 6 it is shown explicitly that different flakes can exhibit very different hot charge relaxation timescales. This suggests that the features in the luminescence images may be related to local relaxation timescales, possibly determined by the topology. Inhomogeneous local doping of the epitaxial graphene, as investigated in Chapter 5, may also be the cause of the decreased luminescence signal.

Chapter 5

Modification of Graphene via Ultrafast Pulses

5.1 Introduction

In this chapter, near–infrared ultrafast pulses are used to modify graphene. The pulses are focussed onto the samples and changes to the properties of the flakes are monitored with nonlinear imaging and Raman spectroscopy. With a plethora of research now being undertaken into the ultrafast optical properties of graphene, it is of vital importance to understand whether the samples are being modified in any way during measurements. With extremely high instantaneous electron and phonon temperatures being reached when photoexcited by intense ultrafast laser pulses, new chemical and physical modifications may become possible. Since nonlinear optical signals in graphene are proposed to be sensitive to charge relaxation timescales, nonlinear imaging is a useful tool to follow this photomodification process.

The nonlinear response of the samples is observed to decrease as a function of increasing exposure time and input power. By comparing the Raman spectra before and after modification the profiles of the G and 2D peaks, as well as the ratio of their intensities, is used to monitor changes in the doping levels and defect concentrations of flakes.

5.2 Loss of Four–Wave Mixing Signal at High Fluences

Using the mechanical exfoliation technique described in Section 2.1.1, a large monolayer flake, confirmed by Raman spectroscopy, is found on an oxidised silicon wafer, Figure 5.2.1(a). Imaging is achieved with the Levante OPO, Section 2.2.1.1, with signal and idler wavelengths of 926 nm and 1251 nm corresponding to a third–order emission at 735 nm. A 750 nm band–pass filter prevents the pump beams being detected. The large instantaneous intensity available with pulsed lasers allows for huge damage to be caused to samples fairly easily. Without attenuating the incident beams one can cause vaporisation of samples and so care must be taken to prevent over–exposure.

The damage threshold of graphene due to ultrafast optical pulses has been of interest in recent years. Several theoretical and experimental works point to a damage threshold of the order 100 mJ/cm^2 [110–114]. It is worth noting here that Currie *et al.* [113] demonstrate a threshold as low as 14 mJ/cm^2, although these measurement were performed on CVD graphene where one would expect a higher density of defects, as observed by a large defect–induced Raman peak, which will lower the threshold for damage.

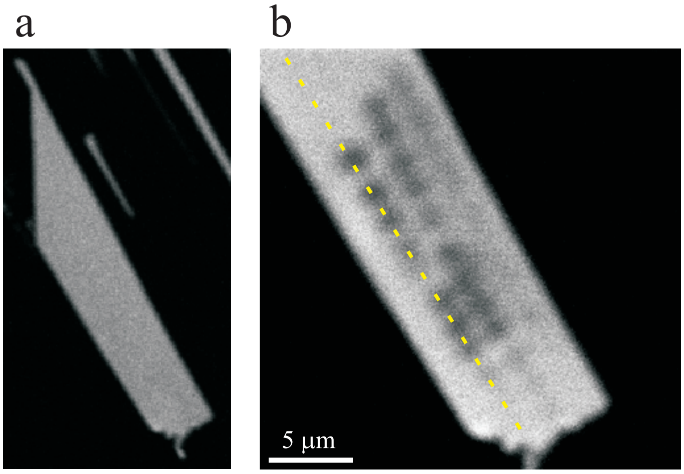

Figure 5.2.1: (a) Four–wave mixing image of a large monolayer sample prior to modification. (b) The same monolayer after modification. Small square areas are raster scanned to induce a change in the response of the flake. On the right hand side of the sample, 5 s exposures are performed at increasing intensities, beginning with 1.5 mW in the lower right hand corner up to 14 mW in the top right hand corner. The other four areas vary exposure time from 5 s to 60 s and incident powers of 9 mW to 12 mW.

In Figure 5.2.1(b) the monolayer sample is exposed to increasing intensities of near–infrared pulses in order to investigate the intermediate effects of ultrafast pulses on the sample before ablation occurs. The Fluoview scan unit is used to raster the incident beams over micron scale squares. The bottom right hand corner of the flake is exposed to a total of 1.5 mW of 926 nm and 1251 nm, 6 ps pulses for 5 seconds. No observable modification is observed in the nonlinear image. Moving up the right hand side of the sample, the exposure intensity is increased to a maximum value of 14 mW. A decrease in the nonlinear signal magnitude is clearly noticeable. Four separate strips on the sample are investigated as a function of exposure time. Intensities of 9 mW (bottom centre), 10 mW (bottom left), 11 mW (top centre) and 12 mW (top left) are raster scanned from between 5 seconds and 60 seconds. The incident power, ranging from 1.5 mW to 14 mW, corresponds to a fluence at the sample of approximately 2 mJ/cm^2 and 20 mJ/cm^2.

To quantify the magnitude of the decrease in nonlinear signal as a function of exposure time, the emission at each modified area is measured and normalised to the unmodified response of the flake, Figure 5.2.2. For each of the input intensities, an asymptote is observed in the normalised intensity of approximately 50%. The data suggests that increasing the exposure time past 30 seconds causes no further modification to the sample. If the decrease in signal intensity were related to induced defects and ablation of the flake then one would expect a constant decline in magnitude as a function of time, continuing until the response fell to zero.

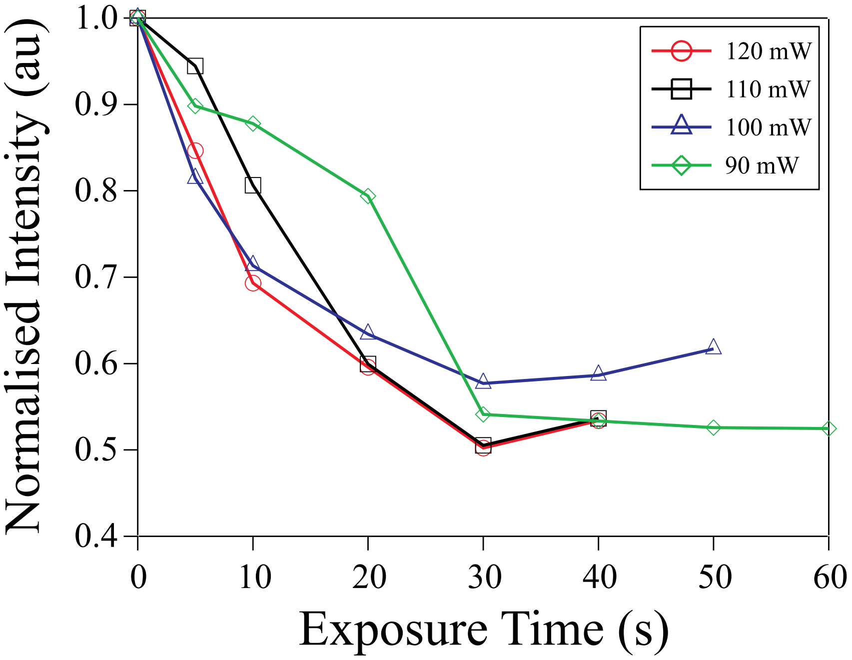

Figure 5.2.2: Four–wave mixing signal intensity as a function of exposure time for various input powers. The modified regions in Figure 5.2.1 are normalised to the response of the unmodified region of the flake. For all input powers one observes a decrease in nonlinear signal which saturates after approximately 30 s of exposure.

To investigate any induced damage to the flake a Raman line scan is taken along the dashed line in Figure 5.2.1, shown in Figure 5.2.3. Spectra are acquired with a Renishaw RM1000 microscope operating at 532 nm, Section 2.3. The measurement begins 15 μm into the unmodified region and continues in steps of 0.5 μm towards the bottom of the flake. The spectrum is centered around 1500 cm^{-1} so as to include both the G and D peaks (at 1580 cm^{-1} and 1350 cm^{-1} respectively). Initially the spectra are uniform and show a constant value for the G peak position. At 15 μm the modified region is reached and an abrupt shift in the position of the G peak is observed. At the far end of the scan, where the measurement again reaches an unmodified area, the peak position recovers to the initial value. Even with these large modifications, the presence of a defect peak is extremely small, suggesting that defects are not the cause of the reduction in nonlinear signal magnitude.

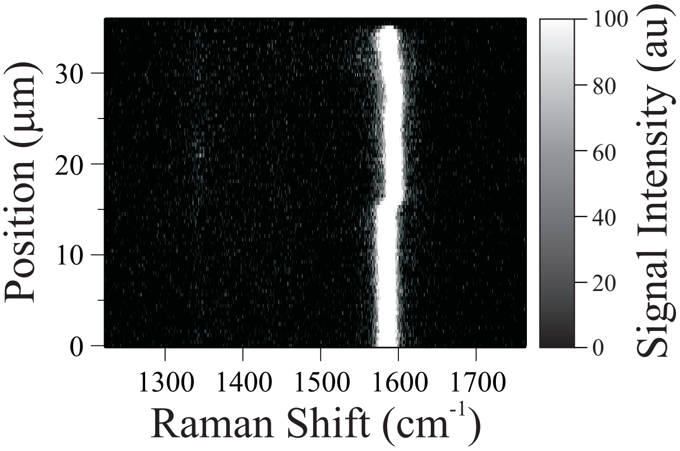

Figure 5.2.3: Raman spectra along the dashed line in Figure 5.2.1, encompassing the D and G regions of the graphene spectrum. A shift in the position of the G peak is observed when crossing from the unmodified region of the flake, $0-15$ μm, to the modified region above 15 μm. No significant defect peak is observed at 1350 cm^{-1}.

Investigations into high levels of doping in graphene via Raman spectroscopy[65,115] demonstrate both a stiffening of the G peak position and a decrease in the full–width half–maximum. For both electron and hole doping, the position of the G peak is up–shifted due to the removal of the Kohn anomaly at the Γ point[116,117]. The Kohn anomaly arises due to screening of lattice vibrations from conduction electrons, occurring for wavevectors corresponding to $\mathbf{q} = 2\mathbf{k}_\mathrm{F}$, where $\mathbf{k}_\mathrm{F}$ is the Fermi wavevector. The anomaly softens the phonon mode, meaning a doped layer should stiffen as the anomaly is removed. The width of the G peak is decreased with doping as the decay of electron–hole pairs via phonon decay is prevented by Pauli blocking[65,117–119]. This effect saturates once the shift in the Fermi energy exceeds $E_\mathrm{phonon}/2$.

Large doping due to high excitation fluences explains both the observed shift in the G peak position, Figure 5.2.3 and the reduction in the nonlinear response. For high levels of doping, the excitation of the low energy idler pulse may be blocked. With an idler wavelength of 1251 nm, this corresponds in a shift from the Dirac point of 0.5 eV. This is investigated in more detail in the next section.

5.3 Monitoring Modification via Raman Spectroscopy

To investigate whether the cause of graphene modification via ultrafast pulses is a result of large shifts in the Fermi level, a pristine flake deposited on a glass coverslip is uniformly exposed. A combination of 871 nm signal and 1064 nm are used to generate a nonlinear emission of 737 nm, used to align the beams and find the optimal focal point. A 750 nm band–pass filter is used to exclude the pump beams.

Prior to exposure a Raman map is taken of the flake, encompassing both the G and 2D peaks. This provides a reference for the G peak position and width, as well as the ratio between the intensities of the G and 2D peaks.

The sample is brought to focus using low intensity pump beams, a nonlinear image is shown in the inset of Figure 5.3.1. The sample is irradiated with 6 ps pulses which are raster scanned evenly over the entire flake with a fluence of 1.5 mJ/cm^2 for approximately 30 seconds. The sample is remeasured in the Raman microscope and a direct comparison made between the pre– and post–modification areas.

The Raman data is fit with two Lorentzian curves centered at approximately 1580 cm^{-1} and 2700 cm^{-1}. The absolute position of the peaks, the FWHM and the intensity are found with a least–squares fitting routine. Contribution to measurement assistance and data fitting by E. Alexeev is greatly acknowledged.

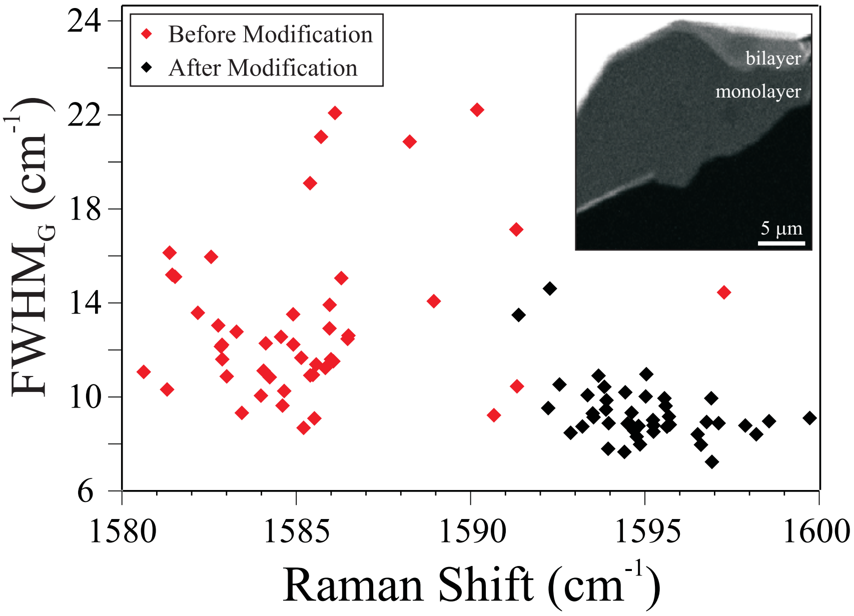

Figure 5.3.1: Full–width half–maximum of the G peak, as a function of peak position, before and after exposure to ultrafast pulses. A stiffening of the G mode and a reduction in peak width is observed for the sample after irradiation. Inset: Low intensity nonlinear image showing the investigated monolayer sample.

The full–width half–maximum of the G peak is plotted as function of the peak position before and after modification in Figure 5.3.1. Prior to irradiation the sample demonstrates a scattered array of G peak positions, with most points found at a Raman shift of approximately 1585 cm^{-1}. The width of the peak also shows a broad distribution, but most points are found above 10 cm^{-1}. The distribution in peak width and position hints at inhomogeneity on the micron scale within the flake, evidence of which has been observed previously[115]. After irradiation both the peak width and position are found to group together at a larger shift, $\sim$ 1585 cm^{-1}, and a narrower peak width, $\sim$ 9 cm^{-1}. Both the shift in position and decrease in width are indications of large doping.

From the work by Das *et al.*[65], a shift in the G peak position from 1585 cm^{-1} to 1595 cm^{-1} corresponds to a shift in the Fermi level of up to 500 meV. The reduction in the FWHM of the G peak can only give a lower bound to the doping level as a saturation is reached in the peak width within $\sim$ 400 meV[65].

Comparing the ratio of the intensities of the 2D and G peaks in Figure 5.3.2, one observes a striking change after modulation. The intensity of the 2D peak prior to modification is up to 6 times that of the G peak, corresponding to a doping level close to the neutrality point. After modification, all data points collapse to a value of approximately 1.5, which again is indicative of large doping of the order 500 meV[65,120]. By scanning the signal and 1064 nm pulses uniformly over the sample, a homogeneous doping level is observed.

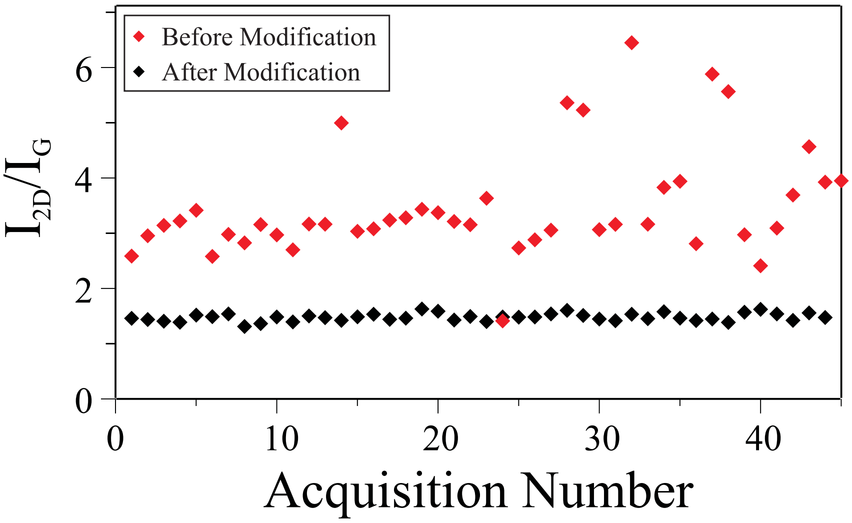

Figure 5.3.2: Intensity of the 2D peak, normalised to the G peak intensity, before and after irradiation for several measurements.

With high levels of doping the shift of the G peak position is symmetric with respect to n–type or p–type doping[65,121]. The shift can only be used as an estimate for the absolute value of the doping level, not direction. Comparing estimates of doping levels from the G peak shift, G peak FWHM decrease and the change in the ratio of the normalised 2D peak intensity, an induced doping level of the order 500 meV is shown to be appropriate. This agrees with the decrease in third order nonlinear signal magnitude may explain why the decrease in signal reaches an asymptote. Comparing this value to the shift in Fermi level available with standard silicon back–gating, one would require a back gate voltage of 260 V to reach this value. Typically dielectric breakdown is observed at $\sim$ 100 V.

In order to fully explain the doping found from modified flakes the optical measurements are required to be complimented with transport experiments. A shift in the Fermi level can therefore be independently verified, along with information regarding the direction of doping. These measurements are currently ongoing.

Modification of the Raman spectra of graphene has been demonstrated by Mohiuddin *et al.*[122], which shows a splitting of the G peak and a shift in the position of the 2D peak for the application of uniaxial strain. Since these features are not observed, an increase or decrease in strain is not thought to be relevant.

It is interesting to note that the fluence used on the sample, 1.5 mJ/cm^2, is significantly lower than that required to noticeably modify the flake on the oxidised wafer in the previous section. The reason for this is unclear as the only differences in the measurements are the incident wavelengths, which are negligibly different, and the underlying substrates. This suggests that the previously defined unmodified regions could themselves be modified as a result of low intensity imaging. Although greater than the fluence used for typical pump–probe ($\sim$ 0.6 mJ/cm^2) and four–wave mixing ($\sim$ 1.2 mJ/cm^2) measurements, one can not rule out unintentional modification during these measurements, although one would expect to see evidence of this in the time–resolved data. The mechanism of the proposed doping is an open question.

5.4 Summary

In summary, modification of graphene via ultrafast near–infrared pulses is shown to cause a decrease in the third–order nonlinear signal. Varying the input intensity and duration of exposure decreases the response to an asymptotic value of approximately 50% of the normalised, unmodified flake response.

Comparing a large data set of Raman measurements before and after irradiation points towards a huge shift in the Fermi level of up to 500 meV. Without complimentary transport data the direction of the Fermi shift can not be known but is under current investigation. Modification is observed with prolonged exposure to just 1.5 mJ/cm^2, below the reported value of the ablation threshold but more comparable to fluences used in four–wave mixing and pump–probe spectroscopy.

Chapter 6

Hot Phonon Decay in Supported and Suspended Exfoliated Graphene

6.1 Introduction

Hot electron relaxation in large area, epitaxially grown graphene layers using pump–probe spectroscopy has been studied previously[28,59,66,67,123–127]. These measurements point to biexponential decay dynamics, characterised by a fast $\sim$ 100 fs component and a slow $\sim$ 2 ps component. This was confirmed in Section 2.2.3.1. There is, however, significant variation in the reported timescales. Epitaxial graphene exhibits inhomogeneity in layer thickness on the micron scale[59] and can result in significant variability in relaxation dynamics from sample to sample[66]. Pump–probe measurements have also been performed on mechanically exfoliated few–layer graphene[71,128], which is homogeneous over much greater length scales. It was concluded that the slow relaxation process was caused by coupling to phonons in the substrate[128].

In this chapter, the ultrafast relaxation of hot charge carriers in mono– and few–layer graphene is investigated for both supported and suspended samples. Near–infrared femtosecond pulses are used to measure the time delayed pump–probe signal and a coupled rate equation, describing the exchange of energy from hot electrons to optical phonons, is used to fit to the data and extract the phonon relaxation times.

From the raw data it is clear to see that there is a difference in the relaxation rate when monolayer graphene is compared to few–layer graphene. The potential role of the substrate in this effect is ruled out by suspending the samples over pre–defined etched holes and comparing the relaxation rates. Possible decay mechanisms, such as flexural phonons, that could cause such an enhancement are discussed.

Further measurements are taken, under the same experimental conditions, to investigate the ultrafast relaxation in large area graphitised epitaxial silicon carbide. The relaxation rate is found to be independent of the number of carbon layers and agrees well with the asymptotic value found in the exfoliated samples.

6.2 Method

Pump-probe measurements are performed using the Mira 900D Ti:sapphire mode–locked laser, centre wavelength 830 nm, with a pulse width $\sim$ 180 fs. This acts as the pump beam for the experiment as well as pumping the optical parametric oscillator (OPO). The OPO is tunable from 1100 nm to 1600 nm and provides the lower energy probe.

The beams are aligned collinearly, so as to overlap in space, and adjusted through separate beam expanders to possess the same amount of divergence. This allows the beams to be focussed through the objective lens to the same depth. A schematic is shown in Figure 6.2.1(a). Once aligned through a pair of separated pinholes, the beams are passed through a Fluoview scan unit and into an inverted microscope, Figure 6.2.1(b). The beams are brought to focus through a 1.2 numerical aperture (NA) water immersion lens, resulting in a spatial resolution of $\leq 1.5\ \mu$m. Importantly, this value is much smaller than the size of the samples investigated. The oscillating mirrors within the scan unit allow for the beams to be raster–scanned over a $250\ \mu$m $\times$ $250\ \mu$m area. Transmitted light is then collected through a collimating lens and focussed onto a PMT for imaging and alignment. For the reflected light, a dichroic mirror in the microscope, Figure 6.2.1(b), preferentially reflects the longer probe wavelengths. Further 1100 nm long–pass filters are placed in front of the reflection diode to exclude all pump light.

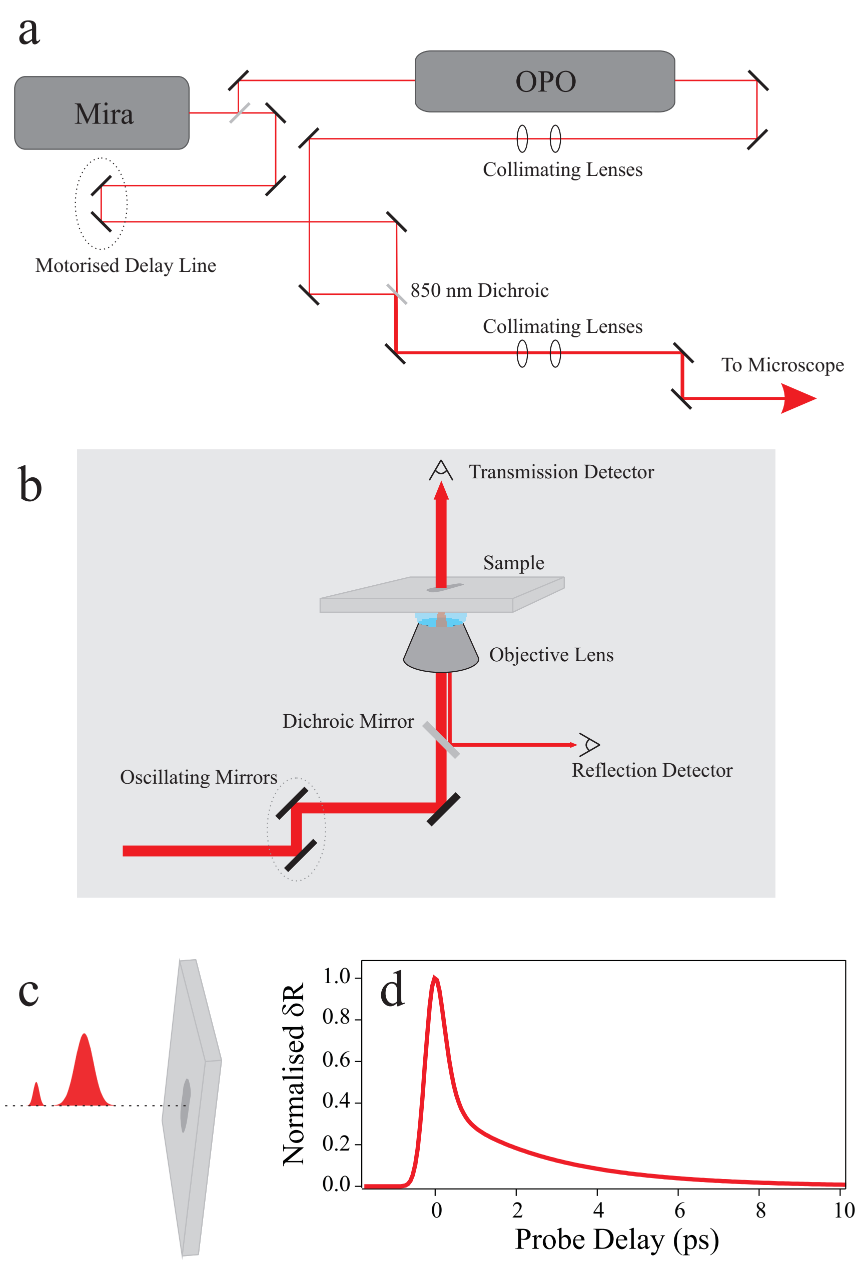

Figure 6.2.1: Schematic design of the pump-probe setup. (a) A schmatic of the beam paths around the optical bench. (b) A zoomed–in view of the beams entering the microscope, with a high numerical aperture water immersion lens to ensure maximum spatial resolution. Detection is possible in both transmission and reflection, for the latter a dichroic filter is used to help separate the probe from the pump (paths offset for clarity). (c) A schematic showing the arrival of the pump and probe beams. Using the delay line in (a) the pump pulse is translated in time, relative to the probe. (d) A typical pump probe measurement for a graphite sample, the pulses are overlapped at $t = 0$.

The probe beam is fully optimised with the use of a mechanical chopper. The beam is chopped at approximately 800 Hz (although this value is unimportant) and the output of the reflection detector is maximised either via a lockin amplifier (preferable) or an oscilloscope. The pump beam is then optimised by chopping the pump and monitoring the pump–probe signal whilst adjusting the delay line. Once the beams are temporally overlapped, a maximum signal is measured. A fine adjustment of the last pump mirror can then be used to maximise the total signal. The delay line is then returned to approximately 2 ps behind the overlap position.

The pump and probe beams are set into a ratio of $> 10 : 1$ going into the microscope. This is to ensure the measurement is a valid one, i.e. that the probe does not strongly influence the electron (hole) distribution in the conduction (valence) band.

For the majority of the measurements taken, the probe wavelength used is 1120 nm. Figure 6.2.2(a) plots the overlapped pump–probe signal magnitude for three different probe wavelengths, all set to the same incident power. Due to the response of the detector decreasing for longer wavelengths, the signal magnitude is found to be largest for 1120 nm. For further comparison, the 1.2 NA water immersion lens is compared to a 40×, 0.55 NA objective. Due to the smaller spot size and focal volume associated with the higher numerical aperture lens, a larger signal is observed.

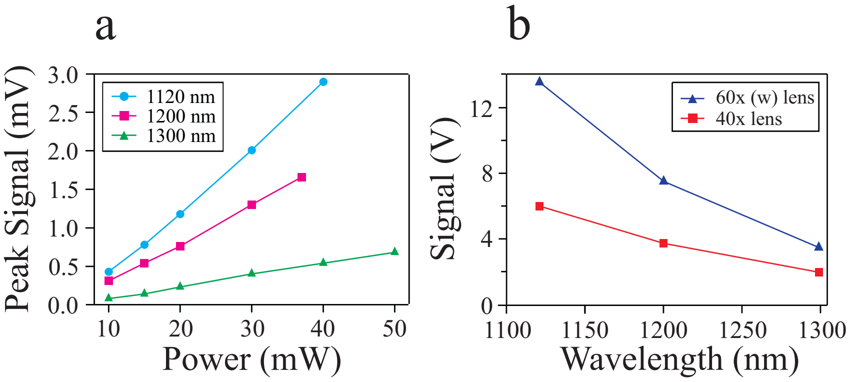

Figure 6.2.2: Comparing signal magnitude with varying probe wavelength and objective lens. (a) Overlapped pump–probe signal magnitude for three different probe wavelengths. The total incident power is fixed at 10 mW in a pump to probe ratio of $10 : 1$. (b) Comparing the signal magnitude, as a function of wavelength, for the 1.2 NA and 0.55 NA lenses. Signal is collected on an oscilloscope with the probe modulated at 800 Hz.

6.2.1 Sample Fabrication

Samples are prepared from mechanically exfoliated natural graphite deposited on 100 μm thick glass cover slides. In Section 1.4.2 the optical contrast as a function of the number of graphene layers is estimated through the use of the Fresnel equations at interfaces. With this knowledge, flakes from a single layer up to six layers are located and characterised. As a first estimate, the number of layers is calculated purely from the optical contrast, monolayers and bilayers are then confirmed from the profile of their 2D Raman mode (see Section 1.4.3).

The suspended graphene samples are fabricated by pre–patterning glass coverslides with a reactive ion etching (RIE) machine, explained in Section 2.1.3. Flakes are then deposited onto the substrate and characterised in the same way. Flakes that span the etched holes are confirmed to be suspended via atomic force microscopy.

6.3 Coupled Rate Equation Model

In order to better understand the mechanisms of the decay, a simple coupled rate equation model, which estimates the electron and optical phonon temperatures after photoexcitation from ultrafast optical and near–infrared pulses is used to fit the data. This model is based on earlier work by Wang *et. al*[28] and Rana *et. al*[70] and developed here with assistance from S. Hornett and E. Hendry.

After excitation from an ultrafast optical pulse, electrons are excited into the conduction band a distance $\hbar\omega_{\text{photon}}/2$ above the Dirac point. These hot electrons quickly thermalise via electron–electron scattering into available states up and down the conduction band, until a Fermi–Dirac distribution is established[28,73,129–131]. Relaxation of electrons is then dominated via high energy optical phonons until all the electrons have fully relaxed into their original states, Section 2.2.3.

The following coupled rate equation model describes how the thermalised distribution of electrons first transfers energy to the phonon bath before reaching a pseudo–equilibrium state. The energy loss from the excited system is then mediated by the rate at which the hot phonons can decay, anharmonically, into acoustic modes. One first begins with the phonon generation rate, Γ_{ph}, which is calculated using the relation

$$\Gamma_{\text{ph}} = \alpha \int_{-\infty}^{\infty} E(E - \hbar\omega_{\text{ph}}) \times \left[\rho_{\text{e}} - \rho_{\text{a}}\right] \text{d}E, \tag{6.3.1}$$

where ω_{ph} is the optical phonon frequency ($\sim$ 180 meV). The probability of emitting, ρ_{e}, and absorbing, ρ_{a}, a phonon are

$$\begin{aligned} \rho_{\text{e}} &= f(\text{E})(1 - f(\text{E} - \hbar\omega_{\text{ph}}))(n_{\text{ph}} + 1) \\ \rho_{\text{a}} &= f(\text{E} - \hbar\omega_{\text{ph}})(1 - f(\text{E}))n_{\text{ph}}. \end{aligned} \tag{6.3.2}$$

Here, $f(\text{E})$ is the Fermi–Dirac distribution of electrons for a given electron temperature, T_{el}. The electron coupling strength, α, is given by[70]

$$\alpha = \frac{9}{2} \times \beta^2 \left[\pi\, \rho\, \omega_{\text{ph}}\, \hbar^4\, v_{\text{F}}^4\right]^{-1}. \tag{6.3.3}$$

The density of graphene, ($\rho \sim 7.6 \times 10^{-7}$ kg/m^2), Fermi velocity, $v_{\text{F}} \sim 1 \times 10^6$ ms^{-1} and deformation potential, $\beta = 45$ eV/nm[70], are known. The phonon occupation number, n_{ph}, is related to the electron temperature through

$$\frac{\mathrm{d}T_{\text{el}}}{\mathrm{d}t} = -2\frac{\Gamma_{\text{ph}}\hbar\omega_{\text{ph}}}{C_{\text{el}}}, \tag{6.3.4}$$

where C_{el} is the electronic heat capacity[132]. Equation 6.3.4 has two components, corresponding to the Γ and K point phonon contributions. For simplicity, these have been written together, due to their similar values. This is justified as treating them separately, or together, yield the same results.

The rate of optical phonon generation is governed by

$$\frac{\mathrm{d}n_{\text{ph}}}{\mathrm{d}t} = \frac{\Gamma_{\text{ph}}}{M_{\text{ph}}} - \frac{n_{\text{ph}} - n^0_{\text{ph}}}{\tau_{\text{ph}}}, \tag{6.3.5}$$

where n^0_{ph} is the phonon occupation at room temperature, T_0, and τ_{ph} is the phonon relaxation time. The second term in Equation 6.3.5 describes the anharmonic decay of hot phonons. M_{ph} is the number of Γ and K point phonons (per unit area) that are able to couple to the hot electrons, which is estimated by considering the maximum and minimum momentum possible for an emitted Γ or K point phonon[28]. This gives

$$M_{\text{ph}} = \left(\frac{2}{4\pi}\right)\left[\left(\frac{\sqrt{2}E_{\text{max}}}{\hbar v_{\text{F}}}\right)^2 - \left(\frac{\omega_{\text{ph}}}{v_{\text{F}}}\right)^2\right], \tag{6.3.6}$$

where E_{max} is the upper energy of the hot electons that are able to emit phonons, found by calculating Γ_{ph} for a given T_{el}. The factor $\sqrt{2}$ in front of E_{max} is due to the conservation of pseudospin, which limits scattering to states within the same semi–cone in the Brillouin zone. The factor 2 arises from valley degeneracy.

Using Equation 6.3.4, one can evaluate the temperature of the electron bath as a function of time after excitation. Since the energy from the excitation pulse is dissipated through intraband optical transitions, an initial electron temperature $T_{\text{el}}(0)$ is calculated from the absorbed fluence and C_{el}. Cooling during the excitation pulse is accounted for by estimating an average emission of 5 optical phonons per excited electron during the excitation pulse[28]. Given these starting conditions, a time dependent reflection change is found using[133]

$$\delta R(t) \propto \tanh\left(\frac{E_{\text{pr}}}{4k_B T_0}\right) - \tanh\left(\frac{E_{\text{pr}}}{4k_B T_{\text{el}}(t)}\right), \tag{6.3.7}$$

which gives the change in the strength of interband transitions of the probe pulse due to the electron temperature, $T_{\text{el}}(t)$, and the probe photon energy, E_{pr}. Probe energies used in the experiments, ranging from $0.94 - 1.11$ eV ($1320 - 1120$ nm), are considered. After convolving Equation 6.3.7 with the correlation of the pulses, and using just the absorbed pump fluence and τ_{ph} as fitting parameters, the time dependent change in reflection can be fully described.

Figure 6.3.1(a) shows an example of the electron and optical phonon temperatures, as a function of time, for the coupled rate equation model. Here, a convoluted Gaussian pulse of width 250 fs is used, along with pump and probe energies of 1.49 eV and 1.11 eV, (830 nm and 1120 nm) respectively. The absorbed pump fluence is 0.05 J/m^2, coupled with a decay constant of 2.0 ps.

The electron temperature in Figure 6.3.1(a) jumps to a high temperature at $t = 0$. This is the point at which the pump pulse irradiates the sample, exciting electrons high into the conduction band. The strong electron–phonon coupling in graphene is then observed by the evolution of the Γ and K phonon temperatures. The electrons transfer energy to the phonon bath until an equilibrium has been reached. The system then evolves as energy is dissipated via the decay of hot optical phonons.

With knowledge of the electron and phonon temperatures as a function of time after excitation, Equation 6.3.7, convolved with the Gaussian pulses, plots the profile of the electron decay, Figure 6.3.1(b). By varying only the phonon relaxation time, τ_{ph}, and the absorbed fluence, the model can be used to fit the pump–probe data for graphene measurements and return the decay rates.

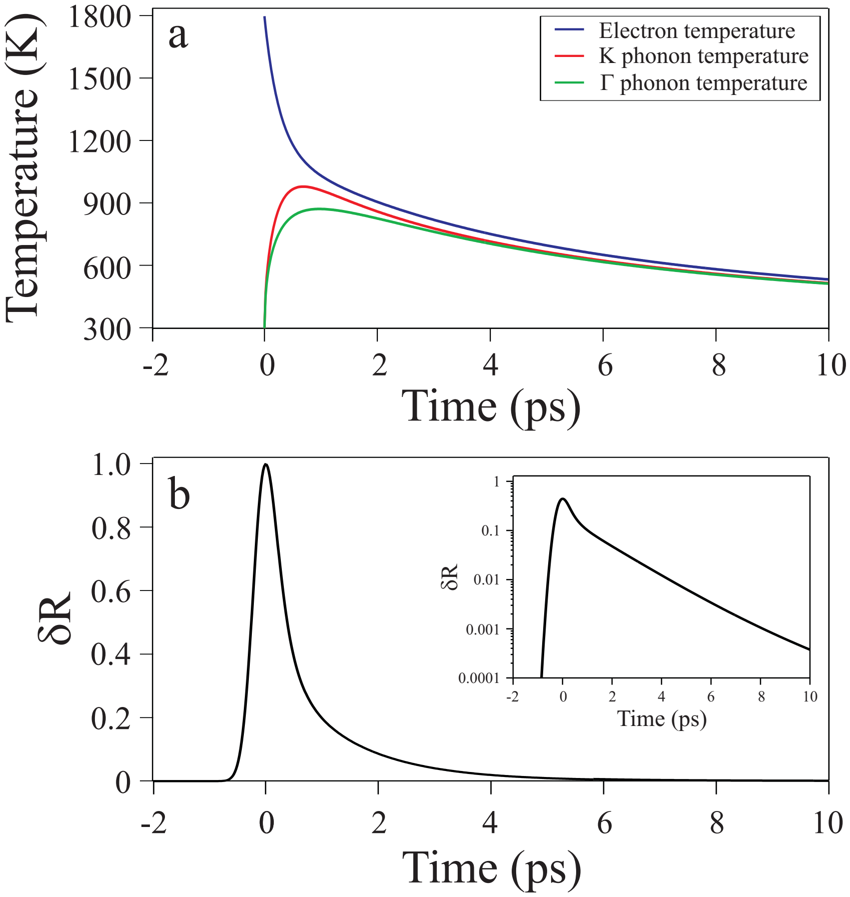

Figure 6.3.1: Modelled curves using the coupled rate equation model. (a) For an excitation at $t = 0$, the temperature of electrons and optical phonons (both the K point and Γ point) are plotted as a function of time. (b) Convoluting the 250 fs pulse with the absorbance, the differential reflection for electrons pumped at 830 nm and probed at 1120 nm is plotted as a function of probe delay. Inset: The same data plotted on a log scale which clearly distinguishes the two relaxation regions after photoexcitation ($0 < t \lesssim 0.5$ ps and $t \gtrsim 0.5$ ps).

Contributions from inter– and intraband transitions have been recently investigated in ultrafast pump–probe measurements in graphene[131,134]. For low fluences, where the induced electron temperature is relatively low, pump–induced changes to the intraband optical conductivity dominate the transient signal. For the range of fluences investigated in this work, changes to the interband optical conductivity dominate, i.e. when the pump and probe pulses are overlapped in time the pump pulse excites electrons and blocks available transitions for the probe, resulting in a decrease in the reflection from the sample. No evidence of characteristic interband contributions observed by Malard *et al.*[134] are seen. Consequently, the relaxation dynamics are fitted with a relatively simple coupled rate equation which describes the time dependent oscillator strength of interband transitions, which depends on the dynamical electron and phonon temperatures.

6.4 Pump-Probe Spectroscopy for Few–Layer Supported Graphene

Pump probe spectroscopy is a form of nonlinear measurement. One must first be careful in ensuring the pump and probe pulses are set to a large enough ratio such that the probe beam does not modify the electron distribution and that the sample is not being saturated from pulses which are too intense. Figure 6.4.1(a) plots the overlapped ($t = 0$) pump–probe signal magnitude as a function of the ratio of the pump and probe beam intensities. The combined input intensity is kept low to avoid saturation. Increasing the pump (with a fixed probe) shows how the signal is linearly dependent on the magnitude of the pump. Plotting the peak signal now as a function of the product of the two input intensities, Figure 6.4.1(b), and increasing the total fluence, a saturation in the signal can be reached. This puts an upper bound on the absolute fluence that can be used for measurements. Typically, the combined input intensity used is of the order 5 mW.

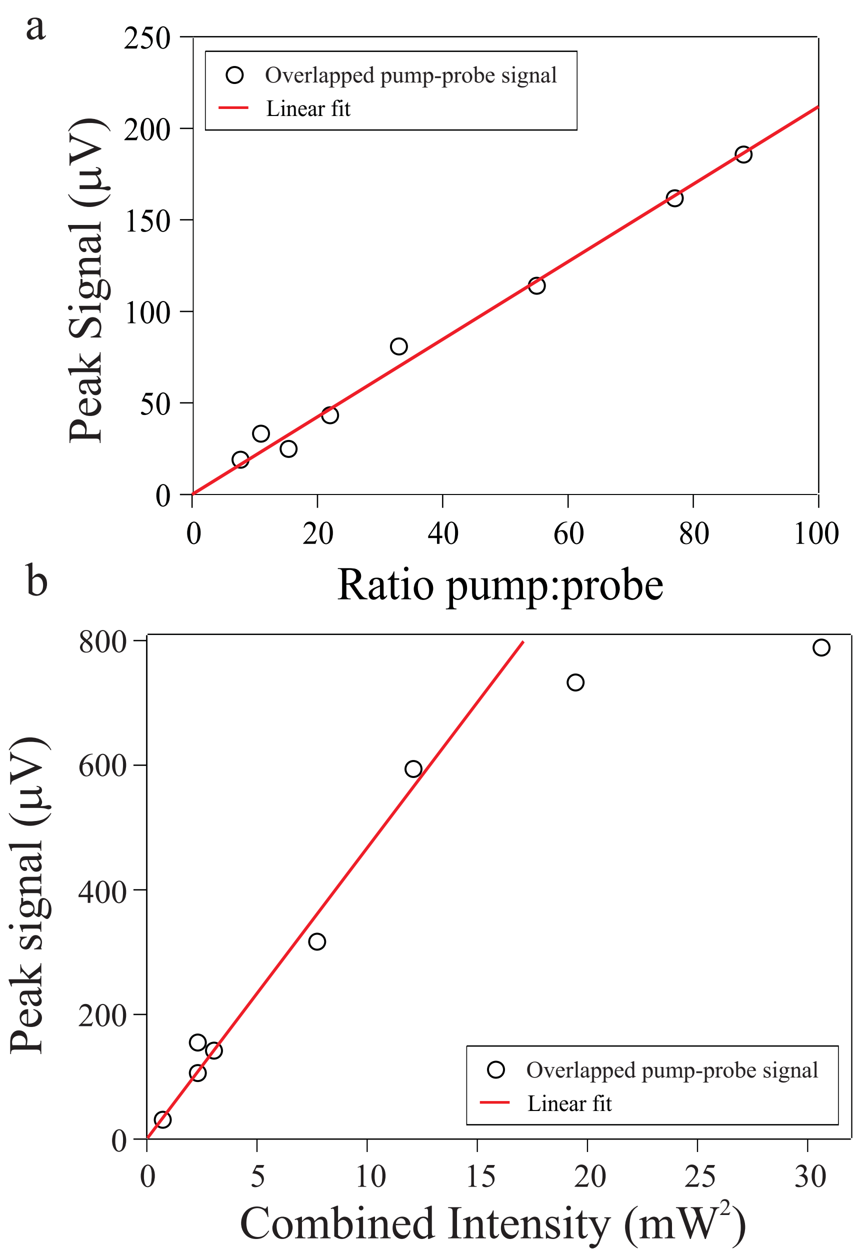

Figure 6.4.1: (a) Linear dependence of the peak overlapped pump–probe signal plotted as a ratio of the pump and probe input intensities. Data is obtained for low combined intensity, so as not to saturate the signal. (b) Linear dependence of the peak pump–probe signal as a function of the combined pump and probe intensities. For high values of the pump intensity a saturation in the maximum signal is observed.

Within the coupled rate equation model, the energy at which the electrons are probed is taken into account. By first measuring a sample at different probe energies one can ascertain whether the model returns the correct physical picture. Figure 6.4.2 shows two measurements of a 10–layer sample, taken at probe wavelengths of 1120 nm (1.11 eV) and 1320 nm (0.94 eV). By probing higher energy electrons a faster decay rate is observed. This is considered within the model and the decay rates returned from the fits are $\tau_{\mathrm{ph}} =$

3.60 ± 0.05 ps and $\tau_{\text{ph}} = 3.35 \pm 0.1$ ps.

Hot optical phonon lifetimes in graphene have been the subject of theoretical calculations by Bonini *et. al*[135]. The anharmonic decay of hot optical phonons into acoustic modes returned lifetimes of the order 2–4 ps for both zone–centre and zone–edge modes, in a temperature range of 500–900 K. The extracted decay rates are clearly consistent with these calculations, as well as phonon lifetimes extracted from time–resolved Raman measurements by Yan *et. al*[136]. Agreement is also found between these measurements and recent pump–probe measurements on epitaxially grown graphene by Wang *et. al*[28]. The slightly longer relaxation times found here for bulk samples ($\sim$ 3 ps), compared to $\sim$ 2.2 ps found by Yan *et.al*[136], are attributed to induced heating due to high excitation fluences in the latter (an absorbed fluence of 2.0 J/m^2, compared with ~ 0.05 J/m^2 here). Kang *et. al*[137] and Bonini *et. al*[135] show a decrease in phonon lifetimes for graphene and graphite with increasing temperature.

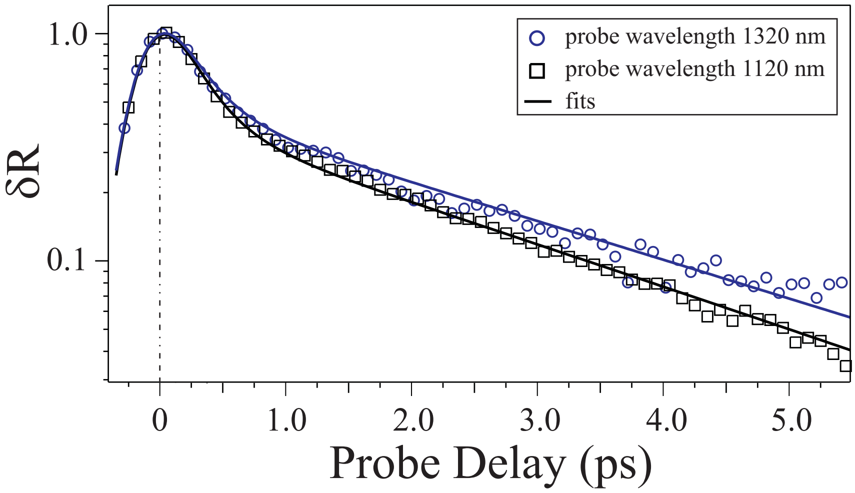

Figure 6.4.2: Differential reflectivity as a function of probe delay for a 10–layer flake. Measurements are performed at 1120 nm and 1320 nm (1.11 eV and 0.94 eV) to demonstrate the wavelength dependence of the relaxation. The coupled rate equation model is used to fit to the data.

Measurements are performed as a function of the number of graphene layers in a large number of different flakes. Figure 6.4.3(a) contrasts the reflectivity measured in flakes from single to six layers supported on a glass substrate. One observes a clear correlation between layer number and decay rate, where a faster relaxation occurs for the thinner samples, Figure 6.4.3(b). However, for ~ 4 layers and above one finds that all of the data collapse onto a single gradient. This indicates that at these thicknesses the sample behaves as a bulk material and the rate of relaxation is constant. This suggests that the mechanism that removes energy from the system in thin layers is not available to the thicker layers.

Variation from sample to sample is observed for all layer thicknesses. With the use of a large data set one may obtain enough statistics in order to reveal the trend within the data. The fitting routine contains several fixed parameters, such as pulse width, ~ 250 fs, probe energy, 1.11 eV, and a shift in the probe delay to overlap the fitted curve and the data at $t = 0$. The only free parameters are the relaxation time, τ_{ph}, and the absorbed fluence.

One should note here that the duration of the pulses used, approximately 250 fs, are far too broad to investigate the fast component of the relaxation. Since the focus of this work lies purely with the slower, picosecond component of the relaxation, a pulse with of 250 fs is more than adequate. The relaxation between $0 < t \lesssim 0.5$ ps is therefore a measure of the profile of the pulses used.

Fitting to the individual measurements on mono– and few–layer samples, one may extract the phonon relaxation times. These are plotted as a function of the number of layers in Figure 6.4.3(b). Averaging the measurements per layer reveals a monolayer phonon relaxation time of 2.05 ps $\pm$ 0.42 ps. This value rises to 2.81 ps $\pm$ 0.37 ps for bilayer samples and asymptotes to 3.30 ps $\pm$ 0.28 ps for the 6–layer samples.

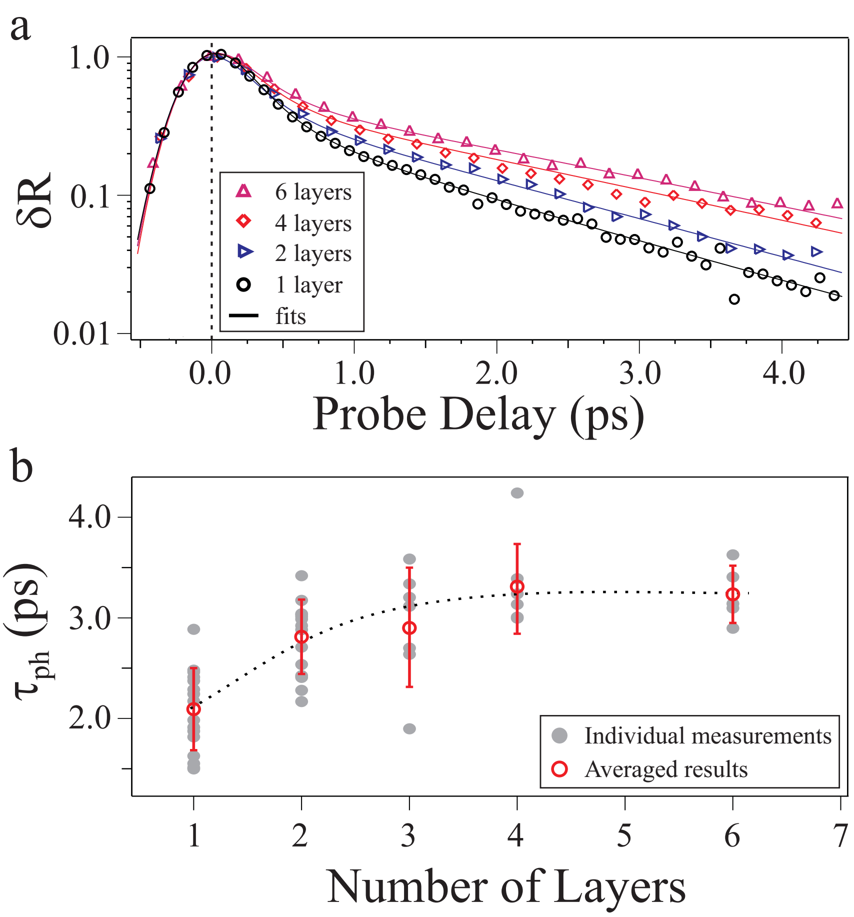

Figure 6.4.3: (a) Differential reflectivity as a function of probe delay for few–layer graphene supported on a glass substrate. The coupled rate equation model is used to fit to the data. (b) Extracted phonon relaxation times, τ_{ph}, for the supported data. Individual measurements are plotted, as well as the averaged results.

The fast and slow relaxation timescales have previously been attributed to electron–electron and electron–phonon interactions respectively[66]. However, it is well known that electron–phonon coupling in graphene features Kohn anomalies[138] that lead to very fast thermalisation with the phonon bath[139]. Indeed, recent calculations[68,140] indicate that thermalisation with phonons is completed within the first $\sim$ 100 fs following photoexcitation. This suggests that the longer timescale, of the order picoseconds, is indeed associated with the relaxation of the thermalised electron–phonon bath through the decay of hot phonons.

6.5 Pump-Probe Spectroscopy for Few-Layer Suspended Graphene

Newson *et. al*[128] postulate that the faster relaxation observed in thinner samples is due to a substrate interaction. Graphene is a soft material which conforms well to the substrate it is placed on. Lui *et. al*[141] recently demonstrated this by comparing the roughness of a graphene flake on a standard SiO_2 substrate to a graphene flake on an atomically flat mica substrate. For the two cases the graphene was observed to possess the same roughness as measured on the bare substrate, indicating that the monolayer flakes conform extremely well to the morphology of the substrate.

As the number of layers increases, so does the rigidity of the sample. For this reason, one may expect the substrate to influence the relaxation dynamics less as the layer number increases. On the other hand, comparing a monolayer to a bilayer sample, one would initially postulate that an increase in the number of layers would in fact increase the relaxation rate. A bilayer will (to a good approximation) absorb twice as much energy as the monolayer, but posesses more than twice the number of phonons (due to the interaction between the two layers, which is not present with a single layer).

To clarify this argument, samples are prepared on pre–defined etched substrates (see Section 2.1.3), resulting in fully suspended mono– and few–layer graphene. Flakes of various thicknesses are found using an optical microscope and characterised via white light reflection contrast on the supported regions of the flakes. This gives a direct comparison to the supported samples measured in Section 6.4 on unetched glass substrates. The samples are confirmed to be suspended via atomic force microscopy, see Figure 6.5.1.

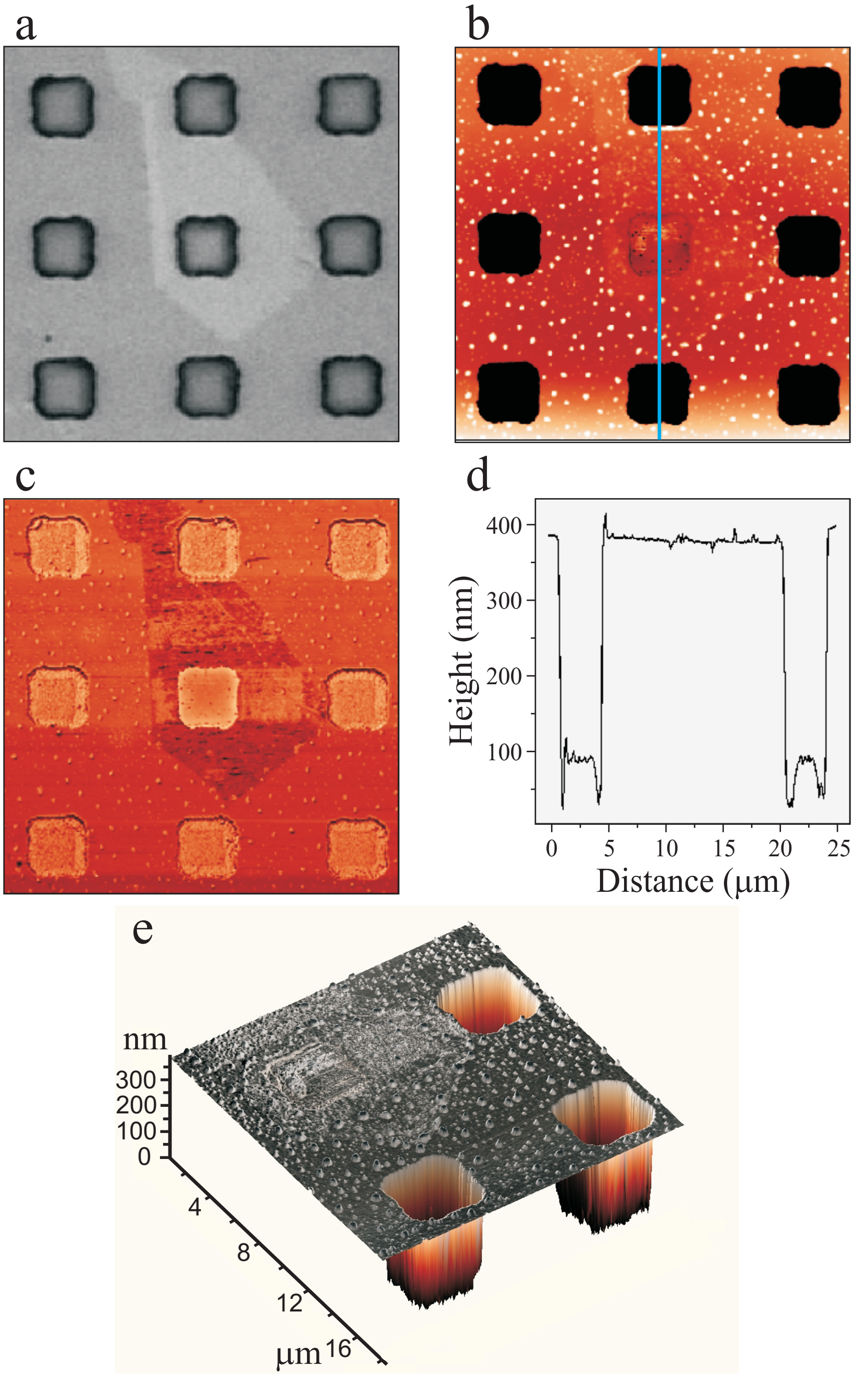

Figure 6.5.1: (a) An optical image (contrast enhanced) of a monolayer sample on the pre–etched substrate. Holes are 3.5 μm $\times$ 3.5 μm and approximately 300 nm in depth. (b) An AFM image of the same region, where the flake covering the centre hole does not touch the base of the hole. The white dots are contaminants on the surface of the substrate. (c) A phase diagram showing the difference between the glass substrate and the graphene. (d) A profile, taken for the blue line in (b), illustrating that the flake is fully suspended. (e) A 3D image of the same flake and substrate.

Monolayers and bilayers are confirmed via Raman spectroscopy. Flakes that appear to span the etched areas are investigated via an atomic force microscope, Figure 6.5.1(b) illustrates such a measurement. The outer holes in the image are all at a depth of approximately 300 nm. The centre hole does not go to this depth. Figure 6.5.1(c) is the phase map from the same measurement, the outline of the flake can clearly be seen due to the difference in the response of the glass substrate and the carbon flake. Figure 6.5.1(d) plots the profile of the blue line shown in Figure 6.5.1(b). The top and bottom holes show a depth of $\sim$ 300 nm and the profile clearly shows how the flake in the centre hole is fully suspended.

With a spot size of ≤ 1.5 μm, one is able to measure solely within the suspended region. To confirm this, samples are found that partially cover an etched hole, Figure 6.5.2. Measuring the portion of the highlighted hole without the flake returns no signal, whereas the region covered by the flake returns the normal signal intensity. This is a clear indication that the resolution of the system is high enough to distinguish between the suspended and supported areas.

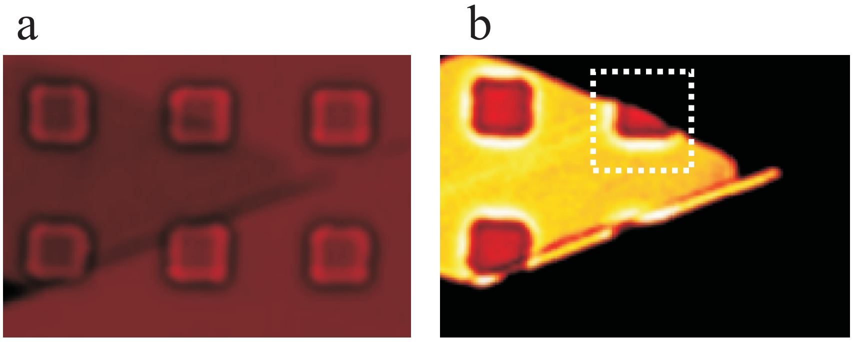

Figure 6.5.2: Images of a suspended flake on an etched glass coverslip. (a) 800 nm transmission image of a 5–layer sample on an etched array of 3.5 μm holes. (b) A nonlinear reflection image of the same region as (a), highlighting the area where the flake partially suspends over a hole. This area is used to confirm the resolution of the experiment.

To ensure the patterned array of holes does not interfere with the pump–probe signal, measurements are taken in and around the etched features, Figure 6.5.3. Scattering from the holes does not result in any competing signal. Since the measurement is the differential reflection of the probe under the influence of the pump, this is not an unexpected result as the dielectric substrate should not possess any nonlinear signal. With the samples characterised, one can now directly compare the decay rates for supported and suspended samples.

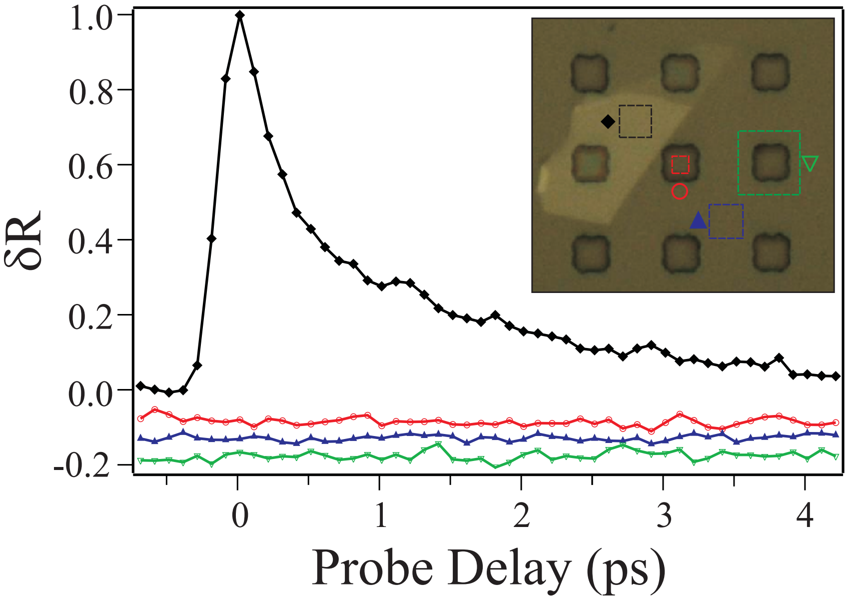

Figure 6.5.3: Differential reflectivity as a function of probe delay for measurements of different regions of the suspended samples. Signal is only measured (black diamonds) when the beams are raster scanned over the flake. When measuring either the substrate (blue triangle), within an etched hole (red circle), or around an etched hole (green triangle), no signal is observed. Traces are offset for clarity.

Measurements are performed in the same experimental conditions as the supported samples in Section 6.4. The differential reflectivity, measured as a function of probe delay for mono– to few–layer graphene, is shown in Figure 6.5.4(a). The faster relaxation for monolayer samples is again observed, with an asymptote being reached at approximately four layers. Fitting to the data with the coupled rate equation model, one is able to extract the phonon relaxation time, τ_{ph}, for the suspended samples. The extracted data is displayed in Figure 6.5.4(b).

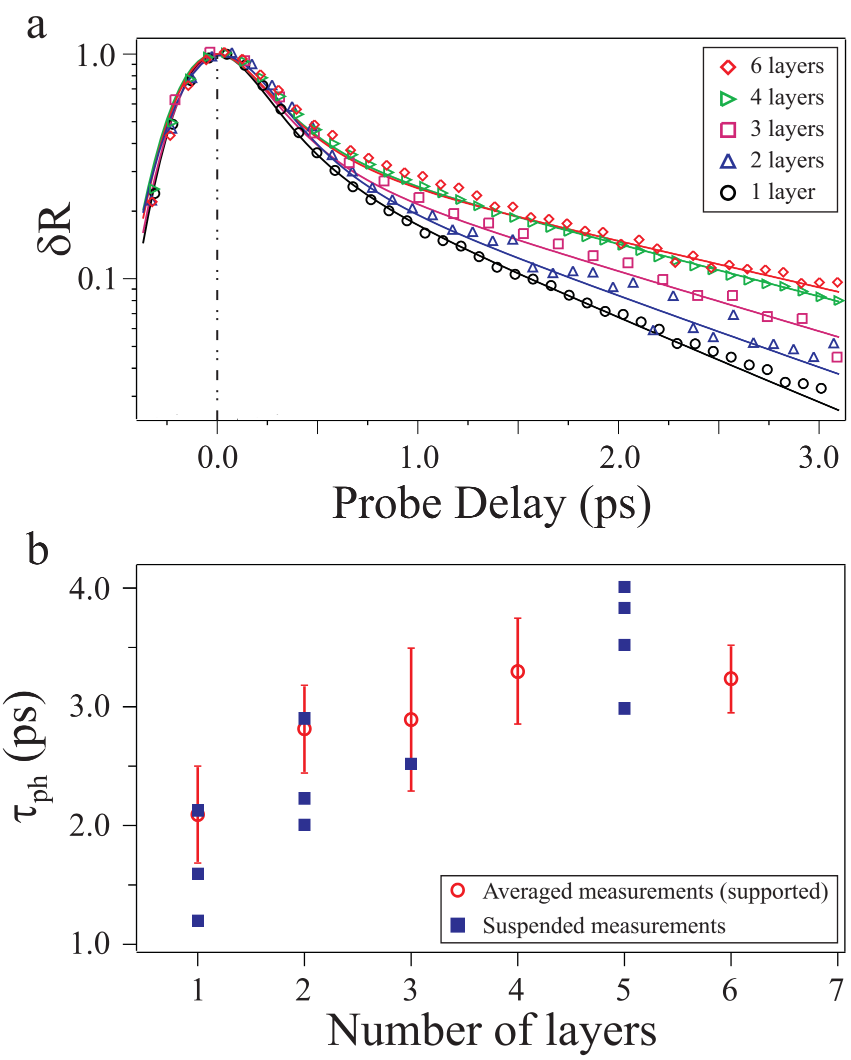

Figure 6.5.4: (a) Differential reflectivity as a function of probe delay for few–layer graphene suspended over pre–defined 3.5 μm square holes on a glass substrate. The coupled rate equation model is used to fit to the data. (b) Extracted phonon relaxation times, τ_{ph}, for the suspended data plotted against the averaged results from the supported measurements.

The suspended samples return a thickness dependence which is in extremely good agreement with the supported measurements. Monolayer samples are observed to relax faster than thicker layers, with an asymptote again being reached at approximately four layers. The data suggests that the relaxation of suspended monolayer graphene may be even faster than that for the supported samples. This strongly suggests that the substrate is not responsible for the faster decay observed in single layer graphene. In turn, this points to an intrinsic origin of the faster decay when comparing mono– to few–layer graphene.

A possible explanation for the faster decay rate lies with out–of–plane (flexural) phonons, which are suppressed in thicker layers. One would expect flexural modes to be present for monolayer graphene supported on a rough glass substrate as the phonon wavelengths in question are comparable to the roughness of the substrate. Out–of–plane modes are suppressed in thicker layers due to interactions between the graphene planes. As the number of layers increases one would expect an asymptote in the observed dynamics as the system begins to resemble a rigid body. The data suggests that this asymptote is already reached at approximately four layers. Introducing strain and/or adsorbates on to the graphene system may provide experimental evidence to confirm the role of flexural phonons, by modifying the coupling to these modes.

6.6 Pump-Probe Measurements on Graphitised Epitaxial SiC

Since epitaxial graphene on silicon carbide is a candidate for future electronic devices, the rate at which these devices can dispose of energy is of vital importance. In recent years, several groups have measured the carrier relaxation processes in graphene using ultrafast techniques[28,59,66,67,123–127]. Due to difficulties in measuring small exfoliated flakes of graphene, all early works focussed mainly on the large area, epitaxial SiC grown samples, while only two studies[74,128] have looked at relaxation dynamics in exfoliated graphene.

Experimental studies have shown a vast range in the slow relaxation timescale: for example, Kampfrath *et al.* observed a 7 ps decay constant when using a pulsed THz frequency probe[139], while Dawlaty *et al.* observed relaxation times $\sim 0.4 - 1.7$ ps when probing with an 800 nm pulse[66]. These apparent discrepancies arise, in part, from the different photon energies in the probe pulses, which change the time dependence of the dynamical signal[72] and the relaxation times which are measured in the experiment[74]. This gives rise to a difficulty in comparing relaxation processes in different types of graphene measured in different experiments. To date, no group has carried out a comparison of ultrafast relaxation processes in exfoliated and epitaxial graphene in the same experiment.

In this section, the ultrafast relaxation dynamics in both exfoliated graphene and graphene epitaxially grown on SiC are compared. Measurements are carried out with identical pump and probe wavelengths, allowing one to directly compare and contrast relaxation processes in these two materials. Since the growth in epitaxial samples tends to be uneven across the substrate, leading to domain formation[59], understanding the transport and optical properties of these layers, especially where there are thickness variations, is of great importance for future graphene–based electronic and opto–electronic devices. The epitaxial graphene sample used is provided by C. Berger, Georgia Institute of Technology. The sample consists of approximately six carbon layers on the $[000\bar{1}]$ (carbon–terminated) face.

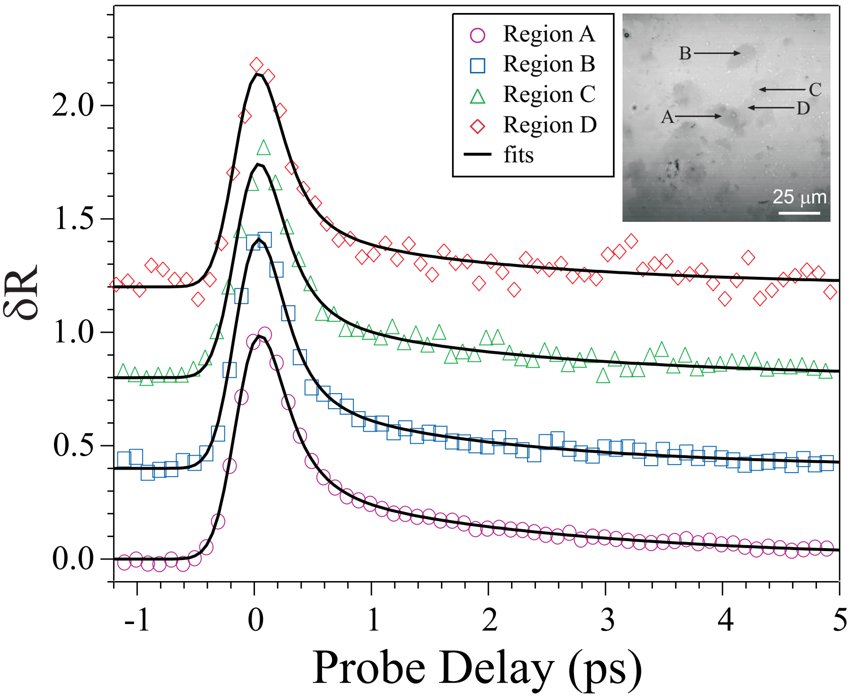

Figure 6.6.1: Normalised differential reflectivity, as a function of probe delay, for various thicknesses of $[000\bar{1}]$ graphitised epitaxial silicon carbide. Traces are offset for clarity. Fits are made to the data using the coupled rate equation model. Inset: Transmission image (830 nm) of the investigated region of the sample with the measured areas identified.

To examine the phonon decay rates for different numbers of carbon layers from epitaxial growth, measurements are taken from different growth regions. The inset of Figure 6.6.1 is a transmission image of the carbon–terminated SiC surface. The 830 nm pump pulse is collected with the transmission PMT to identify the different thickness regions of the sample. Dark regions, corresponding to thicker carbon layers, are compared to the lower intensity, thinner regions.

A portion of the sample showing thin regions is chosen such that the few–layer dynamics can be investigated. For few–layer measurements the overlapped peak pump–probe signal is linear in magnitude and so can be used to calibrate the layer number. Table 6.6.1 shows the peak pump–probe signal for the four regions investigated, along with the estimated optical contrast from the transmission image. The data suggests a value of approximately 15 μV per layer which agrees well with the thickness estimation from the transmission image.

Region	Overlapped ΔT (μV)	$\text{N}_{\text{Optical Contrast}}$
A	129	8
B	68	5
C	46	3
D	32	2

Table 6.6.1: The magnitude of the overlapped pump–probe signal for the regions of graphitised epitaxial silicon carbide investigated. The layer number, N, estimated from the optical contrast, is in good agreement for a signal magnitude of ~ 15 μV per layer.

The optical contrast for each layer is found and corresponds to layer thicknesses of $N = 8$ for region A, $N = 5$ for region B, $N = 3$ for region C and $N = 2$ for region D. The samples are measured in the same experimental conditions as the exfoliated flakes and the normalised differential reflectivity as a function of probe delay is shown in Figure 6.6.1.

Plotting the extracted phonon relaxation times as a function of the number of carbon layers, Figure 6.6.2, a relaxation that appears to be independent of layer number is observed. This suggests the relaxation processes in few– and multilayer regions in epitaxially grown graphene are similar.

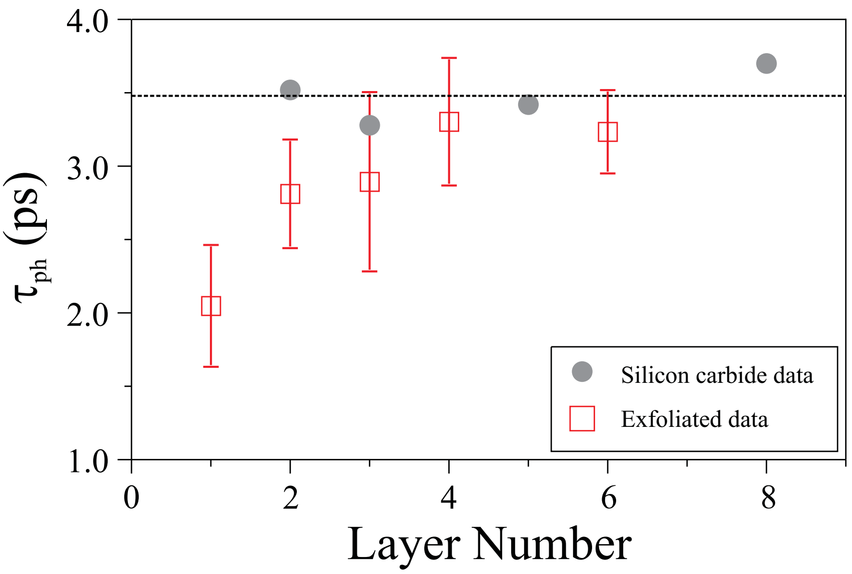

Figure 6.6.2: Extracted phonon relaxation times, as a function of probe delay, for the different regions of graphitised epitaxial silicon carbide. Fits are made using the coupled rate equation model. The dashed line denotes the average relaxation time from the different measurements. For comparison, the extracted relaxation times from the exfoliated samples are also plotted.

This behaviour for epitaxially grown regions of graphene is in contrast to that observed for exfoliated flakes. The question remains as to the origin of this different behaviour between exfoliated and epitaxial graphene. If flexural phonons do provide a significant decay channel for hot phonons, one might expect this to be diminished in epitaxially grown graphene: although the graphene layers are electrically decoupled on the carbon terminated surface, atomic scale forces between the graphene and the substrate may still quench out of plane modes. An alternative explanation for the origin of the different behaviour between exfoliated and epitaxial graphene could lie in the cohesion between the multilayer graphene stacks themselves. While the electronic and optical properties of certain multilayered epitaxial graphene regions can be similar to that of a single graphene layer[38,51,108,142], in other cases the properties are seen to be affected by stacking[143]. Annealing at different temperatures has also been shown to change the stacking order on both the silicon and carbon terminated faces[144].

Comparing the relaxation times for few–layer exfoliated and epitaxial graphene is difficult without a measure of the monolayer on silicon carbide. The enhanced relaxation observed in exfoliated samples is apparent within the bilayer but the strongest effect is clearly observed in monolayers. To conclude whether the relaxation in epitaxial samples follows the enhancement for exfoliated monolayers, a measure of the single layer is required.

6.7 Summary

In summary, time–resolved near–infrared pump–probe spectroscopy is used to measure the ultrafast dynamics of photoexcited charge carriers in monolayer and few–layer graphene. Two timescales are observed in the biexponential decay, a fast component of ~ 100 fs and a slower component $\sim 2-3$ ps. The fast relaxation timescale is attributed to electron–phonon thermalisation, whereas the slower timescale represents a bottleneck in the relaxation process due to the anharmonic decay of the hot phonon population.

Using a simple theoretical model, the decay rates in different graphene flakes are calculated and confirm that the hot phonon decay is faster in monolayer than in few–layer graphene. Comparing the results on supported and suspended flakes it is demonstrated that substrate phonons are not the mechanism for removing energy from the system. One possible origin of the intrinsic mechanism is the enhanced coupling to out–of–plane flexural phonon modes.

The relaxation rate of hot optical phonons on the carbon–terminated face of epitaxial SiC, as a function of the number of layers grown, is also investigated. The rate of relaxation appears to be independent of layer number and agrees well with the results obtained from exfoliated few–layer graphene. Due to the growth of a buffer layer in–between the carbon layers and the silicon carbide bulk, one may postulate that the coupling between the first layer and the buffer is stronger than the interaction between a monolayer of exfoliated graphene and a rough substrate, such as glass or silicon dioxide.

Chapter 7

Conclusions and Further Work

In this thesis, measurements have been performed on graphene and few–layer graphene samples via ultrafast optical techniques. The large third–order nonlinear susceptibility found in graphene in Chapter 3 suggests that this response will be useful for future imaging and characterisation of graphene samples. With a large and almost dispersionless emission over a broad spectral range, graphene is a potential candidate for a standard in third–order nonlinear emission. Four–wave mixing may potentially be used for coupling to a surface plasmon resonance in graphene by tuning the Raman shift between signal and idler frequencies to low enough wavenumbers such that a sweep of the carrier concentration can find a plasmonic resonance.

By investigating the nonlinear response for large area epitaxial graphene on silicon carbide, the use of luminescence imaging enables a high contrast, surface sensitive response to be measured. The extension of the nonlinear imaging technique to epitaxial samples is therefore an obvious step. With tuning of the incident signal and idler wavelengths, a more suitable arrangement of optical band–pass filters can be thought of to further enhance the signal response.

Time–resolved pump–probe spectroscopy demonstrates a bi–exponential decay of photoexcited charge carriers in graphene. The slower relaxation component is attributed to the relaxation of hot optical phonons and shows a significant layer dependence. The intrinsic mechanism for enhanced phonon decay in monolayer graphene is clearly an area for further research. Introducing strain and/or adatoms to the graphene to modify coupling to phonons will provide valuable information regarding the phonon decay channels. By measuring at large carrier concentrations one may attempt to remove the contribution from optical phonons completely, this is discussed in more detail in Section 7.1.

Relaxation of charge carriers in epitaxial graphene on silicon carbide is shown to be independent of the number of layers grown. This has implications for future graphene technology since the rate at which potential devices are able to remove energy will determine device performance. Further investigation, involving a measurement of an epitaxially grown monolayer, will determine whether the enhanced decay observed in monolayer exfoliated graphene is present. Insight into the mechanism behind the enhanced decay may then be found.

Measurements of the modification due to irradiation from ultrafast optical pulses has shown a significant decrease in the third–order nonlinear response of graphene. Comparing pristine and modified flakes one observes what appears to be a shift in the doping level by approximately 500 meV. With ultrafast optics in graphene a popular field, further work in this area is of vital importance to establish the cause of the modification, the direction of the doping and the mechanism behind the effect.

7.1 Pump–Probe Spectroscopy at High Carrier Concentrations

In Chapter 6 the ultrafast relaxation of hot optical phonons in graphene is investigated as a function of the number of graphene layers. The data is analysed with the use of a coupled rate equation model, which calculates the temperature of both the electron and optical phonon population after photoexcitation from an ultrafast pulse. Relaxation of charge carriers is mediated by the rate at which hot optical phonons can decay, and thus the role of the optical phonons is of paramount importance.

This section presents preliminary results concerning the investigation of the role of optical phonons in the relaxation process. By changing the Fermi level in graphene via the application of a solid electrolyte gate, a shift of ~ 0.8 eV from the charge neutrality point can be achieved[60,61,65]. With all available states filled (or empty in the case of hole doping) the decay of charge carriers via carrier–phonon scattering can be stopped. This gives an insight to the other relaxation processes in graphene which are otherwise dominated by optical phonons.

Changes in the carrier concentration can be made with the application of a capacitively–coupled back gate and produce a shift in the Fermi energy, E_{F}. For graphene on an oxidised silicon wafer this corresponds to $E_{\mathrm{F}}(\mathrm{eV}) = 0.031 \cdot \sqrt{\mathrm{V_g}}$, see Section 2.1.4.1. In order to investigate the role of optical phonons in the relaxation of charge carriers in graphene, one must shift the Fermi level to

$$\Delta E_{\mathrm{F}} \geq \left| \frac{\hbar\,\omega_{\mathrm{probe}}}{2} - \hbar\,\Omega_{\mathrm{phonon}} \right| , \tag{7.1.1}$$

as shown in Figure 7.1.1. Here, $\hbar\omega_{\mathrm{probe}}$ and $\hbar\Omega_{\mathrm{phonon}}$ correspond to the probe photon and optical phonon energies respectively. By reaching such extremes in carrier concentration, the relaxation of an electron from the probe energy via an optical phonon can be prohibited since there are no longer any available states to scatter into.

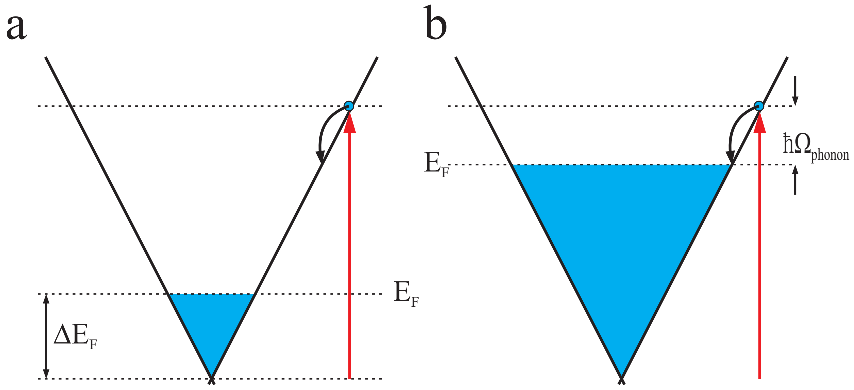

Figure 7.1.1: The electronic dispersion relation at the K point in graphene, shown for electron doping within the conduction band. (a) Low doping levels allow excited electrons to interact with optical phonons due to the availability of states below $\hbar\omega_{\text{probe}}/2$. (b) Increasing the doping level to within $\hbar\Omega_{\text{phonon}}$ of $\hbar\omega_{\text{probe}}/2$ prevents optical phonon scattering due to the lack of available states to scatter into.

Silicon dioxide back gates typically show dielectric breakdown at approximately 100 V, corresponding to a shift in the Fermi level of only 300 meV. To perform measurements in ambient conditions, the application of such high voltages would itself cause hysteresis and measurements would become difficult to interpret. To overcome this, electrolyte gating is employed, as explained in Section 2.1.4.2. Figure 7.1.2 shows a typical measurement of a two–terminal monolayer sample under the application of an electrode voltage. Electrolyte measurements are performed via constant–current measurements with 100 nA passing through the flake. Hysteresis is observed when sweeping due to the low mobility of ions in the electrolyte. This is observed as a shift in the neutrality point for positive and negative sweeps and a broadening of the peak for faster sweep rates. Measurement of a reference electrode shows that the voltage drop is entirely between the flake and the source electrode, with a leakage of the order 10^{-4} V when applying ± 2 V.

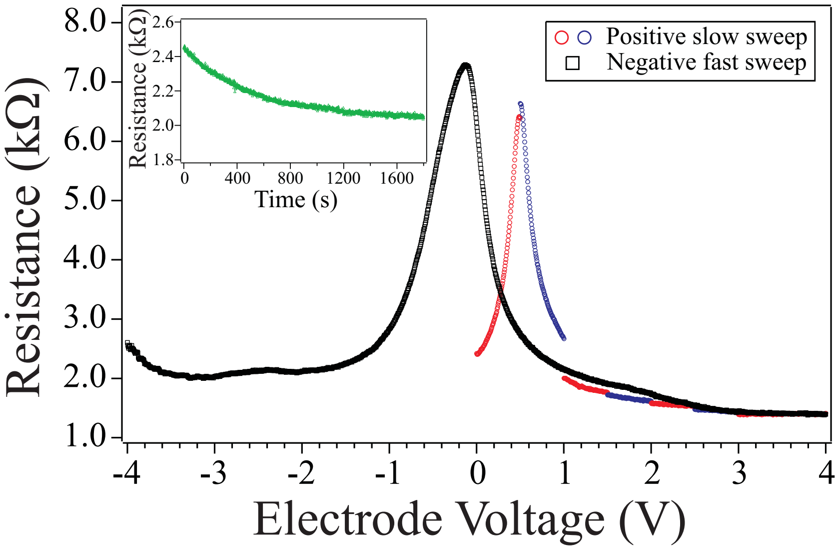

Figure 7.1.2: Resistance as a function of applied electrode voltage for a graphene flake covered with electrolyte. Modulation of the resistance is observed along with a large amount of hysteresis. The black, broader curve is a fast sweep, 4 V/hour, from positive to negative applied voltage. Sweeping slower (red and blue curves) from zero applied voltage to +4 V at 1 V/hour, the peak in resistance is much sharper. Inset: Resistance as a function of time for the positive sweep at an electrode voltage of +1 V. Even with the slow sweep rate the sample requires 30 minutes to reach equilibrium.

Monitoring resistance as a function of time, inset of Figure 7.1.2, shows the timescale on which the electrolyte reaches equilibrium with the applied electrode voltage. Sweeping to +1 V and waiting for the resistance to asymptote, a timescale of the order 30 minutes is observed. Without an independent measurement of the carrier concentration as a function of applied electrode voltage, the absolute shift in E_F is unknown. Hall measurements on a four–terminal device are required.

Preliminary pump–probe measurements are performed on a contacted bilayer sample in the same experimental conditions as Chapter 6. The carrier concentration is modified by quickly sweeping the electrode voltage and waiting for the resistance to equilibriate. Numerous forwards and backwards sweeps are compared and the asymptotic values of resistance are displayed in the inset of Figure 7.1.3. The individual points plot the resistance as a function of applied voltage and show a reproducible curve. The overlapped pump–probe signal at $t = 0$ shows a decrease in magnitude with the application of large voltages. This is repeatable for up and down sweeps and presents a severe difficulty in obtaining the decay dynamics at high carrier concentrations. For the extracted data no dependence has been observed on applied voltage, however, the value of the Fermi shift is unknown.

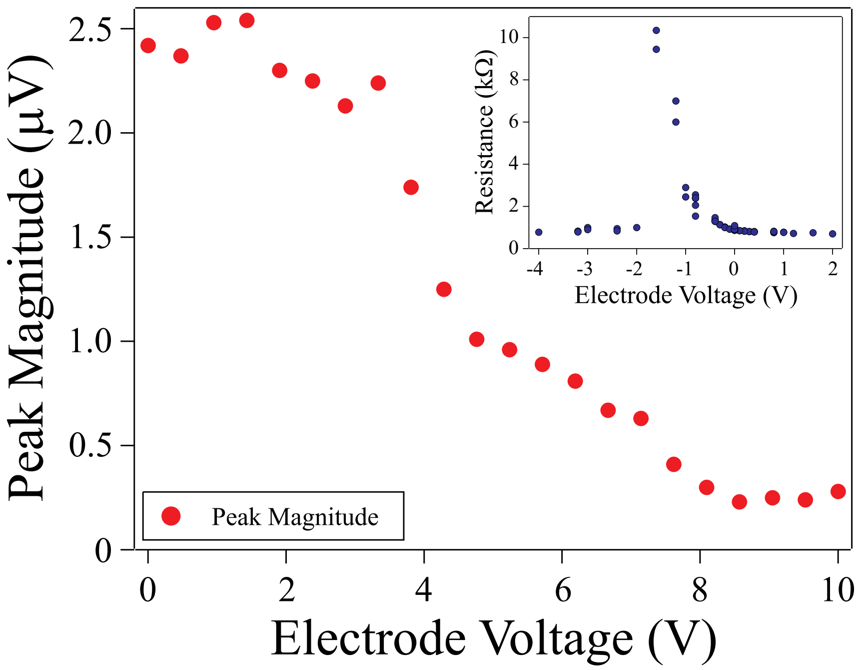

Figure 7.1.3: Magnitude of the overlapped pump–probe signal as a function of applied electrode voltage for a bilayer flake. Due to the low mobility of ions within the electrolyte, the absolute value of the voltage is unknown during sweeping. Overlapped pump–probe signal is observed to decrease under the application of large voltages. Inset: Resistance as a function of electrode voltage for a monolayer sample. Sweeping quickly to a voltage and waiting for the resistance to saturate results in more repeatable data.

Repeating the experiment on a contacted monolayer sample is of importance. The loss of pump induced changes to the probe reflection are potentially caused by the population of a higher band in the bilayer and so would not be present in a measurement of a single layer. To a first approximation one would expect the overlapped signal magnitude to increase as a function of applied voltage due to the further blocking of states at the probe energy. These measurements are currently ongoing.

Appendix A

Subtraction of Bulk SiC Pump–Probe Signal

If one first considers the case where the pump pulse does not exist, the transmission of the probe pulse, T, for an N–layered system is simply a combination of the absorption and reflection losses at each layer,

$$T \ = \ t_{01} \cdot e^{-\alpha_1 L_1} + t_{12} \cdot e^{-\alpha_2 L_2} + ... \cdot t_{(n-1)n} \cdot e^{-\alpha_n L_n} \, , \tag{A.1}$$

where t is the transmission through a given layer, L is the layer thickness and α is the absorption coefficient, Figure A.1. The pump pulse induces a change in the absorbance of the probe and so the transmission of the probe under the influence of the pump, T', is modified,

$$\begin{aligned} T' \ &= (t_{01} + \delta t_{01}) \cdot e^{-(\alpha_1 + \delta\alpha_1) L_1} + (t_{12} + \delta t_{12}) \cdot e^{-(\alpha_2 + \delta\alpha_2) L_2} + ... \\ &\quad (t_{(n-1)n} + \delta t_{(n-1)n}) \cdot e^{-(\alpha_n + \delta\alpha_n) L_n} \, . \end{aligned} \tag{A.2}$$

If one assumes the changes in absorption, $\delta\alpha$, dominate the observed signal, the measured $T' \ - \ T$ may be written

$$\begin{aligned} T' \ - T \ = \ &\left(t_{01} \cdot t_{12} ... \cdot t_{(n-1)n} \cdot e^{-\alpha_1 L_1} \cdot e^{-\alpha_2 L_2} ... \cdot e^{-\alpha_n L_n}\right) \times \left(e^{-\delta\alpha_1} \cdot e^{-\delta\alpha_2} ... \cdot e^{-\delta\alpha_n}\right) \\ &- \left(t_{01} \cdot t_{12} ... \cdot t_{(n-1)n} \cdot e^{-\alpha_1 L_1} \cdot e^{-\alpha_2 L_2} ... \cdot e^{-\alpha_n L_n}\right) \, . \end{aligned} \tag{A.3}$$

By collecting the terms in Equation A.3, one may substitute in for T,

$$T' \ - T \ = T \cdot \left(e^{-\alpha_1 L_1} \cdot e^{-\alpha_2 L_2} ... \cdot e^{-\alpha_n L_n} - 1\right) \, . \tag{A.4}$$

For these weak, nonlinear measurements, the observed changes in transmission are

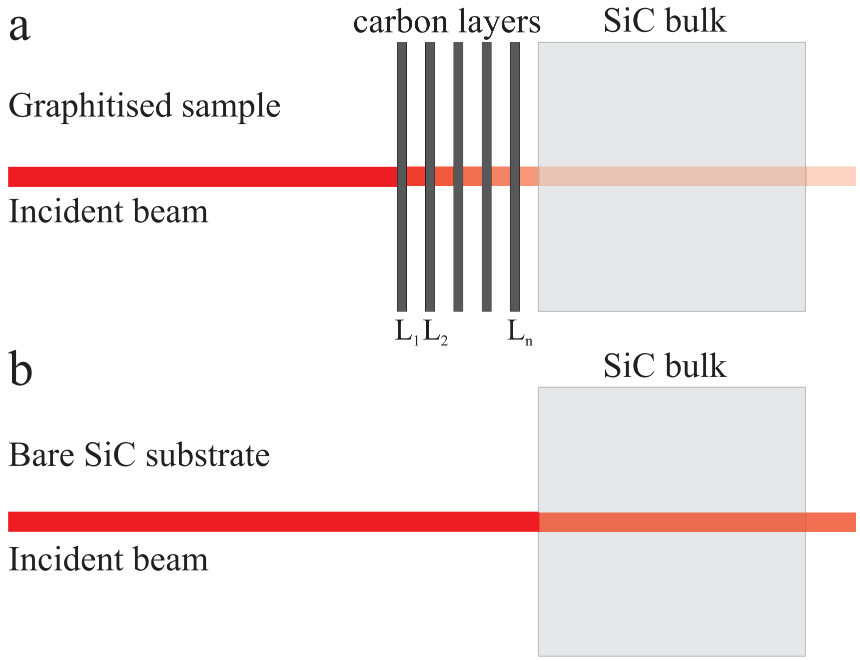

Figure A.1: Schematic of the attenuation of the pulses due to absorption in the carbon layers. (a) Transmission through N carbon layers, lowering the intensity at the SiC bulk. (b) Schematic of a pristine SiC sample which receives the full, unattenuated, laser power.

small. Taking a first order expansion of Equation A.4, and normalising to the reference signal (as in the measurement), one obtains the measured signal, S,

$$\begin{aligned} S &= \frac{T' - T}{T} \\ &\approx -\alpha_1 L_1 - \alpha_2 L_2 ... - \alpha_n L_n - 1\,. \end{aligned} \tag{A.5}$$

The signal from the last layer, the bulk SiC, is the feature to be removed. Importantly, the bulk signal measured in a reference measurement, $\delta\alpha^*_{\text{bulk}}$, is not equal to the bulk signal from a graphitised sample, $\delta\alpha_{\text{bulk}}$ due to losses within the carbon layers. Since the magnitude of the bulk signal is proportional to the intensity of light, Figure A.2, one may write

$$\delta\alpha'_n \cdot I_n = \delta\alpha_n \cdot I'_n\,. \tag{A.6}$$

As each graphene layer absorbs $\sim 2.3\%$ of the incident light, the signal from the carbon layers, S_{graphene}, can be written

$$\mathrm{S_{graphene}} = \mathrm{T'} - \mathrm{T} \cdot 0.977^{\mathrm{N}}\,, \tag{A.7}$$

where N is the number of graphene layers.

White light reflection images of the graphitised sample and a pristine silicon carbide

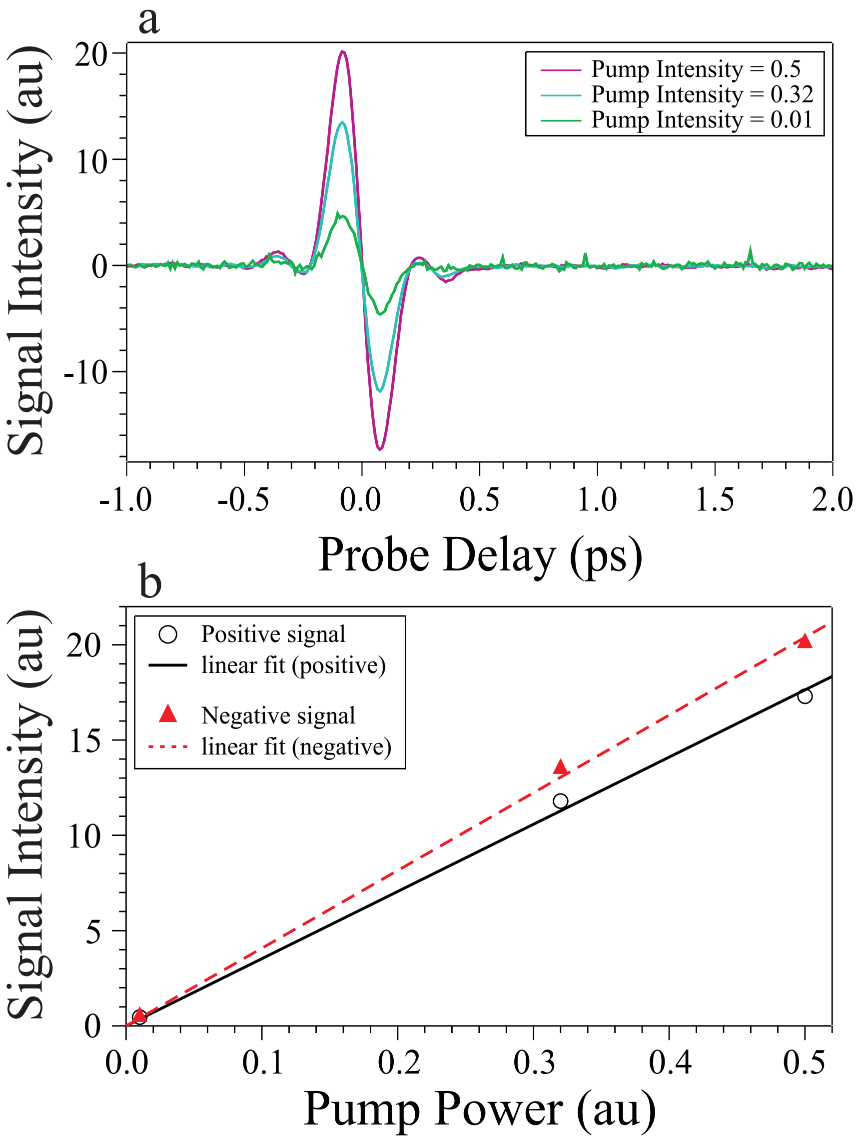

Figure A.2: (a) The ultrafast pump–probe response of pristine 4–H SiC for pump and probe wavelengths of 800 nm. The pump intensity is varied by fifty times. The lowest intensity ($I = 0.01$, green curve) has been multiplied by an order of magnitude for clarity. (b) The extracted peak values for the magnitude of the positive (t ~ -0.1 ps) and negative (t ~ 0.1 ps) features. These show a linear dependence on pump intensity.

substrate are compared to quantify the number of carbon layers present. An optical contrast of $\sim 11\%$ is found, which, normalised over the visible spectrum, corresponds to a carbon coverage of 6 layers, Figure A.3. This is independently verified by the manufacturers via atomic force microscopy, with a reported thickness of $\sim$ 23 Å. The subtraction of the bulk signal is therefore made with a carbon thickness of $N = 6$.

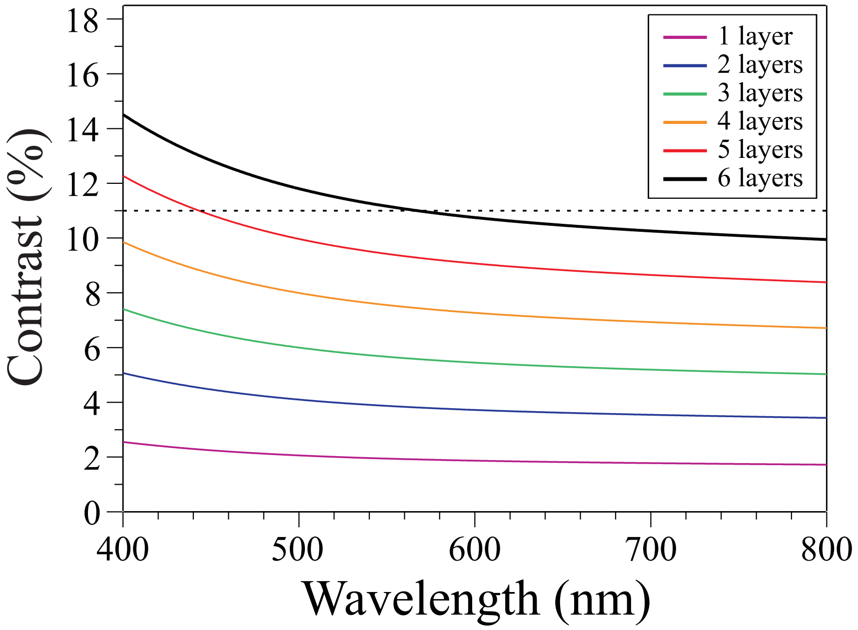

Figure A.3: Modelled reflection contrast, as a function of wavelength, for 1–6 layers of graphite on a silicon carbide substrate using the Fresnel coefficients with plane wave illumination. An observed contrast of $\sim 11\%$ (indicated with the dashed line) suggests a thickness of approximately 6 layers.

References

[1] M.I. Katsnelson. Graphene: carbon in two dimensions. *Materials today*, 10(1-2):20–27, 2007. x, 2

[2] L Wirtz and a Rubio. The phonon dispersion of graphite revisited. *Solid State Communications*, 131(3-4):141–152, July 2004. x, 8, 9

[3] D. Mafra, G. Samsonidze, L. Malard, D. Elias, J. Brant, F. Plentz, E. Alves, and M. Pimenta. Determination of LA and TO phonon dispersion relations of graphene near the Dirac point by double resonance Raman scattering. *Physical Review B*, 76(23):233407, December 2007. xii, 8, 19

[4] Jolanta Borysiuk, Jakub Sotys, Rafal Boek, Jacek Piechota, Stanislaw Krukowski, Wlodzimierz Strupinski, Jacek M. Baranowski, and Roman Stepniewski. Role of structure of C-terminated 4H-SiC(000) surface in growth of graphene layers - transmission electron microscopy and density functional theory studies. *arXiv*, September 2011. xiii, 27

[5] S.A. Mikhailov. Theory of the nonlinear optical frequency mixing effect in graphene. *Physica E: Low-dimensional Systems and Nanostructures*, pages 1–4, October 2010. xviii, 59, 60, 66, 67, 68

[6] S. Logothetidis, J. Petalas, H. Polatoglou, and D. Fuchs. Origin and temperature dependence of the first direct gap of diamond. *Physical Review B*, 46(8):4483, August 1992. 1

[7] A. Pisanty. The electronic structure of graphite: A chemist's introduction to band theory. *Journal of Chemical Education*, 68(10):804, 1991. 1

[8] P. R. Wallace. The Band Theory of Graphite. *Physical Review*, 71(9):622–634, May 1947. 1, 3

[9] R. E. Peierls. Quelques proprietes typiques des corpses solides. *Ann. Inst. H. Poincare*, 5:177, 1935. 1

[10] L. D. Landau. Zur Theorie der phasenumwandlungen II. *Phys. Z. Sowjetunion*, 11:26, 1937. 1

[11] E Thostenson. Advances in the science and technology of carbon nanotubes and their composites: a review. *Composites Science and Technology*, 61(13):1899, October 2001. 2

[12] K S Novoselov, A K Geim, S V Morozov, D Jiang, Y Zhang, S V Dubonos, I V Grigorieva, and A A Firsov. Electric field effect in atomically thin carbon films. *Science*, 306(5696):666, October 2004. 2, 23

[13] K S Novoselov, A K Geim, S V Morozov, D Jiang, M I Katsnelson, I V Grigorieva, S V Dubonos, and A A Firsov. Two-dimensional gas of massless Dirac fermions in graphene. *Nature*, 438(7065):197–200, November 2005. 2

[14] Tsuneya Ando, Yisong Zheng, and Hidekatsu Suzuura. Dynamical Conductivity and Zero-Mode Anomaly in Honeycomb Lattices. *Journal of the Physics Society Japan*, 71(5):1318–1324, May 2002. 2, 9

[15] A. Kuzmenko, E. van Heumen, D. van der Marel, and F. Carbone. Universal Optical Conductance of Graphite. *Physical Review Letters*, 100(11):117401, March 2008.

[16] K.F. Mak, M.Y. Sfeir, Y. Wu, C.H. Lui, J.A. Misewich, and T.F. Heinz. Measurement of the optical conductivity of graphene. *Physical Review Letters*, 101(19):196405, 2008. 2, 9

[17] G Kresse, J Furthmüller, and J Hafner. Ab initio Force Constant Approach to Phonon Dispersion Relations of Diamond and Graphite. *Europhysics Letters (EPL)*, 32(9):729–734, December 1995. 8

[18] Yoshiyuki Miyamoto, Marvin Cohen, and Steven Louie. Ab initio calculation of phonon spectra for graphite, BN, and BC2N sheets. *Physical Review B*, 52(20):14971–14975, November 1995.

[19] P Pavone, R Bauer, K Karch, O. Schütt, S Vent, W Windl, D Strauch, S Baroni, and S. de Gironcoli. Ab initio phonon calculations in solids. *Physica B: Condensed Matter*, 219-220:439–441, April 1996.

[20] Daniel Sánchez-Portal, Emilio Artacho, José Soler, Angel Rubio, and Pablo Ordejón. Ab initio structural, elastic, and vibrational properties of carbon nanotubes. *Physical Review B*, 59(19):12678, May 1999.

[21] Ludger Wirtz, Angel Rubio, Raul de la Concha, and Annick Loiseau. Ab initio calculations of the lattice dynamics of boron nitride nanotubes. *Physical Review B*, 68(4):045425, July 2003.

[22] O. Dubay and G. Kresse. Accurate density functional calculations for the phonon dispersion relations of graphite layer and carbon nanotubes. *Physical Review B*, 67(3):035401, January 2003.

[23] L. Vitali, M. Schneider, K. Kern, L. Wirtz, and A. Rubio. Phonon and plasmon excitation in inelastic electron tunneling spectroscopy of graphite. *Physical Review B*, 69(12):121414, March 2004.

[24] H. Yanagisawa, T. Tanaka, Y. Ishida, M. Matsue, E. Rokuta, S. Otani, and C. Oshima. Analysis of phonons in graphene sheets by means of HREELS measurement andab initio calculation. *Surface and Interface Analysis*, 37(2):133–136, February 2005. 8

[25] Takashi Aizawa, Ryutaro Souda, Yoshio Ishizawa, Hideki Hirano, Taro Yamada, Ken-ichi Tanaka, and Chuhei Oshima. Phonon dispersion in monolayer graphite formed on Ni(111) and Ni(001). *Surface Science*, 237(1-3):194–202, November 1990. 8

[26] Susanne Siebentritt, Roland Pues, Karl-heinz Rieder, and Alexander M Shikin. Surface phonon dispersion in graphite and in a lanthanum graphite intercalation compound. *Physical Review B*, 55(12):7927–7934, March 1997.

[27] J. Maultzsch, S. Reich, C. Thomsen, H. Requardt, and P. Ordejón. Phonon Dispersion in Graphite. *Physical Review Letters*, 92(7):075501, February 2004. 8

[28] Haining Wang, Jared H. Strait, Paul A. George, Shriram Shivaraman, Virgil B. Shields, Mvs Chandrashekhar, Jeonghyun Hwang, Farhan Rana, Michael G. Spencer, Carlos S. Ruiz-Vargas, and Jiwoong Park. Ultrafast relaxation dynamics of hot optical phonons in graphene. *Applied Physics Letters*, 96(8):081917, 2010. 8, 85, 89, 90, 95, 103

[29] T. H. Maiman. Stimulated Optical Radiation in Ruby. *Nature*, 187(4736):493, August 1960. 9

[30] D. S. L. Abergel, A. Russell, and Vladimir I. Falko. Visibility of graphene flakes on a dielectric substrate. *Applied Physics Letters*, 91(6):063125, 2007. 11, 64

[31] P. Blake, EW Hill, A.H.C. Neto, KS Novoselov, D. Jiang, R. Yang, TJ Booth, and AK Geim. Making graphene visible. *Applied Physics Letters*, 91:063124, 2007. 64

[32] C. Casiraghi, A. Hartschuh, E. Lidorikis, H. Qian, H. Harutyunyan, T. Gokus, KS Novoselov, and AC Ferrari. Rayleigh imaging of graphene and graphene layers. *Nano Letters*, 7(9):2711–2717, 2007.

[33] S Roddaro, P Pingue, V Piazza, V Pellegrini, and F Beltram. The optical visibility of graphene: interference colors of ultrathin graphite on SiO(2). *Nano letters*, 7(9):2707, September 2007. 16

[34] Guoquan Teo, Haomin Wang, Yihong Wu, Zaibing Guo, Jun Zhang, Zhenhua Ni, and Zexiang Shen. Visibility study of graphene multilayer structures. *Journal of Applied Physics*, 103(12):124302, June 2008. 13

[35] M. Friedemann, K. Pierz, R. Stosch, and F. J. Ahlers. Graphene on gallium arsenide: Engineering the visibility. *Applied Physics Letters*, 95(10):102103, 2009.

[36] Victor Yu and Michael Hilke. Large contrast enhancement of graphene monolayers by angle detection. *Applied Physics Letters*, 95(15):151904, 2009. 11

[37] E. D. Palik, editor. *Handbook of Optical Constants of Solids*. Academic Press, New York, 1991. 13

[38] Kin Fai Mak, Matthew Y Sfeir, James a Misewich, and Tony F Heinz. The evolution of electronic structure in few-layer graphene revealed by optical spectroscopy. *Proceedings of the National Academy of Sciences of the United States of America*, 107(34):14999, August 2010. 13, 106

[39] E. McCann, D. S.L. Abergel, and V. I. Fal'ko. The low energy electronic band structure of bilayer graphene. *The European Physical Journal Special Topics*, 148(1):91–103, September 2007. 19

[40] A. C. Ferrari, J. C. Meyer, V. Scardaci, C. Casiraghi, Michele Lazzeri, Francesco Mauri, S. Piscanec, Da Jiang, K. S. Novoselov, S. Roth, and A. K. Geim. Raman Spectrum of Graphene and Graphene Layers. *Physical Review Letters*, 97(18):187401, October 2006. 20

[41] Chunxiao Cong, Ting Yu, Kentaro Sato, Jingzhi Shang, Riichiro Saito, Gene F. Dresselhaus, and Mildred S Dresselhaus. Raman Characterization of ABA- and ABC- Stacked Trilayer Graphene. *ACS Nano*, 5(11):8760, October 2011. 20

[42] D C Elias, R R Nair, T M G Mohiuddin, S V Morozov, P Blake, M P Halsall, A C Ferrari, D W Boukhvalov, M I Katsnelson, A K Geim, and K S Novoselov. Control of graphene's properties by reversible hydrogenation: evidence for graphane. *Science*, 323(5914):610–613, January 2009. 25, 70

[43] Jeremy T Robinson, James S Burgess, Chad E Junkermeier, Stefan C Badescu, Thomas L Reinecke, F Keith Perkins, Maxim K Zalalutdniov, Jeffrey W Baldwin, James C Culbertson, Paul E Sheehan, and Eric S Snow. Properties of fluorinated graphene films. *Nano letters*, 10(8):3001, August 2010. 25

[44] Seung Jin Chae, Fethullah Günes, Ki Kang Kim, Eun Sung Kim, Gang Hee Han, Soo Min Kim, Hyeon-Jin Shin, Seon-Mi Yoon, Jae-Young Choi, Min Ho Park, Cheol Woong Yang, Didier Pribat, and Young Hee Lee. Synthesis of Large-Area Graphene Layers on Poly-Nickel Substrate by Chemical Vapor Deposition: Wrinkle Formation. *Advanced Materials*, 21(22):2328, June 2009. 26

[45] Alfonso Reina, Xiaoting Jia, John Ho, Daniel Nezich, Hyungbin Son, Vladimir Bulovic, Mildred S Dresselhaus, and Jing Kong. Large area, few-layer graphene films on arbitrary substrates by chemical vapor deposition. *Nano letters*, 9(1):30, January 2009.

[46] L.G. De Arco and Akshay Kumar. Synthesis, Transfer, and Devices of Single- and Few-Layer Graphene by Chemical Vapor Deposition. *IEEE Transactions on Nanotechnology*, 8(2):135, March 2009.

[47] A. J. Pollard, R. R. Nair, S. N. Sabki, C. R. Staddon, L. M. A. Perdigao, C. H. Hsu, J. M. Garfitt, S. Gangopadhyay, H. F. Gleeson, A. K. Geim, and P. H. Beton. Formation of Monolayer Graphene by Annealing Sacrificial Nickel Thin Films. *The Journal of Physical Chemistry C*, 113(38):16565, September 2009.

[48] Wei Liu, Choong-Heui Chung, Cong-Qin Miao, Yan-Jie Wang, Bi-Yun Li, Ling-Yan Ruan, Ketan Patel, Young-Ju Park, Jason Woo, and Ya-Hong Xie. Chemical vapor deposition of large area few layer graphene on Si catalyzed with nickel films. *Thin Solid Films*, 518(6):S128, January 2010. 26

[49] Xuesong Li, Weiwei Cai, Jinho An, Seyoung Kim, Junghyo Nah, Dongxing Yang, Richard Piner, Aruna Velamakanni, Inhwa Jung, Emanuel Tutuc, Sanjay K Banerjee, Luigi Colombo, and Rodney S Ruoff. Large-area synthesis of high-quality and uniform graphene films on copper foils. *Science*, 324(5932):1312–1314, 2009. 26

[50] Sukang Bae, Hyeongkeun Kim, Youngbin Lee, Xiangfan Xu, Jae-Sung Park, Yi Zheng, Jayakumar Balakrishnan, Tian Lei, Hye Ri Kim, Young Il Song, Young-Jin Kim, Kwang S Kim, Barbaros Ozyilmaz, Jong-hyun Ahn, Byung Hee Hong, and Sumio Iijima. Roll-to-roll production of 30-inch graphene films for transparent electrodes. *Nature nanotechnology*, 5(8):574, August 2010. 26

[51] Claire Berger, Zhimin Song, Xuebin Li, Xiaosong Wu, Nate Brown, Cécile Naud, Didier Mayou, Tianbo Li, Joanna Hass, Alexei N Marchenkov, Edward H Conrad, Phillip N First, and Walt a de Heer. Electronic confinement and coherence in patterned epitaxial graphene. *Science (New York, N.Y.)*, 312(5777):1191, May 2006. 26, 106

[52] Gong Gu, Shu Nie, R. M. Feenstra, R. P. Devaty, W. J. Choyke, Winston K. Chan, and Michael G. Kane. Field effect in epitaxial graphene on a silicon carbide substrate. *Applied Physics Letters*, 90(25):253507, 2007.

[53] W De Heer, C Berger, X Wu, P First, E Conrad, X Li, T Li, M Sprinkle, J Hass, and M Sadowski. Epitaxial graphene. *Solid State Communications*, 143(1-2):92, July 2007. 26, 75

[54] Claire Berger, Zhimin Song, Xuebin Li, Xiaosong Wu, Nate Brown, Duncan Maud, Cécile Naud, and Walt a. de Heer. Magnetotransport in high mobility epitaxial graphene. *physica status solidi (a)*, 204(6):1746, June 2007. 26

[55] Xu Du, Ivan Skachko, Anthony Barker, and Eva Y Andrei. Approaching ballistic transport in suspended graphene. *Nature nanotechnology*, 3(8):491, August 2008. 26

[56] J. L. Tedesco, B. L. VanMil, R. L. Myers-Ward, J. M. McCrate, S. a. Kitt, P. M. Campbell, G. G. Jernigan, J. C. Culbertson, C. R. Eddy, and D. K. Gaskill. Hall effect mobility of epitaxial graphene grown on silicon carbide. *Applied Physics Letters*, 95(12):122102, 2009. 26

[57] F. Varchon, R. Feng, J. Hass, X. Li, B. Nguyen, C. Naud, P. Mallet, J.-Y. Veuillen, C. Berger, E. Conrad, and L. Magaud. Electronic Structure of Epitaxial Graphene Layers on SiC: Effect of the Substrate. *Physical Review Letters*, 99(12):3–6, September 2007. 26

[58] D. S. L. Abergel, V Apalkov, J Berashevich, K Ziegler, and Tapash Chakraborty. Properties of graphene: a theoretical perspective. *Advances in Physics*, 59(4):261–482, July 2010. 26

[59] Libai Huang, Gregory V Hartland, Li-Qiang Chu, Luxmi, Randall M Feenstra, Chuanxin Lian, Kristof Tahy, and Huili Xing. Ultrafast transient absorption microscopy studies of carrier dynamics in epitaxial graphene. *Nano letters*, 10(4):1308–13, April 2010. 26, 85, 103

[60] Dmitri Efetov and Philip Kim. Controlling Electron-Phonon Interactions in Graphene at Ultrahigh Carrier Densities. *Physical Review Letters*, 105(25):256805, December 2010. 38, 39, 109

[61] A. Pachoud, M. Jaiswal, P. K. Ang, K. P. Loh, and B. Özyilmaz. Graphene transport at high carrier densities using a polymer electrolyte gate. *Europhysics Letters*, 92(2):27001, October 2010. 109

[62] J. Ye, M. F. Craciun, M. Koshino, S. Russo, S. Inoue, H. Yuan, H. Shimotani, a. F. Morpurgo, and Y. Iwasa. Accessing the transport properties of graphene and its multilayers at high carrier density. *Proceedings of the National Academy of Sciences*, pages 1–5, July 2011.

[63] Dmitri Efetov, Patrick Maher, Simas Glinskis, and Philip Kim. Multiband transport in bilayer graphene at high carrier densities. *Physical Review B*, 84(16):161412, October 2011.

[64] Adarsh Sagar, Kannan Balasubramanian, Marko Burghard, Klaus Kern, and Roman Sordan. Polymer-electrolyte gated graphene transistors for analog and digital phase detection. *Applied Physics Letters*, 99(4):043307, 2011. 38

[65] A. Das, S. Pisana, B. Chakraborty, S. Piscanec, S. K. Saha, U. V. Waghmare, K S Novoselov, H R Krishnamurthy, A. K. Geim, A. C. Ferrari, and A. K. Sood. Monitoring dopants by Raman scattering in an electrochemically top-gated graphene transistor. *Nature nanotechnology*, 3(4):210, April 2008. 39, 81, 83, 109

[66] Jahan M. Dawlaty, Shriram Shivaraman, Mvs Chandrashekhar, Farhan Rana, and Michael G. Spencer. Measurement of Ultrafast Carrier Dynamics in Epitaxial Graphene. *Applied Physics Letters*, 92(4):042116, 2007. 45, 85, 97, 103

[67] Paul A. George, Jared Strait, Jahan Dawlaty, Shriram Shivaraman, Mvs Chandrashekhar, Farhan Rana, and Michael G. Spencer. Ultrafast Optical-Pump Terahertz-Probe Spectroscopy of the Carrier Relaxation and Recombination Dynamics in Epitaxial Graphene. *Nano letters*, 8(12):4248–4251, November 2008. 45, 85, 103

[68] Markus Breusing, Claus Ropers, and Thomas Elsaesser. Ultrafast Carrier Dynamics in Graphite. *Physical Review Letters*, 102(8):086809, 2009. 45, 97

[69] Dong Sun, Zong-Kwei Wu, Charles Divin, Xuebin Li, Claire Berger, Walt a. De Heer, Phillip N. First, and Theodore B. Norris. Ultrafast dynamics and interlayer thermal coupling of hot carriers in epitaxial graphene. *Physica Status Solidi (C)*, 6(2):470–473, February 2009.

[70] Farhan Rana, Paul George, Jared Strait, Jahan Dawlaty, Shriram Shivaraman, Mvs Chandrashekhar, and Michael Spencer. Carrier recombination and generation rates for intravalley and intervalley phonon scattering in graphene. *Physical Review B*, 79(11):115447, March 2009. 89, 90

[71] Xingquan Zou, Da Zhan, Xiaofeng Fan, Dongwook Lee, Saritha K. Nair, Li Sun, Zhenhua Ni, Zhiqiang Luo, Lei Liu, Ting Yu, Zexiang Shen, and Elbert E. M. Chia. Ultrafast carrier dynamics in pristine and FeCl[sub 3]-intercalated bilayer graphene. *Applied Physics Letters*, 97(14):141910, 2010. 85

[72] Chun Lui, Kin Mak, Jie Shan, and Tony Heinz. Ultrafast Photoluminescence from Graphene. *Physical Review Letters*, 105(12):127404, September 2010. 77, 103

[73] M. Breusing, S. Kuehn, T. Winzer, E. Malić, F. Milde, N. Severin, J. Rabe, C. Ropers, A. Knorr, and T. Elsaesser. Ultrafast nonequilibrium carrier dynamics in a single graphene layer. *Physical Review B*, 83(15):153410, April 2011. 89

[74] P. J. Hale, S. M. Hornett, J. Moger, D. W. Horsell, and E. Hendry. Hot phonon decay in supported and suspended exfoliated graphene. *Physical Review B*, 83:121404(R), March 2011. 103

[75] Jingzhi Shang, Ting Yu, Jianyi Lin, and Gagik G Gurzadyan. Ultrafast electron-optical phonon scattering and quasiparticle lifetime in CVD-grown graphene. *ACS nano*, 5(4):3278–3283, April 2011.

[76] S. Winnerl, M. Orlita, P. Plochocka, P. Kossacki, M. Potemski, T. Winzer, E. Malic, a. Knorr, M. Sprinkle, C. Berger, W. de Heer, H. Schneider, and M. Helm. Carrier Relaxation in Epitaxial Graphene Photoexcited Near the Dirac Point. *Physical Review Letters*, 107(23):2–6, November 2011. 45

[77] S. A. Mikhailov. Non-linear electromagnetic response of graphene. *Europhysics Letters (EPL)*, 79(2):27002, July 2007. 52, 69

[78] S. Tatsuura, M. Furuki, Y. Sato, I. Iwasa, M. Tian, and H. Mitsu. Semiconductor Carbon Nanotubes as Ultrafast Switching Materials for Optical Telecommunications. *Advanced Materials*, 15(6):534, March 2003. 52, 63

[79] J-S. Lauret, C. Voisin, G. Cassabois, J. Tignon, C. Delalande, Ph. Roussignol, O. Jost, and L. Capes. Third-order optical nonlinearities of carbon nanotubes in the femtosecond regime. *Applied Physics Letters*, 85(16):3572, 2004.

[80] C. Stanciu, R. Ehlich, V. Petrov, O. Steinkellner, J. Herrmann, I. V. Hertel, G. Ya. Slepyan, a. a. Khrutchinski, S. a. Maksimenko, F. Rotermund, E. E. B. Campbell, and F. Rohmund. Experimental and theoretical study of third-order harmonic generation in carbon nanotubes. *Applied Physics Letters*, 81(21):4064, 2002. 59

[81] JaeTae Seo, SeongMin Ma, Qiguang Yang, Linwood Creekmore, Russell Battle, Makaye Tabibi, Herbert Brown, Ashley Jackson, Tifney Skyles, Bagher Tabibi, SungSoo Jung, and Min Namkung. Third-order Optical Nonlinearities of Single-wall Carbon Nanotubes for Nonlinear Transmission Limiting Application. *Journal of Physics: Conference Series*, 38:37, May 2006. 62, 63

[82] Vl.A. Margulis, O.V. Boyarkina, and E.A. Gaiduk. Non-degenerate optical four-wave mixing in single-walled carbon nanotubes. *Optics Communications*, 249:339, May 2005. 52, 56, 63, 64

[83] Peixian Ye and Y. Shen. Transient four-wave mixing and coherent transient optical phenomena. *Physical Review A*, 25(4):2183–2199, April 1982. 53

[84] R. W. Boyd. *Nonlinear Optics*. Academic Press, 1992. 55, 56, 61

[85] Robert Adair, L. L. Chase, and Stephen a. Payne. Nonlinear refractive-index measurements of glasses using three-wave frequency mixing. *Journal of the Optical Society of America B*, 4(6):875, June 1987. 56, 65

[86] Carlo Sirtori, Federico Capasso, Deborah Sivco, and Alfred Cho. Giant, triply resonant, third-order nonlinear susceptibility χ_{3ω}^{(3)} in coupled quantum wells. *Physical Review Letters*, 68(7):1010, February 1992. 59

[87] Evangelia Xenogiannopoulou, Kostas Iliopoulos, Stelios Couris, Tanya Karakouz, Alexander Vaskevich, and Israel Rubinstein. Third-Order Nonlinear Optical Response of Gold-Island Films. *Advanced Functional Materials*, 18(8):1281, April 2008. 61, 62

[88] David D. Smith, Youngkwon Yoon, Robert W. Boyd, Joseph K. Campbell, Lane a. Baker, Richard M. Crooks, and Michael George. z-scan measurement of the nonlinear absorption of a thin gold film. *Journal of Applied Physics*, 86(11):6200, 1999. 61, 62

[89] Hyunmin Kim, David K Taggart, Chengxiang Xiang, Reginald M Penner, and Eric Olaf Potma. Spatial control of coherent anti-stokes emission with height-modulated gold zig-zag nanowires. *Nano letters*, 8(8):2373, August 2008. 62

[90] Vl.A. Margulis and T.a. Sizikova. Theoretical study of third-order nonlinear optical response of semiconductor carbon nanotubes. *Physica B: Condensed Matter*, 245(2):173, March 1998. 63

[91] Vl A Margulis. Theoretical estimations of third-order optical nonlinearities for semiconductor carbon nanotubes. *Journal of Physics: Condensed Matter*, 11(15):3065, April 1999. 63

[92] P. E. Gaskell, H. S. Skulason, C. Rodenchuk, and T. Szkopek. Counting graphene layers on glass via optical reflection microscopy. *Applied Physics Letters*, 94(14):143101, 2009. 64, 65

[93] Hyunmin Kim, Tatyana Sheps, Philip G Collins, and Eric O Potma. Nonlinear optical imaging of individual carbon nanotubes with four-wave-mixing microscopy. *Nano letters*, 9(8):2991, August 2009. 65

[94] Zheshen Zhang and Paul L Voss. A quantum-dynamical theory for nonlinear optical interactions in graphene. *arXiv*, page 1106.4838, June 2011. 68, 69

[95] Kenichi Ishikawa. Nonlinear optical response of graphene in time domain. *Physical Review B*, 82(20):201402, November 2010.

[96] Zheshen Zhang and Paul L Voss. Full-band quantum-dynamical theory of saturation and four-wave mixing in graphene. *Optics Letters*, 36(23):4569, November 2011. 69

[97] F. Withers, M. Dubois, and A. Savchenko. Electron properties of fluorinated single-layer graphene transistors. *Physical Review B*, 82(7):073403, August 2010. 70

[98] S.-H. Cheng, K. Zou, F. Okino, H. R. Gutierrez, A. Gupta, N. Shen, P. C. Eklund, J. O. Sofo, and J. Zhu. Reversible fluorination of graphene: Evidence of a two-dimensional wide bandgap semiconductor. *Physical Review B*, 81(20):205435, May 2010. 70

[99] Vitor Pereira and A. Castro Neto. Strain Engineering of Graphenes Electronic Structure. *Physical Review Letters*, 103(4):046801, July 2009. 70

[100] Seon-Myeong Choi, Seung-Hoon Jhi, and Young-Woo Son. Controlling energy gap of bilayer graphene by strain. *Nano letters*, 10(9):3486, September 2010. 70

[101] Young-Woo Son, Marvin L. Cohen, and Steven G. Louie. Energy Gaps in Graphene Nanoribbons. *Physical Review Letters*, 97(21):216803, November 2006. 70

[102] Melinda Han, Barbaros Özyilmaz, Yuanbo Zhang, and Philip Kim. Energy Band-Gap Engineering of Graphene Nanoribbons. *Physical Review Letters*, 98(20):206805, May 2007. 70

[103] T Gokus, R R Nair, A Bonetti, M Böhmler, A Lombardo, K S Novoselov, a K Geim, a C Ferrari, and A Hartschuh. Making graphene luminescent by oxygen plasma treatment. *ACS nano*, 3(12):3963, December 2009. 72

[104] Goki Eda, Yun-Yue Lin, Cecilia Mattevi, Hisato Yamaguchi, Hsin-An Chen, I-Sheng Chen, Chun-Wei Chen, and Manish Chhowalla. Blue photoluminescence from chemically derived graphene oxide. *Advanced Materials*, 22(4):505, January 2010.

[105] Wei-Tao Liu, S. Wu, P. Schuck, M. Salmeron, Y. Shen, and F. Wang. Nonlinear broadband photoluminescence of graphene induced by femtosecond laser irradiation. *Physical Review B*, 82(8):081408(R), August 2010. 72

[106] Jaemyung Kim, Laura J Cote, Franklin Kim, and Jiaxing Huang. Visualizing graphene based sheets by fluorescence quenching microscopy. *Journal of the American Chemical Society*, 132(1):260, January 2010.

[107] Tran Viet Cuong, Viet Hung Pham, Eun Woo Shin, Jin Suk Chung, Seung Hyun Hur, Eui Jung Kim, Quang Trung Tran, Hoang Hung Nguyen, and Paul a. Kohl. Temperature-dependent photoluminescence from chemically and thermally reduced graphene oxide. *Applied Physics Letters*, 99(4):041905, 2011. 72

[108] Dong Su Lee, Christian Riedl, Benjamin Krauss, Klaus von Klitzing, Ulrich Starke, and Jurgen H Smet. Raman spectra of epitaxial graphene on SiC and of epitaxial graphene transferred to SiO2. *Nano letters*, 8(12):4320, December 2008. 75, 106

[109] G. Creeth, A. Strudwick, J. Sadowski, and C. Marrows. Surface morphology and transport studies of epitaxial graphene on SiC(0001[over]). *Physical Review B*, 83(19):195440, May 2011. 75

[110] Harald Jeschke, Martin Garcia, and K. Bennemann. Theory for the Ultrafast Ablation of Graphite Films. *Physical Review Letters*, 87(1):015003, June 2001. 79

[111] M. Lenner, A. Kaplan, Ch. Huchon, and R. Palmer. Ultrafast laser ablation of graphite. *Physical Review B*, 79(18):184105, May 2009.

[112] Guichuan Xing, Hongchen Guo, Xinhai Zhang, Tze Chien Sum, and Cheng Hon Alfred Huan. The Physics of ultrafast saturable absorption in graphene. *Optics Express*, 18(5):4564, February 2010.

[113] Marc Currie, Joshua D. Caldwell, Francisco J. Bezares, Jeremy Robinson, Travis Anderson, Hayden Chun, and Marko Tadjer. Quantifying pulsed laser induced damage to graphene. *Applied Physics Letters*, 99(21):211909, 2011. 79

[114] Adam Roberts, Daniel Cormode, Collin Reynolds, Ty Newhouse-Illige, Brian J. LeRoy, and Arvinder S. Sandhu. Response of graphene to femtosecond high-intensity laser irradiation. *Applied Physics Letters*, 99(5):051912, 2011. 79

[115] A. C. Ferrari. Raman spectroscopy of graphene and graphite: Disorder, electron-phonon coupling, doping and nonadiabatic effects. *Solid State Communications*, 143(1-2):47, 2007. 81, 83

[116] Michele Lazzeri and Francesco Mauri. Nonadiabatic Kohn Anomaly in a Doped Graphene Monolayer. *Physical Review Letters*, 97(26):266407, December 2006. 81

[117] Simone Pisana, Michele Lazzeri, Cinzia Casiraghi, Kostya S Novoselov, a K Geim, Andrea C Ferrari, and Francesco Mauri. Breakdown of the adiabatic Born-Oppenheimer approximation in graphene. *Nature materials*, 6(3):198, March 2007. 81

[118] Jun Yan, Yuanbo Zhang, Philip Kim, and Aron Pinczuk. Electric Field Effect Tuning of Electron-Phonon Coupling in Graphene. *Physical Review Letters*, 98(16):166802, 2007.

[119] A. Das, B. Chakraborty, S. Piscanec, S. Pisana, A. Sood, and A. Ferrari. Phonon renormalization in doped bilayer graphene. *Physical Review B*, 79(15):155417, April 2009. 81

[120] DM Basko, S. Piscanec, and AC Ferrari. Electron-electron interactions and doping dependence of the two-phonon Raman intensity in graphene. *Physical Review B*, 80(16):165413, 2009. 83

[121] C. Stampfer, F. Molitor, D. Graf, K. Ensslin, A. Jungen, C. Hierold, and L. Wirtz. Raman imaging of doping domains in graphene on SiO[sub 2]. *Applied Physics Letters*, 91(24):241907, 2007. 83

[122] T. Mohiuddin, A. Lombardo, R. Nair, A. Bonetti, G. Savini, R. Jalil, N. Bonini, D. Basko, C. Galiotis, N. Marzari, K. Novoselov, A. Geim, and A. Ferrari. Uniaxial strain in graphene by Raman spectroscopy: G peak splitting, Grüneisen parameters, and sample orientation. *Physical Review B*, 79(20):205433, May 2009. 84

[123] H. Choi, F. Borondics, D. A. Siegel, S. Y. Zhou, M. C. Martin, A. Lanzara, and R. A. Kaindl. Broadband electromagnetic response and ultrafast dynamics of few-layer epitaxial graphene. *Applied Physics Letters*, 94(17):172102, 2009. 85, 103

[124] Dong Sun, Zong-Kwei Wu, Charles Divin, Xuebin Li, Claire Berger, Walt A. de Heer, Phillip N. First, and Theodore B. Norris. Ultrafast Relaxation of Excited Dirac Fermions in Epitaxial Graphene Using Optical Differential Transmission Spectroscopy. *Physical Review Letters*, 101(15):157402, 2008.

[125] Dong Sun, Zong-Kwei Wu, Charles Divin, Xuebin Li, Claire Berger, Walt A. De Heer, Phillip N. First, and Theodore B. Norris. Ultrafast dynamics and interlayer thermal coupling of hot carriers in epitaxial graphene. *physica status solidi (c)*, 6(2):470–473, 2009.

[126] Brian Ruzicka, Shuai Wang, Lalani Werake, Ben Weintrub, Kian Loh, and Hui Zhao. Hot carrier diffusion in graphene. *Physical Review B*, 82(19):195414, November 2010.

[127] P. Plochocka, P. Kossacki, A. Golnik, T. Kazimierczuk, C. Berger, W. A. de Heer, and M. Potemski. Slowing hot carrier relaxation in graphene using a magnetic field. *Physical Review B*, 80:245415, June 2009. 85, 103

[128] Ryan W. Newson, Jesse Dean, Ben Schmidt, and Henry M. van Driel. Ultrafast carrier kinetics in exfoliated graphene and thin graphite films. *Optics Express*, 17(4):2326, February 2009. 85, 98, 103

[129] Brian A Ruzicka, Nardeep Kumar, Shuai Wang, Kian Ping Loh, and Hui Zhao. Two-probe study of hot carriers in reduced graphene oxide. *Journal of Applied Physics*, 109(8):084322, 2011. 89

[130] Jared Strait, Haining Wang, Shriram Shivaraman, Virgil Shields, Michael Spencer, and Farhan Rana. Very Slow Cooling Dynamics of Photoexcited Carriers in

Graphene Observed by Optical-Pump Terahertz-Probe Spectroscopy. *Nano letters*, 11(11):4902, October 2011.

[131] J Lee, K M Dani, A Mohite, R Sharma, A J Taylor, and R P Prasankumar. Probing Intraband Conductivity Dynamics in Graphene. In *International Conference on Ultrafast Phenomena*, volume 2, 2010. 89, 92

[132] Chun Hung Lui, Kin Fai Mak, Jie Shan, and Tony F Heinz. Ultrafast Photoluminescence from Graphene. *Physical review letters*, 105(12):13, June 2010. 90

[133] L a Falkovsky. Optical properties of graphene. *Journal of Physics: Conference Series*, 129:012004, October 2008. 90

[134] Leandro M Malard, Kin Fai Mak, A H Castro Neto, N M R Peres, and Tony F Heinz. Observation of Intra- and Inter-band Transitions in the Optical Response of Graphene. *arXiv*, April 2011. 92

[135] Nicola Bonini, Michele Lazzeri, Nicola Marzari, and Francesco Mauri. Phonon Anharmonicities in Graphite and Graphene. *Physical Review Letters*, 99(17):176802, October 2007. 95

[136] Hugen Yan, Daohua Song, Kin Fai Mak, Ioannis Chatzakis, Janina Maultzsch, and Tony F. Heinz. Time-resolved Raman spectroscopy of optical phonons in graphite: Phonon anharmonic coupling and anomalous stiffening. *Physical Review B*, 80(12):121403, September 2009. 95

[137] Kwangu Kang, Daner Abdula, David G. Cahill, and Moonsub Shim. Lifetimes of optical phonons in graphene and graphite by time-resolved incoherent anti-Stokes Raman scattering. *Physical Review B*, 81(16):165405, April 2010. 95

[138] S. Piscanec, M. Lazzeri, Francesco Mauri, A. Ferrari, and J. Robertson. Kohn Anomalies and Electron-Phonon Interactions in Graphite. *Physical Review Letters*, 93(18):185503, October 2004. 97

[139] Tobias Kampfrath, Luca Perfetti, Florian Schapper, Christian Frischkorn, and Martin Wolf. Strongly Coupled Optical Phonons in the Ultrafast Dynamics of the Electronic Energy and Current Relaxation in Graphite. *Physical Review Letters*, 95(18):187403, October 2005. 97, 103

[140] S. Butscher, F. Milde, M. Hirtschulz, E. Malić, and A. Knorr. Hot electron relaxation and phonon dynamics in graphene. *Applied Physics Letters*, 91:203103, 2007. 97

[141] Chun Hung Lui, Li Liu, Kin Fai Mak, George W Flynn, and Tony F Heinz. Ultraflat graphene. *Nature*, 462(7271):339, November 2009. 98

[142] J. Hass, F. Varchon, J. Millán-Otoya, M. Sprinkle, N. Sharma, W. de Heer, C. Berger, P. First, L. Magaud, and E. Conrad. Why Multilayer Graphene on 4H-SiC(0001) Behaves Like a Single Sheet of Graphene. *Physical Review Letters*, 100(12):125504, March 2008. 106

[143] Jamie H Warner, Mark H Rümmeli, Thomas Gemming, Bernd Büchner, and G Andrew D Briggs. Direct imaging of rotational stacking faults in few layer graphene. *Nano letters*, 9(1):102, January 2009. 106

[144] I Forbeaux. Solid-state graphitization mechanisms of silicon carbide 6HSiC polar faces. *Applied Surface Science*, 162-163(1-4):406, August 2000. 106